Magnetic Susceptibility of Alzheimer's Disease Brain Altered by Neurodegeneration

Maruf Ahmed

Magnetic Susceptibility of Alzheimer's Disease Brain Altered by Neurodegeneration

by

Maruf Ahmed

A dissertation submitted in partial satisfaction of the

requirements for the degree of

Doctor of Philosophy

in

Engineering - Electrical Engineering and Computer Sciences

in the

Graduate Division

of the

University of California, Berkeley

Committee in charge:

Professor Chunlei Liu, Chair
Professor Michael Lustig
Professor William Jagust
Assistant Professor Samuel Pimentel

Summer 2023

Magnetic Susceptibility of Alzheimer's Disease Brain Altered by Neurodegeneration

Abstract

Magnetic Susceptibility of Alzheimer's Disease Brain Altered by Neurodegeneration

by

Maruf Ahmed

Doctor of Philosophy in Engineering - Electrical Engineering and Computer Sciences

University of California, Berkeley

Professor Chunlei Liu, Chair

A sensitive and accurate imaging technique capable of tracking the disease progression of Alzheimer's Disease (AD) driven amnestic dementia would be beneficial. A currently available method for pathology detection in AD with high accuracy is Positron Emission Tomography (PET) imaging, despite certain limitations such as low spatial resolution, off-target error, and radiation exposure. Non-invasive Magnetic Resonance Imaging (MRI) scanning with quantitative magnetic susceptibility measurements can be used as a complementary tool. The human brain can be magnetized by the strong magnetic field of an MRI scanner. The corresponding magnetic susceptibility can be computed from MRI signals and is found to be in the order of 10^{-8}. In AD, the accumulation of amyloid plaques, tau neurofibrillary tangles, and iron are crucial signatures of the underlying neurodegenerative process. Amyloid and tau proteins are diamagnetic while biological iron is paramagnetic. The opposing magnetic susceptibility of these sources complicates the quantification of susceptibility changes in the brain. To date, quantitative susceptibility mapping (QSM) has widely been used in tracking deep gray matter iron accumulation in AD. The present work proposes that by compartmentalizing quantitative susceptibility into paramagnetic and diamagnetic components, more holistic information about AD pathogenesis can be acquired. Computational susceptibility-source separation techniques such as DECOMPOSE-QSM can be used to compartmentalize paramagnetic and diamagnetic susceptibilities on a voxel level. In this work, we demonstrated significant voxel-wise differences between AD patients and healthy controls using paramagnetic and diamagnetic susceptibility derived from DECOMPOSE-QSM. Particularly, diamagnetic component susceptibility (DCS) have shown promise in tracking protein accumulation in the grey matter (GM), demyelination in the white matter (WM), and relevant changes in the cerebrospinal fluid (CSF). Through regions of interest (ROI) based analysis, we observed meaningful associations between pathological measures vs paramagnetic and diamagnetic susceptibility in several GM regions typically affected by tau deposition in AD. Finally, we explored the relationship of susceptibility distribution parameters with clinical, pathological, and genetic markers of AD. It has been found that the

separated paramagnetic and diamagnetic susceptibility can be used to track pathological neurodegeneration in different tissue types and regions of the brain. With the initial evidence, we believe the usage of compartmentalized susceptibility demonstrates substantive potential as an MRI-based technique for tracking AD-driven neurodegeneration.

To Sifat-E-Tanzim Chowdhury

My loving wife

Contents

List of Figures

List of Tables

Acknowledgments

I want to start by thanking the almighty for creating me on this earth and giving me the opportunities to find meaning in my life.

I want to thank my advisor for guiding me the way he did. I observed what a personable mentoring skill he demonstrated while advising students from differing backgrounds, knowledge, and experience. He not only created an environment for knowledge sharing but also fostered care for the humane aspects of our lives. Whenever I was stuck in a research problem, he gave me useful advice and suggestions. But beyond that, he understood the kind of stressful experience I went through, not unlike my fellow graduate students, and made accommodations for that. He would also arrange events and trips for encouraging and celebrating our success which acted as positive reinforcement for our research. He is not only a great advisor but also a kind human being.

I also want to thank my thesis committee members professor William Jagust, professor Miki Lustig, and assistant professor Samuel Pimentel. Their advice and suggestion helped me define my research problem in a more concrete manner easing the path of my Ph.D. progress.

I want to thank my colleague and friend Jingjia Chen for helping me get acquainted with the tools and techniques of my research. Without her support, I would never be able to pick up the necessary skills needed to complete my Ph.D. I also appreciated her encouraging words whenever I was struggling with my research. I also acknowledge the support of my other group members for their suggestions in improving my research and dissertation. I want to thank my colleague from the previous research group, Mahsa Sadeghi for guiding me through the research I was doing in that lab. I also want to acknowledge Anju Toor who helped me write my first manuscript, even though unpublished, it helped me improve my writing skills. I want to acknowledge Igal Deckman who introduced me to the pieces of lab equipment and lab culture in my previous lab. I also acknowledge all the members of my previous research group for their support in my journey. I am also grateful to my graduate school friends and colleagues Jake Sporrer, Urmita Sikder, Dwipayan Patnaik, and many more, who inspired me with their kind words in difficult times. I also give thanks to my first Ph.D. advisor Sayeef Salahuddin for playing his role in admitting me to UC Berkeley.

I am grateful to the EECS graduate division staff, in particular, Shirley Salanio for her support and help throughout my graduate career. Her advice and suggestions in academic, funding-related, and even personal matters were amazing. Her presence made my graduate experience tractable.

I also acknowledge the mental health resources in Berkeley which helped me through difficult times and guided me to find myself anew. My experience with therapists made me more resilient and equipped me to maintain sanity during failures.

I acknowledge all the researchers, technician, and staff at Mayo Clinic Alzheimer's Disease Research Center (MCADRC) for graciously providing me with the data used in my research. The data contained in this analysis were obtained under one of the following research grants from the National Institutes of Health to the Mayo Clinic Study of Aging (U01 AG06786,

Chapter 1

Introduction

Researchers have been trying to understand Alzheimer's disease-driven neurodegenerative pathology for a long time. Neurodegenerative diseases affect a big portion of the elderly population in the world. The following table presents the number of people affected by neurodegenerative pathologies each year. It is important to note AD is one of the most impactful neurodegenerative diseases.

Disease	Global population (in millions)
Alzheimer's disease (AD) and other dementia	55
Parkinson's disease (PD)	10
Multiple sclerosis (MS)	2.8
Amyotrophic lateral sclerosis (ALS)	0.45

Table 1.1: Global population affected by neurodegenerative diseases

Over the years, people have used different techniques to diagnose and detect the progression of neurodegenerative diseases. Clinical markers have been predominantly used to detect disease and remain the primary mode of diagnosis. However, it has been suggested that a combination of different markers can be of best use when tracking a neurodegenerative disease is concerned. These markers may be clinical, biochemical, genetic, and imaging [1].

After clinical biomarkers, CSF biochemical markers are the most discriminative for AD diagnosis [2]. Decreased CSF β-amyloid-42/β-amyloid-40 ratio has been reported to identify AD patients distinctively [3] and the increase of CSF phosphorylated-τ/β-amyloid-42 ratio is shown to be an accurate biomarker for detecting AD dementia [4]. As a genetic marker, ApoE4 has been associated with progressing from MCI to AD [5]. Among the imaging markers, positron emission tomography (PET) has been used to confirm the presence of AD. Increased amyloid and tau PET signals in the brain and reduced FDG PET in different regions are typical of AD patients [6]. Additionally, structural MRI can detect atrophy at the late stages of AD [7].

Clinical markers are more useful at the late stages of the disease. Biochemical markers, particularly CSF markers are invasive. PET comes with radiation exposure and smaller resolution. Nonetheless, all of these markers are quite important in terms of understanding the disease. However, multimodal investigation and fruition of less or non-invasive markers are essential for the early detection and study of gradual pathology progression in AD.

Non-invasive techniques like magnetic resonance imaging (MRI) can be very useful in terms of overcoming the limitation of the current gold standard of PET imaging. Together with PET imaging MRI modalities can come in handy in reducing the number of scans or even reducing radiation dose [8]. Among the candidates of MRI in this regard, diffusion tensor imaging (DTI), magnetization transfer imaging (MTI), and quantitative susceptibility mapping (QSM) are worth mentioning. For a while now, diffusion metrics like fractional anisotropy (FA) and mean diffusivity (MD) have been used for tracking WM, myelin in particular, in health and disease. However, recently Neurite Orientation Dispersion and Density Imaging (NODDI), a successor of DTI has shown promise in tracking WM [9] alteration which can theoretically be extended to GM. However, QSM is more specific in studying myelin concentration compared to diffusion imaging [10] and diffusion MRI is more time-consuming resulting in potential discomfort for patients. Macromolecular Proton Fraction (MPF) measured using MTI is also useful in studying WM myelination but it suffers from SAR limitation [11]. Neither NODDI nor MPF can track changes related to Fe accumulation in GM. Quantitative Susceptibility Mapping (QSM) can make up for a few of these limitations like reduced scan time, safe SAR limit, and tracking both Fe, myelin, and other potential changes.

In AD neurodegeneration amyloid plaque and tau tangles may accumulate in the cortical gray matter (GM). Age-related Fe accumulation is also a well-known phenomenon in the human brain. QSM is a well-established technique to assess iron accumulation in the brain caused by aging or AD. On top of that plaques and tangles may have their diamagnetic susceptibility. Brain white matter contains myelin demonstrating diamagnetic susceptibility too. So, in healthy and AD brain iron and other para- and dia-magnetic species have been and can be tracked using QSM. In particular, substantia nigra is very distinctive in terms of iron accumulation in PD and the iron concentration is a discriminatory factor between healthy and PD brain [12]. Using QSM MS lesions has also been made visible and different kind of lesions have been identified [13].

So, far, however, QSM has been used in a limited capacity to mostly track iron-related neurodegeneration in AD. In a voxel, different sources of susceptibility can be present. QSM is an estimate of the overall average susceptibility of a voxel, hence, lacks the information about composition of the sub-voxel level susceptibility. As a result, at a voxel level, the susceptibility estimation lacks accuracy. On top of that if any kind of image registration or warping technique is used or region of interest (ROI) analysis is performed nearby voxels intermix with each other causing further loss of information. Additionally, at an ROI level, the distribution of susceptibility sources is as much important as the magnitude of the sources. Hence, the spread of susceptibility distribution, and other properties can be very useful in tracking susceptibility signature of neurodegeneration.

Recently many techniques have been proposed to separate susceptibility sources on a sub-voxel level [14, 15, 16]. In particular, DECOMPOSE-QSM [14] has been proposed which only uses MEGRE data and no additional scan to compartmentalize susceptibility sources. In the current work, we used this susceptibility separation technique to better understand the relationship between AD pathology and susceptibility.

In Chapter 2 the fundamental concepts related to QSM and DECOPMOSE-QSM are discussed. The data analysis approach and data details are also presented.

In Chapter 3 paramagnetic compartment susceptibility (PCS) I used to understand iron-related degeneration in cortical and sub-cortical GM. AD patients were compared with healthy controls to find areas of differences caused by iron accumulation. Amyloid and tau PET were also correlated with PCS to assess how much iron-related information is shared between these different modalities on an ROI level. A similar analysis with a different cohort is repeated to assess the reproducibility of our results.

In Chapter 4 diamagnetic component susceptibility (DCS) is used to find areas of differences between healthy controls and AD patients. Areas in GM are observed to see if to assess protein accumulation. Areas of differences in WM are analyzed to observe myelin degeneration. Even in CSF differences may exist between AD patients and controls because of structural or compositional differences.

In Chapter 5 the effect of susceptibility distribution parameters is analyzed to explain the difference between patients and controls as well as pathology progression. Susceptibility metrics combined with genetic information and other biomarkers may pave the way to understanding AD pathogenesis better.

In Chapter 6 the overall conclusion of current work and future directions to be explored is introduced.

Chapter 2

Background and Methodology

In this chapter, the tools and techniques employed in current research will be introduced. Quantitative susceptibility mapping (QSM) is a tool to recover information from MRI phase images. Previously only magnitude images were used for imaging the brain and other organs in health and disease and the phase images were discarded. Also, susceptibility variation was interpreted as an artifact rather than actual information [17]. However, over the last few decades phase images are being investigated to retrieve further information and QSM is one of those approaches. 100s of algorithms have been proposed and are being proposed for QSM reconstruction. In current work, STAR-QSM [18] has been employed to study tissue susceptibility maps.

QSM is the basic way of tracking susceptibility variation in bio-tissue. However, it is limited in terms of separating effects from different polarities of susceptibility. Recently several approaches have been used to extract further information from QSM. One of the ways is to retrieve multi-frequency compartments [19, 20] from localized signals. Another approach is to compartmentalize susceptibility [14, 16]. In the current work, a susceptibility separation technique has been chosen for further investigation of its performance to study disease pathology progression. The approach selected here is DECOMPOSE-QSM. In this chapter, DECOMPOSE-QSM [14] and relevant processing steps will be introduced as a starting point for the discussions and analyses to follow in the next chapters.

Voxel-wise and ROI analysis have been used to study the difference between healthy control (HC) participants and patients. As will be discussed in later chapters Alzheimer's disease (AD) has been chosen as the disease of study for the current work. Differences in QSM between AD patients and HC participants will be introduced in terms of voxel-wise and ROI analysis.

2.1 STAR-QSM

The basic principle behind QSM is the relationship between phase signal, ϕ and magnetic field intensity variation, ΔB_z as shown in Eqn. 2.1 [21] and Eqn. 2.2 [22]. Here, $\phi(\vec{r}, \text{TE})$ is

the phase of the signal at any point $\vec{r}$ at echo time TE, $\phi_0(\vec{r}, \text{TE})$ is a coil sensitivity dependent phase offset, γ is the gyromagnetic ratio, k is the k-space vector and k_z its z-component, B_0 is the applied magnetic field, taken to be in the z-direction, and $\chi(k)$ is the Fourier transform of the magnetic susceptibility distribution. QSM computation is performed by inverting Eqn. 2.2.

$$\phi(\vec{r}, \text{TE}) = \phi_0(\vec{r}, \text{TE}) + \gamma \cdot \Delta B_z(\vec{r}) \cdot \text{TE}, \tag{2.1}$$

$$\Delta B_z(k) = B_0(1/3 - k_z^2/|k|^2)\chi(k). \tag{2.2}$$

For the acquisition of QSM, the phase of the signal has to relate to the local magnetic field. In gradient-echo-based echo-planar imaging or gradient recalled echo (GRE) sequence the phase is a function of the local magnetic field making these good candidates for QSM reconstruction [21, 23]. The sequence used in the current study is multi-echo gradient recalled echo (MEGRE) where the phase information at multiple TE is available. The raw magnitude and phase images of a particular slice for a subject in the current study are presented in Fig. 2.1(A) and Fig. 2.1(B) containing images of all collected TE.

In Fig. 2.1(B) the discontinuity in the phase image occurs from phase wrapping happening during acquisition. Laplacian phase unwrapping is used which is fast and robust because of taking advantage of fast Fourier transform (FFT) [24]. In Fig. 2.1(C) Laplacian phase unwrapped images at all TE are presented. Using the Spherical Mean Value (SMV) property of harmonic functions a Variable-kernel Sophisticated Harmonic Artifact Reduction of the Phase data (VSHARP) [25, 26] method has been used to remove the background field using SMV size of 12 pixels. Images after VSHARP processing is presented in Fig. 2.1(D).

After VSHARP as shown in Fig. 2.1(D), the local tissue phase is obtained. Using Eqn. 2.1 and 2.2 now susceptibility could be reconstructed. However, Eqn. 2.2 is ill-posed on a conical surface in k-space ($k^2 - 3k_z^2 = 0$) resulting in streaking artifacts in the computed QSM [18]. One solution would be to sample k-space in multiple orientations with a technique named COSMOS [27], but that is too time-consuming and hence, inapplicable for clinical setup. Therefore, we resort to Streaking artifact reduction for quantitative susceptibility mapping (STAR-QSM) [18] approach which showed improved accuracy in reconstruction for sources with large dynamic range. The images after reconstruction using STI Suite [28] for all the echoes are presented in Fig. 2.1(E). Averaging multiple TE images a mean QSM image can also be generated as shown in Fig. 2.2.
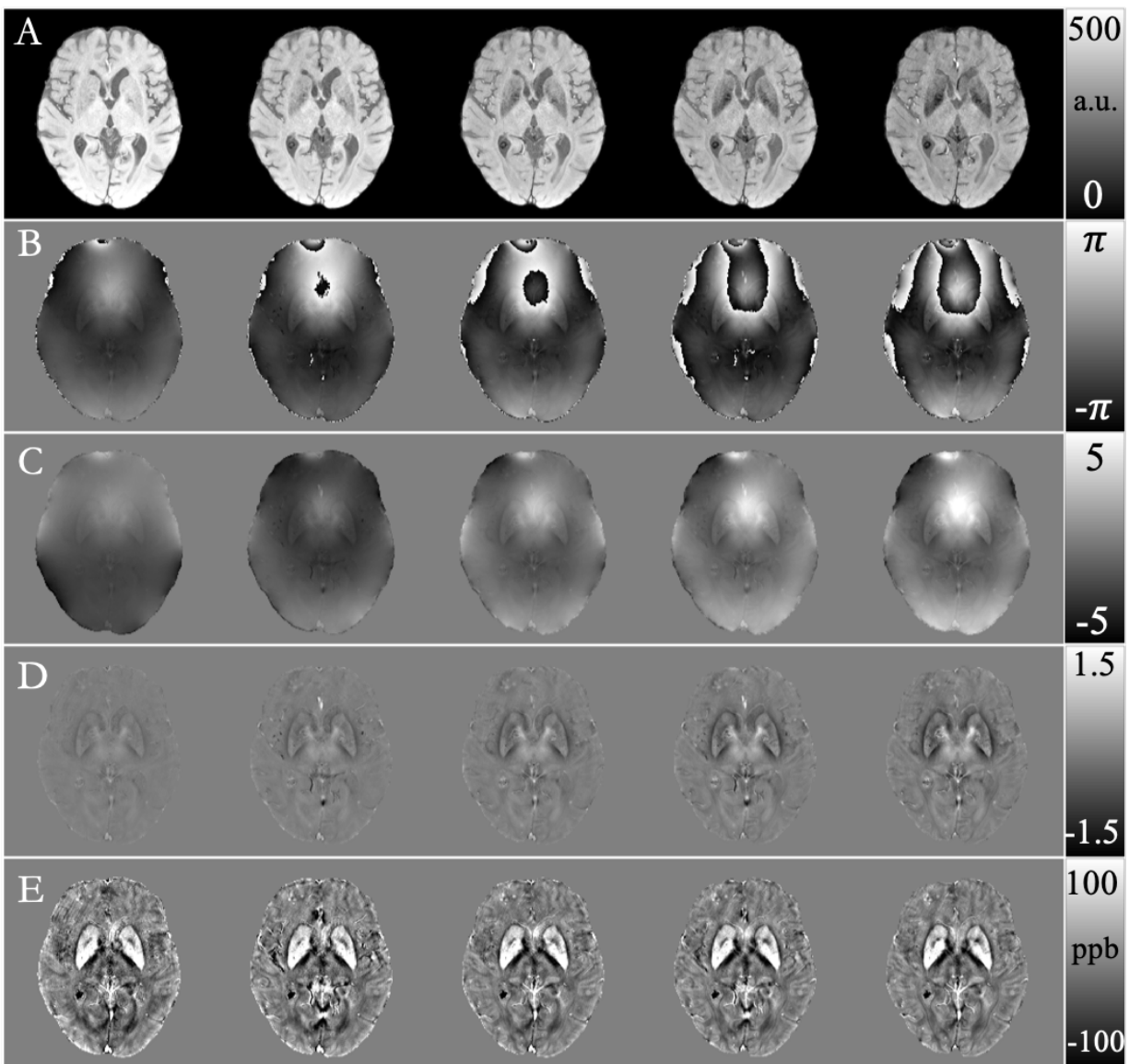
Figure 2.1: Sample images at different steps of QSM processing from an 89-year-old subject. (A) Raw magnitude images, (B) raw phase images, (C) unwrapped phase images using laplacian phase unwrapping, (D) background field removed images using VSHARP, and (E) final QSM images for all 5 echoes in the acquired data.

2.2   DECOMPOSE-QSM

First introduced by Chen et al [14] DiamagnEtic COMponent and Paramagnetic cOmponent SEparation or DECOMPOSE-QSM has been shown to separate paramagnetic compo-

nent susceptibility (PCS) and diamagnetic component susceptibility (DCS) using the same MEGRE data used in QSM reconstruction without the need of any additional scan. The principle is based on Eqn. 2.3.

$$S(t; C_p, C_n, \chi_p, \chi_n, R^*_{2,0}) = C_p e^{-(a\chi_p + R^*_{2,0} + i2/3\chi_p \gamma B_0)t} + C_n e^{-(-a\chi_n + R^*_{2,0} + i2/3\chi_n \gamma B_0)t} + C_0 e^{-R^*_{2,0}t},$$
(2.3)

where, S is the localized signal generated from each voxel, $\chi(p)$ represents the volume susceptibility of the paramagnetic compartment, $\chi(n)$ represents the volume susceptibility of the diamagnetic compartment, $R^*_{2,0}$ is the transverse relaxation rate of the reference susceptibility medium, $a = 323.5$ Hz/ppm at 3T, C_p, C_n, C_0 indicate the concentrations of the corresponding components.
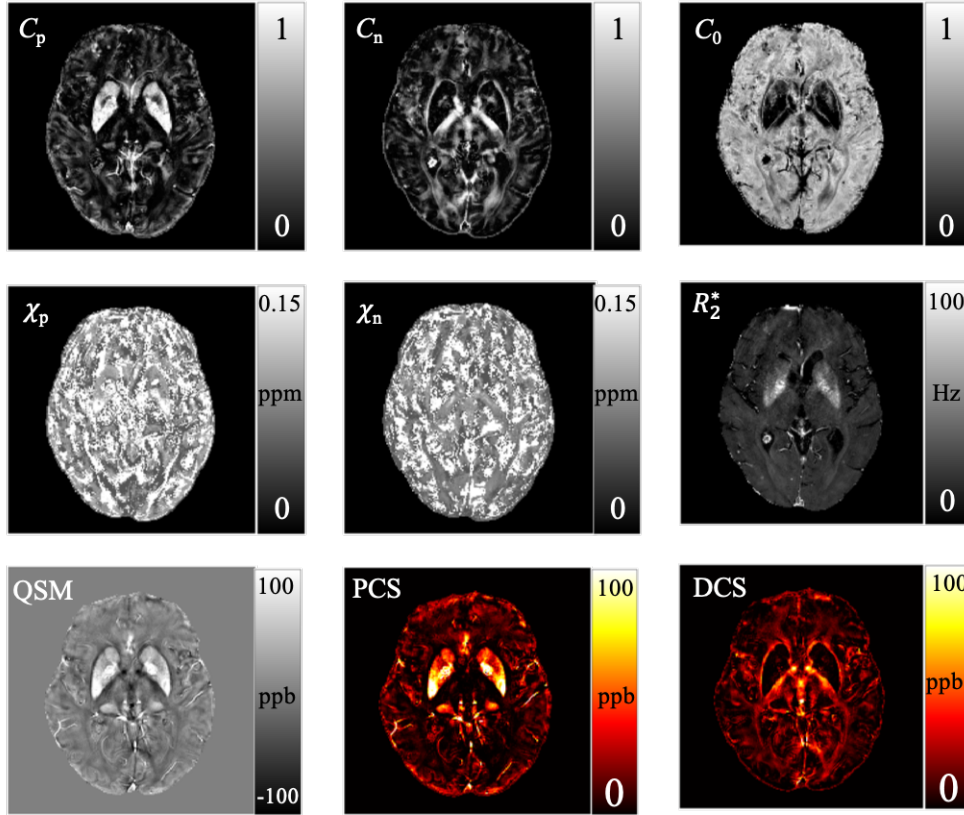
Figure 2.2: Different outputs from DECOMPOSE-QSM model from an 89-year-old subject.

First QSM is computed and signal S is generated using localized QSM value at each voxel, a signal model is initialized, and different parameters are solved using a non-linear solver. Later PCS and DCS are defined accounting for complex tissue environment as if

either only paramagnetic or diamagnetic species is present in the voxel along with neutral component as discussed in [14]. Different outputs of the DECOMPOSE-QSM algorithm for a chosen subject are plotted in Fig. 2.2.

In Fig. 2.2 C_p and PCS delineated the presence of paramagnetic species primarily iron in cortical and subcortical areas. C_n and DCS demonstrated brightened signals in myelinated white matter (WM) regions. Representing the reference susceptibility C_0 shows a uniform pattern everywhere except deep gray matter (GM). QSM in this figure is computed by taking the temporal average of all the TE-dependent QSM in Fig. 2.2 χ_p and χ_n did not show too much structural delineation because they represent only the volume susceptibility of each species in each voxel. Here, R_2^* is an intermediate parameter depicting the transverse relaxation time of the reference tissue.

2.3 Data details and method

2.3.1 Data information

Demographic details of the data used in the analysis is presented in Table 2.1. MRI, PET, imaging data, and demographic data were collected at the Mayo Clinic Alzheimer's Disease Research Center (MCADRC). Data from 71 β-amyloid and tau negative cognitively unimpaired (CU) Healthy control (HC) participants and 49 β-amyloid and tau positive [29] AD patients were used in the current analysis. HC and AD groups were compared using the χ^2 test for sex. No significant difference was found between the AD and the HC group ($\chi^2 = 0.64$, p > 0.4). Hence, sex was not considered a confounding variable for any of the analyses performed in this article. The study was approved by the Mayo Clinic institutional review board. All participants provided informed written consent; a legally authorized representative provided consent for cognitively impaired participants, as necessary. MRI, PET, and other data from the MCADRC are available to qualified academic and industry researchers by request to the MCADRC Executive Committee (https://www.mayo.edu/research/centers-programs/alzheimers-disease-research-center/research-activities/mayo-clinic-study-aging/for-researchers/data-sharing-resources).

Variable	AD patients (n=49)	CU HC participants (n=71)
Male/female	24/24 (50%/50%)	42/29 (59%/41%)
Age	67 (60, 76)	65 (52, 71)
STMS	22 (18, 28)	37 (36, 38)
Education	16 (13.75, 16)	16 (14, 16.5)

Table 2.1: Demographic details of selected participant data. Values are displayed as median (1st quartile, 3rd quartile). STMS: Short Test of Mental State

2.3.2   MRI scan

T_1-weighted structural scans were performed on a 3T MRI scanner (Siemens MAGNETOM Prisma, software version: VE11C) using a 3D Magnetization Prepared Rapid Acquisition Gradient Recalled Echo (MPRAGE [30]) pulse sequence. The scan parameters were; TE/TR of 3/2300 ms, TI of 900 ms, and $0.8 \times 0.8 \times 0.8$ mm^3 imaging resolution. The MPRAGE image for each participant was segmented using FreeSurfer 5.3 (https://surfer.nmr.mgh.harvard.edu/) [31, 32] for defining GM ROIs to be used later for correlation analysis.

3D Multi-echo GRE data (MEGRE) with 5 echoes were collected in the same exam with the following acquisition parameters: $TE_1/\Delta TE/TE_5 = 6.71/3.91/22.35$ ms, matrix size = $384 \times 269 \times 88$, spatial resolution = $0.52 \times 0.52 \times 1.8$ mm^3, with GRAPPA 2x acceleration; the total acquisition time per participant was 6 min 37 sec. More details on the acquisition can be found in Cogswell et al [33]. The MEGRE complex images were down sampled in-plane by a factor of two to reduce anisotropy of the spatial resolution, hence, improving the accuracy of the dipole kernel inversion for QSM and reducing computation time during the processing of DECOMPOSE-QSM.

2.3.3   PET scan

Late uptake PiB PET images for detecting β-amyloid plaques were acquired on PET-CT scanners for 40–60 minutes and Flortaucipir (FTP or tau) for 80-100 minutes after injection. Each had four, five-minute frames. Low-dose CT scanning was performed for attenuation correction. Reconstructions were performed on-scanner with iterative ordered subset expectation maximization (OSEM) algorithms. A 5 mm Gaussian post-reconstruction filter was applied, along with standard corrections for attenuation, scatter, random coincidences, and decay. Four-frame dynamic PET images were co-registered with a group-wise rigid registration to correct for cross-frame motion and averaged to produce a single static (summed) PET image. These images were co-registered with T_1-weighted structural images using SPM12 [34]. Voxel-wise PET SUVr values were computed by normalizing with cerebellar crus GM [35]. More details on PET imaging can be found in [33].

2.3.4   Image registration and other tools

Structural images were warped to standard (Montreal Neurological Institute) MNI [36] space using (ANTs) [37]. First, brain masks from the MPRAGE images were extracted using FSL [38] Brain Extraction Tool (BET). Then the first echo of the MEGRE magnitude images was co-registered to BET extracted MPRAGE image using rigid transformation with ANTs. For each participant, a composite transform was generated combining the transforms from QSM to MPRAGE T_1 structural space and the one from native T_1 structural space to MNI T_1 space. This composite transform was used to warp an individual's QSM map to MNI space, and this process was repeated for all participants. All QSM maps warped to MNI space were concatenated and sent as input to the FSL tool named randomise [39] for group comparison.

The disease status and age of the patients were used to generate the design matrix. Then FSL randomise was used for group comparison using the default 5000 permutations [40, 41]. The Threshold-Free Cluster Enhancement (TFCE) [42] statistics with family-wise error (FWER) correction were reported. The randomise analysis was performed for the full brain tissue volume without spatial smoothing. MNI space was segmented using FSL FMRIB's Automated Segmentation Tool (FAST) [43]. Region-specific results were drawn by applying tissue segmentation masks to the randomise outputs. For voxel-wise analysis, corrected $p < 0.05$ was considered. BrainSlicer [44] was used to plot brain images.

2.4 Sample QSM voxel-wise analysis

A sample voxel-wise group difference between AD patients and HC participants will be presented here. Fig. 2.3 presents different steps involved and important image registration and warping examples.

Fig. 2.4 presents voxel-wise group differences between AD patients and HC participants. Increased QSM is observed in cortical and subcortical GM areas in AD patients. The comparison in WM is a little complicated because of negative values of susceptibility. The areas with larger QSM will be regions with decreased susceptibility because decreased magnitude represents increased negative value. This problem is avoided if negative and positive QSM are analyzed separately. In our analysis of Chapter 4 |DCS| is already separated from its positive counterpart so in that case lower |DCS| will represent areas of lower diamagnetic susceptibility.

Finally, Fig. 2.5 depicts a representative axial slice of different imaging contrasts of the averaged images across subjects in the MNI space utilized in the current work. Structural MPRAGE images were used for segmentation and normalization. The averaged structural image in the AD group shows more ventricular space compared to HC participants in the chosen slice. PiB and FTP PET were used as pathological markers of dementia. The averaged PiB image of AD patients showed widespread elevated SUVr in cortical GM compared to HC participants. The average FTP SUVR in AD group was higher in temporal cortex compared to HC participants. QSM values show the bulk magnetic susceptibility relative to the reference (the mean susceptibility of the whole brain volume). A positive value (bright) means paramagnetic susceptibility and a negative value (dark) means diamagnetic susceptibility. QSM and MEGRE magnitude images were used as inputs to the DECOMPOSE-QSM algorithm. Average QSM and PCS images showed a stronger signal in basal ganglia in the AD group compared to HC participants in the slice shown. The average |DCS| value was weaker in the AD group compared to HC participants in the internal capsule region. Also, the brighter |DCS| regions had more well-defined and sharper boundaries in HC participants compared to AD patients.
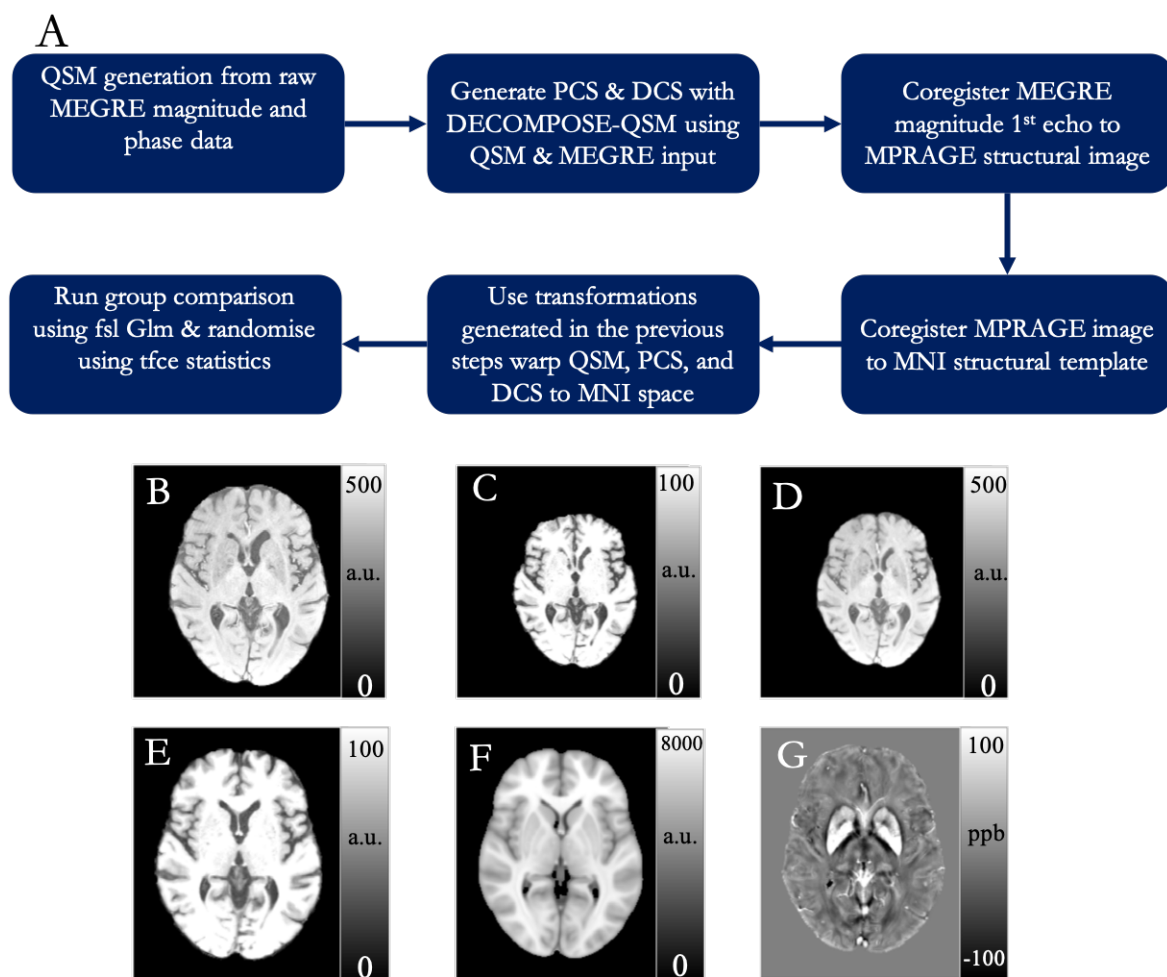
Figure 2.3: (A) Pipeline, (B) first echo MEGRE skull stripped (using fsl bet) magnitude, (C) skull-stripped MPRAGE, (D) MEGRE first echo magnitude warped to MPRAGE, (E) MPRAGE warped to MNI space, (F) MNI template, and (G) QSM warped to MNI template from the same subject presented in Fig. 2.1.

2.5   Conclusion

Susceptibility measurements in terms of QSM and DECOMPOSE-QSM have been reviewed in this chapter. In later chapters, these susceptibility metrics will be analyzed thoroughly in studying AD-driven neurodegeneration.
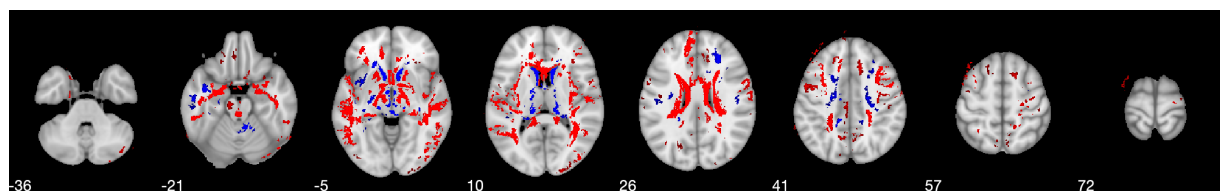
Figure 2.4: QSM voxelwise group difference between AD patients and HC participants. In red clusters $\text{QSM}_{\text{AD}} > \text{QSM}_{\text{HC}}$ and in blue clusters $\text{QSM}_{\text{AD}} < \text{QSM}_{\text{HC}}$.
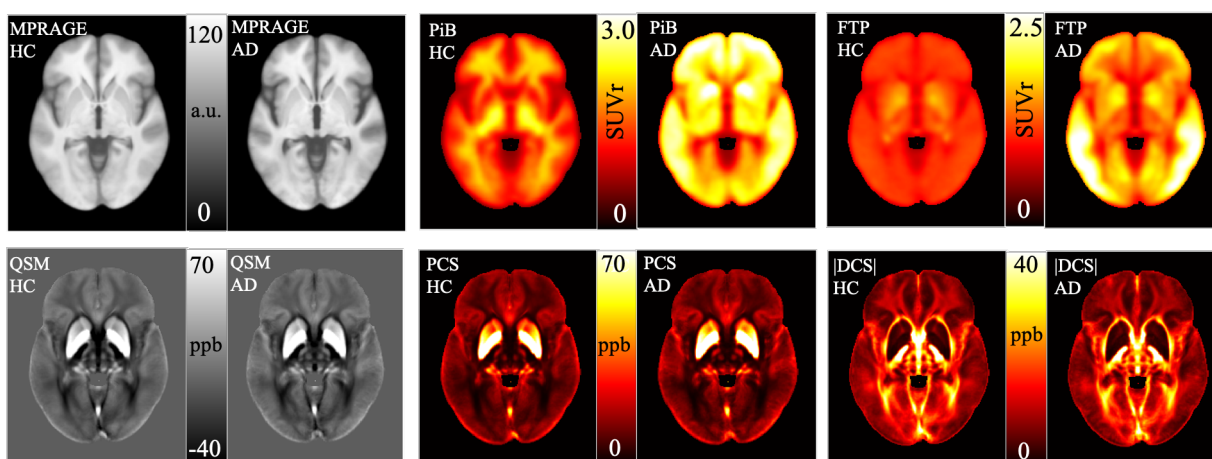
Figure 2.5: Representative slice of average MNI space images of different contrasts for HC and AD group. Ventricles appear bigger in structural images of AD subjects compared to HC participants as seen in the structural MPRAGE (top left) panel. Strong PiB PET (top middle) signal spread over the whole cortical GM was present for the AD patients dissimilar to a healthy brain which was marked by non-specific PET SUVr in the WM. FTP PET SUVr (top right) was high in the temporal cortex, which is typical of an AD patient but absent in HC. QSM (bottom left) showed stronger contrast in the deep GM AD patients compared to HC participants. PCS (bottom middle) demonstrated brighter contrast in deep GM for AD patients compared to HC participants. |DCS| (bottom right) showed an overall brighter contrast in HC participants compared to AD patients. In cortical WM |DCS| map in the AD group showed reduced contrast compared to the HC group. Note that the DCS map is shown in absolute value for simplicity. The higher the |DCS| value the more diamagnetic content is. a.u.: arbitrary unit. SUVr: standardized uptake value ratio. ppb: parts per billion, 10^{-9}.

Chapter 3

Study of Iron Mediated AD Neurodegeneration Using Paramagnetic Susceptibility in QSM

Iron plays a vital role in brain function, particularly in neurotransmitter metabolism, myelin formation, and mitochondrial function [45]. Although iron is essential for human cognitive behavior the accumulation of excess iron can induce degenerative processes in brain tissue. Several processes have been hypothesized for an increase in brain iron, particularly with aging brain iron accumulation is a very well-known phenomenon [46]. In Alzheimer's disease (AD) iron is hypothesized to accumulate with amyloid plaques [47]and tau tangles [48]. However, whether iron accumulation is only associated with protein accumulation or is responsible for further downstream degeneration yet to be studied. Irrespective of the origin, iron accumulation is known to happen in the brain with AD and other neurodegenerative diseases [49]. Increased iron further affects homeostasis and catalyzes the fenton reaction generating reactive oxygenation species (ROS) and participating in damaging the DNA structure, resulting in lipid peroxidation, affecting mitochondrial function, and ultimately neuronal cell death known as ferroptosis [50].

QSM has been frequently used to track iron accumulation in AD. Acosta-Cabronero et al [51] showed a voxel-wise difference between AD patients and controls attributing the QSM-measured susceptibility difference to iron accumulation with a very small number of subjects (19 in total). Du et al [49] showed a difference between AD patients and control in deep gray matter using QSM. Kim et al also showed a difference between AD and controls in mostly deep gray matter using QSM, number of patients in that study was 57 in total. So far most of the studies conducted used QSM as a measure of iron. If the paramagnetic susceptibility of iron is measured more accurately without the competing effect of diamagnetic susceptibility using source-separation algorithms, it is anticipated to improve the accuracy to track iron-related changes associated with neurodegeneration. In the current work using a relatively larger cohort, 49 AD patients and 71 controls, and using PCS as a measure of paramagnetic susceptibility we obtain voxel-wise group difference between patients and controls. On top

of that, using ROI based correlation of the AD patients, we associate tau PET with PCS as a proxy of iron accumulation in AD neurodegeneration. This kind of study is necessary to assess the usefulness of susceptibility source-separation techniques such as DECOMPOSE-QSM and find new ways of using source-separated susceptibility to probe more detailed information about iron-mediated neurodegeneration in AD.

3.1 Voxel-wise group analysis

A metric defined by the ratio of the number of voxels with a greater PCS in AD patients relative to the HC participants and the number of voxels with a smaller PCS for the same combination was computed. The ratio is denoted by m and subscripted by the corresponding susceptibility metric is as follows:

$$m_{\text{PCS}} = \frac{\text{number of voxels with PCS}_{\text{AD}} > \text{PCS}_{\text{HC}}}{\text{number of voxels with PCS}_{\text{AD}} < \text{PCS}_{\text{HC}}}. \tag{3.1}$$

3.1.1 AD patients differ from healthy controls at GM in voxel-wise analysis of PCS

In Fig. 3.1 regions with increased iron have been shown in red after a voxel-wise group analysis between amyloid and tau-positive healthy controls and amyloid and tau-negative AD patients. The clusters with increased iron predominantly reside in precentral cortex, frontal cortex, temporal cortex, parahippocampal cortex, and subcortical regions such as pallidum and putamen. In frontal cortex and hippocampus iron accumulation was colocalized with amyloid and p-tau (hyperphosphorylated-tau) as reported previously [52]. Elevated iron levels were also seen in Inferior temporal cortex, hippocampus, putamen, and globus pallidus revealed by MRI [52]. An increase of iron in frontal and temporal cortex has been shown to be associated with reduced performance in language tasks [53, 54]. Increased ferritin iron accumulation in hippocampus has been shown to damage its structural integrity [55]. Hippocampal iron increase has been associated with reduced episodic memory [53].

The voxel-wise analysis in the current work not only conforms to the regions of iron accumulation but establishes the viability of PCS as a measure for iron accumulation observation. The pattern emerging from the voxel-wise analysis can be considered for further probing the origin of this iron-related dyshomeostasis in AD [56]. Also, the pattern of iron accumulation seems asymmetric in that iron more prominently accumulates in the left hemisphere. In fact, this left hemispheric asymmetric degeneration faster than its right counterpart has been reported before [57]; in our analysis, we see the confirmation of this occurrence through iron accumulation represented by PCS.

In Fig. 3.1 regions with lower PCS in AD patients compared to HC participants are marked in blue. Clusters are primarily located in a very small portion of the frontal cortex, part of thalamus, and caudate nucleus. While an increase in iron is well-established
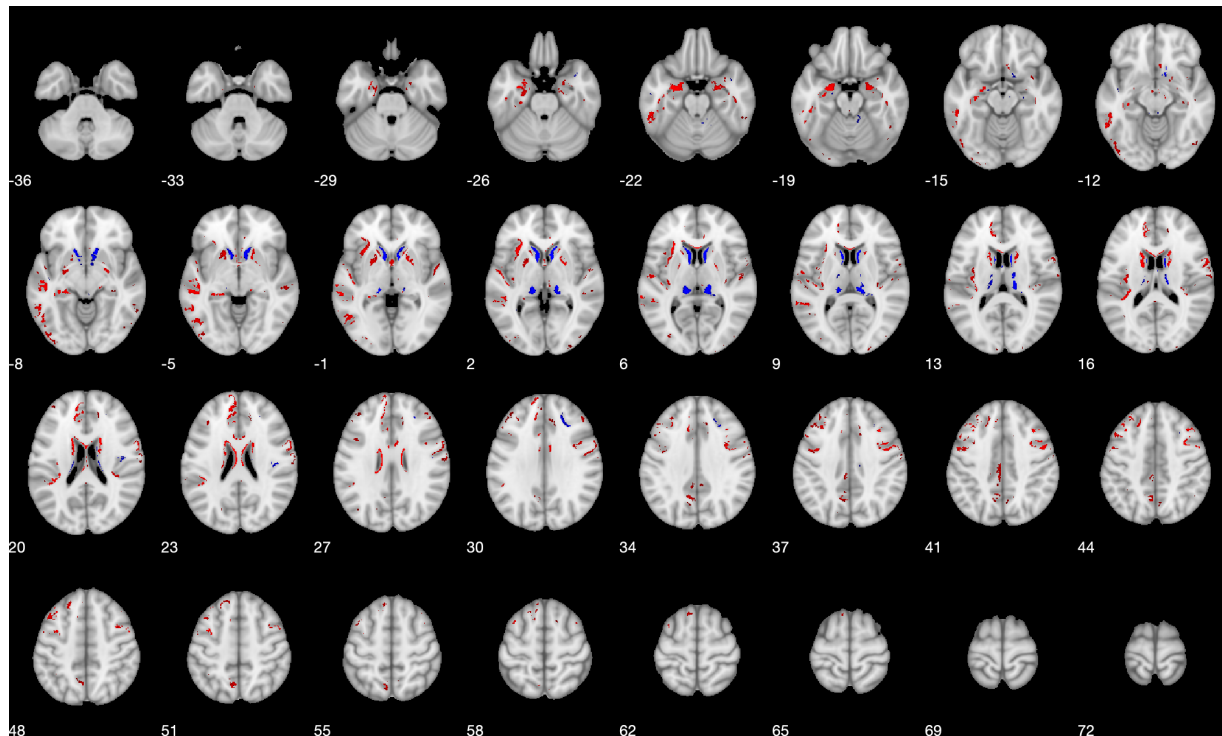
Figure 3.1: Result of voxel-wise group analysis of PCS between patients and controls. Predominant clusters with higher PCS in AD (red) are present in precentral cortex, frontal cortex, temporal cortex, precuneus, parahippocampal cortex, and subcortical deep gray matter (putamen and pallidum). Predominant clusters with lower PCS in AD (blue) are primarily located in the frontal cortex, thalamus, and caudate nucleus.

phenomenon in AD this reduction of iron in AD seems interesting. It is not surprising that some of the clusters will have lower iron in AD patients as iron is dysregulated in the AD brain. Further confirmation is needed through histology that some regions may show a reduction of iron in AD. It should also be stressed the number of voxels with higher PCS in AD patients (compared to HC participants) far outweigh the number of lower PCS; to be precise the metric defined in Eqn. 3.1 m_{PCS} is 4.4 for GM. So, overall a higher iron load is confirmed for AD patients compared to HC participants. The pattern established by PCS is in well-agreement by current literature and yet another way to confirm the presence of iron in potentially a more accurate manner because PCS is not contaminated by diamagnetic sources even at the voxel level.

3.1.2 AD patients differ from healthy controls at WM in voxel-wise analysis of PCS

Oligodendrocytes, microglia, and astrocytes contain much more iron compared to neurons [52]. Hence, the increase of iron in these cells may become visible in iron-related contrasts such as PCS. Previously because susceptibility separation techniques were not being used, QSM in the WM primarily represented myelin. However, with DECOMPOSE-QSM technique PCS in WM has also been assessed.
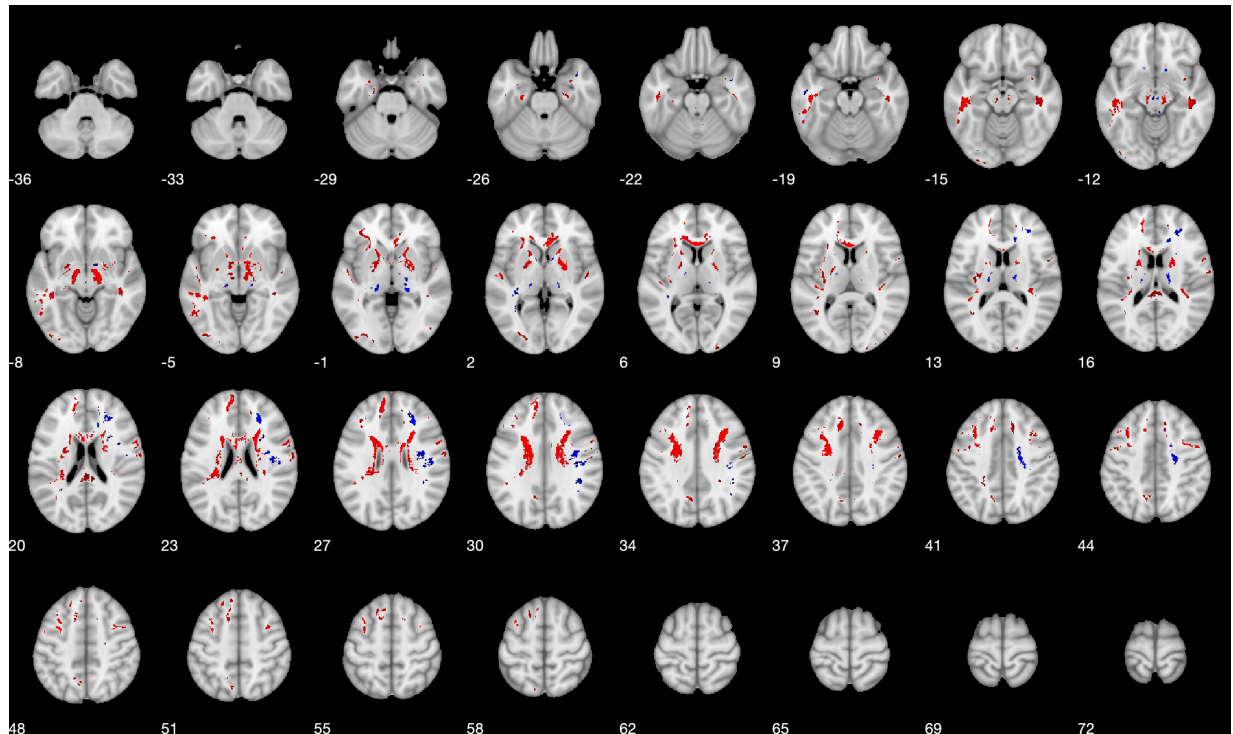
Figure 3.2: Clusters with higher PCS (red) in the WM of AD patients compared to HC participants and lower PCS (blue) in AD patients compared to HC participants. The number of voxels with higher PCS is much larger compared to lower PCS in the AD group. Clusters with higher PCS in AD patients are located in frontal white matter, superior fronto-occipital fasciculus, superior corona radiata, genu, and splenium of corpus callosum, and cerebral peduncle to name a few with a very widespread pattern. On the other hand, lower PCS is found only in a few clusters located in the cingulum bundle, and some part of the thalamic white matter.

In WM regions with higher PCS in AD are prominently located in frontal white matter, superior fronto-occipital fasciculus, superior corona radiata, genu, and splenium of corpus callosum, cerebral peduncle whereas regions with lower PCS in AD are much less prevalent

in the WM. As we already know iron homeostasis is negatively affected in AD pathology it is not unexpected that even in WM regions the concentration of iron would be high compared to HC participants. Increased iron in hippocampal microglia, middle temporal gyrus adjacent WM, and along myelinated fibers have been reported previously [52, 58, 59, 60, 61]. The increase of iron in cortical III-V layers and microglia is hypothesized to provide high iron concentration for myelinization and oligodendrocyte differentiation [62]. Hippocampal fimbria has been shown to have higher iron levels (measured via QSM) in AD patients [63]. The ratio of voxels with higher PCS in AD patients (compared to HC participants) to that of voxels with lower PCS in AD patients, m_{PCS} in WM was computed as 6.5; i.e. majority of the voxels in AD patients showed higher PCS indicating an increase of iron in WM. So, in AD throughout the whole brain, the overall iron load is increased not just in the cortex or gray matter.

3.1.3 AD patients differ from healthy controls at CSF in voxel-wise analysis of PCS

As shown in Fig. 3.3 in CSF too, the number of voxels with higher PCS in AD patients is much larger compared to that of HC participants. The m_{PCS} value for CSF was 4.78. An increase in ferritin, an iron storage protein, has been reported in AD [54]. CSF ferritin level has been shown to be associated with cognitive decline [53]. The concentration of other proteins such as melanotransferrin and hepcidin also changes in CSF indicating again dysregulation of iron homeostasis in the brain. Our findings support an increase of iron level in the AD brain through PCS but this too needs to be further verified through more studies and phantom experiments.

3.2 ROI analysis in select gray matter region

Tau accumulation is a key factor in Alzheimer's Disease progression [64, 65]. Therefore, we evaluated PCS values of regions primarily affected by tau pathology and altered most during the progression of the disease. ROIs were chosen based on how frequently or severely they are affected by tau pathology based on a review of relevant articles [66, 33, 7, 67, 68, 69]. ROIs included for the analysis were the entorhinal cortex, parahippocampal cortex, amygdala, fusiform gyrus, inferior temporal cortex, middle temporal cortex, superior temporal cortex, posterior cingulate cortex, precuneus, and lingual cortex. Additionally, deep grey matter regions of the caudate nucleus, putamen, and globus pallidus were also included because of their apparent importance found in other QSM literature [51, 49, 70]. Correlation analysis for the ROIs shown in Fig. 3.4 was performed for 48 β-amyloid and tau-positive AD patients only, one β-amyloid and tau-positive AD patient was not included due to FreeSurfer segmentation error. Rstudio [71] (Rstudio, Inc, Boston, MA) 2022.07.2 Build 576 for MacOS and R 4.2.1 were used for all ROI-based statistical analyses including the computation of linear regression and Pearson's correlation coefficient. The p-value was corrected with
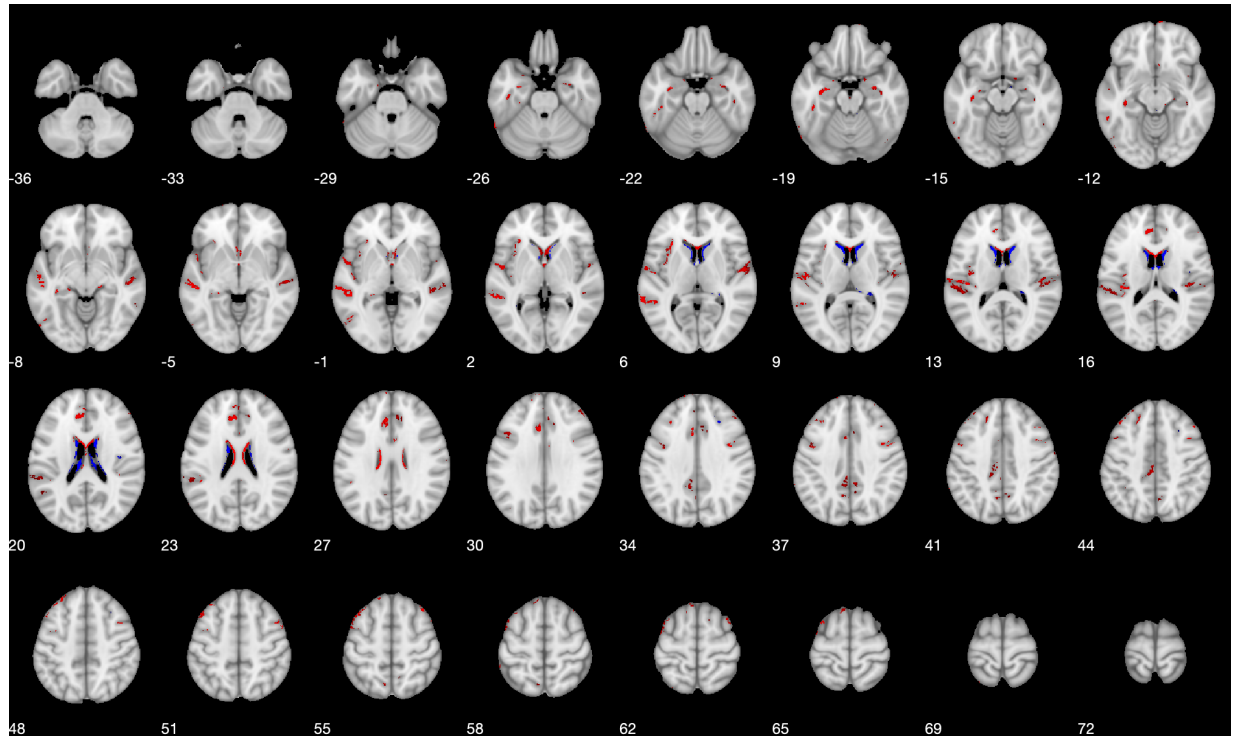
Figure 3.3: Regions of statistically significant ($p < 0.05$) higher (red) and lower (blue) magnitude PCS in the CSF of AD patients compared to the HC participants in MNI space. There are more clusters in higher PCS images for AD group compared to the lower PCS image.

considerations of multiple comparisons with 5000 permutations [72, 73]. For ROI analysis, corrected $p < 0.05(*)$, $p < 0.01(**)$, $p < 0.001(***)$ were considered.

3.2.1   PCS correlated with tau PET measures and age in ROI analysis in the Mayo clinic cohort

In the ROIs chosen, cortical ROIs showed a positive association between PCS and tau PET as shown in Table 3.1 and Fig. 3.5. Even though only a few ROIs survived the significance test based on corrections for multiple comparisons the association is positive for tau PET. This strengthens the hypothesis that tau PET colocalizes with iron. Previously, a positive association between QSM and tau PET was observed in inferior temporal cortex [48]. PCS instead of QSM is used in the current analysis. Arguably, PCS can represent a more accurate measure of iron compared to QSM as PCS does not contain any contribution from any diamagnetic source in voxel level and ROI level. The association between amyloid and PCS is very small for most of the ROIs. It makes sense because these ROIs are known for tau
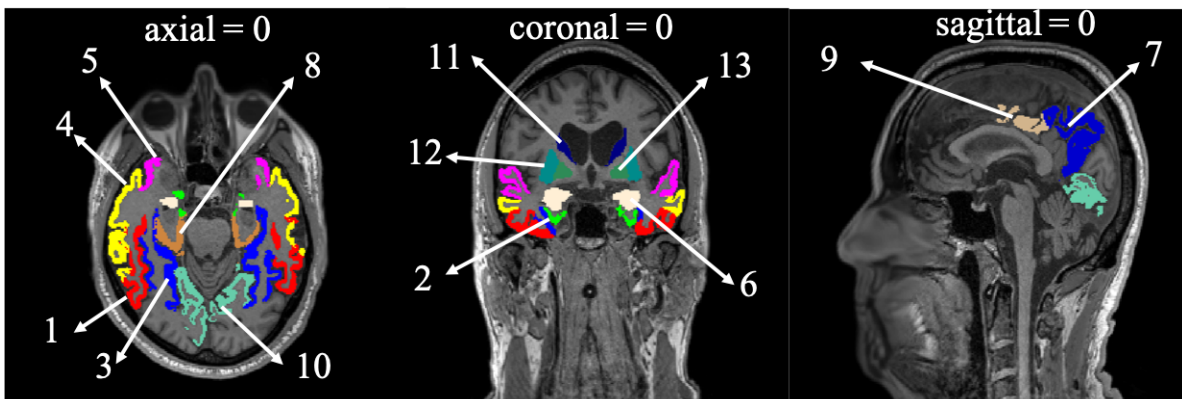
Figure 3.4: Regions included in the correlation analysis. The slice locations are shown designating the midpoint as the origin (0,0,0) of a 65-year-old male amnestic dementia patient's FreeSurfer processed structural image space with a matrix size of 256 × 256 × 256. Here, (1) Inferior temporal cortex, (2) entorhinal cortex, (3) fusiform cortex, (4) middle temporal cortex, (5) superior temporal cortex, (6) amygdala, (7) precuneus, (8) parahippocampal cortex, (9) posterior cingulate cortex, (10) lingual cortex, (11) caudate nucleus, (12) putamen, and (13) globus pallidus.

accumulation, not amyloid.
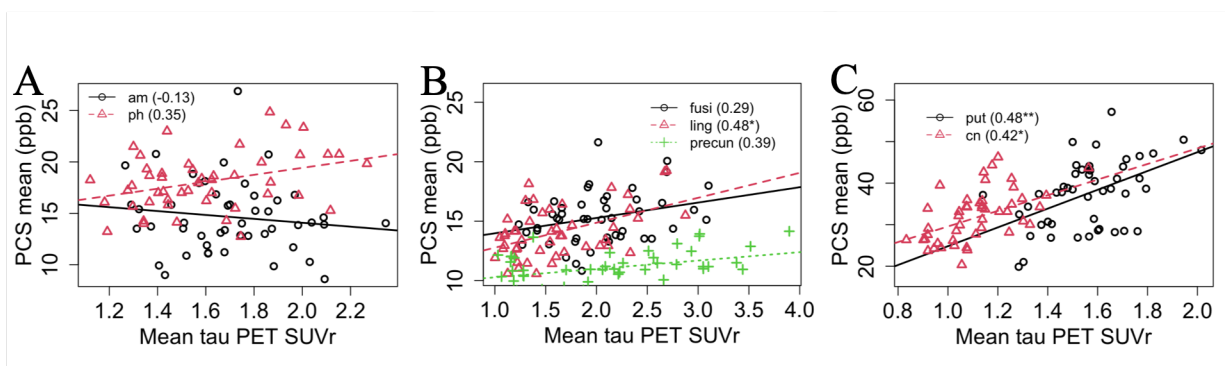
Figure 3.5: (A) Limbic, (B) neocortical, and (C) subcortical regional association between mean PCS and tau PET for selected ROIs. The number in the parenthesis represents Pearson's correlation coefficient. Here, $*p < 0.05$, $**p < 0.01$, $***p < 0.001$, after correction for multiple comparisons using permutation tests. Also, am = amygdala, ph = parahippocampal cortex, fusi = fusiform gyrus, ling = lingual cortex, precun = precuneus, put = putamen, cn = caudate nucleus.

ROI	Pearson's r for PCS and tau PET	Pearson's r for PCS and amyloid PET
Entorhinal cortex	-0.05	0.02
Parahippocampal cortex	0.33	0.1
Inferior temporal cortex	0.21	0.07
Middle temporal cortex	0.15	0.05
Superior temporal cortex	0.21	0.11
Fusiform gyrus	0.29	0.07
Lingual cortex	0.48**	0.12
Precuneus	0.37	-0.01
Posterior cingulate cortex	0.11	0.05
Amygdala	-0.13	-0.01
Putamen	0.49**	0.17
Caudate nucleus	0.43*	0.05
Globus pallidus	0.27	0.08

Table 3.1: Pearson's correlation between amyloid and tau PET and PCS for AD patients for the Mayo clinic cohort.

ROI	Pearson's r for PCS and age for AD patients	Pearson's r for PCS and age for HC participants
Entorhinal cortex	0.12	0.27
Parahippocampal cortex	-0.07	0.1
Inferior temporal cortex	-0.23	0.07
Middle temporal cortex	-0.13	0.06
Superior temporal cortex	-0.17	-0.11
Fusiform gyrus	-0.23	-0.09
Lingual cortex	-0.29	-0.26
Precuneus	-0.27	-0.54***
Posterior cingulate cortex	-0.17	-0.42**
Amygdala	0.39	0.17
Putamen	0.21	0.61***
Caudate nucleus	0.06	-0.02
Globus pallidus	0.25	0.07

Table 3.2: Pearson's correlation between PCS and age for AD patients and HC participants for the Mayo clinic cohort.
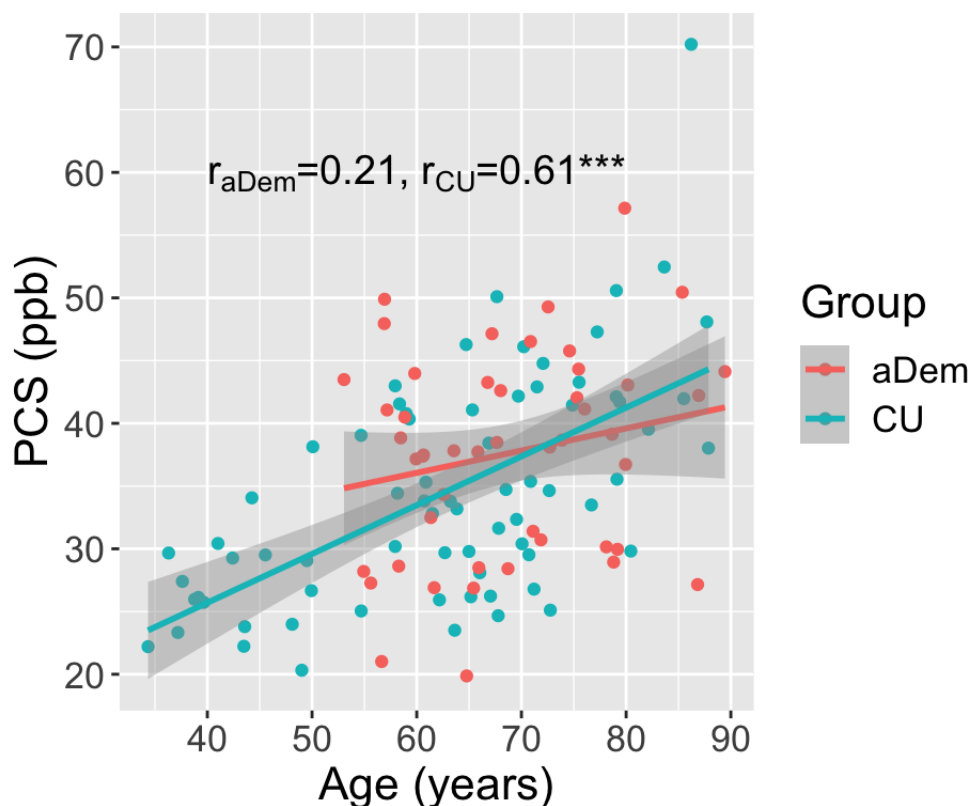
Figure 3.6: Regression line and correlation coefficient between PCS and age for AD patients (aDem) and HC (CU) participants in putamen.

The association between age and PCS is another important measure. In cortical ROIs, the association is mostly negative whereas for AD patients the association strength is very small but positive for HC participants as shown in Table 3.2. In subcortical ROIs, this association strength is positive for both groups however, for the AD group the association strength is much weaker, particularly in Putamen. This putaminal association between age and tau PET is particularly noticeable for AD patients. The iron accumulation is more prominent in HC participants compared to the healthy controls in AD patients for putamen as shown in Fig. 3.6; these two correlation coefficients are significantly different tested using Fisher Z-transform. So, the iron accumulation process in putamen with age is different between healthy control and AD patients. Previously Tiepolt et al [70] showed β-amyloid PET shows a strong negative correlation with average QSM in Putamen, pointing out the importance of putamen in AD pathological progression. In the current analysis importance of putamen is established in terms of the association between age and PCS. These results encourage further study of putamen for understanding AD pathological progression.

The apparent insignificant association between PCS and age is baffling for most other ROIs, particularly in HC participants. However, it should be mentioned that the current study is a cross-sectional one. In a longitudinal study iron accumulation with age may be more prominent, particularly in cortical regions. Also, the iron load in cortical regions is much smaller compared to subcortical regions. Additionally, the number of echo and reconstruction parameters may play a role in determining PCS values. Effects of atrophy and image registration error, and error accumulation during data processing all effects must be considered while explaining these associations. Prospective studies with optimized acquisition parameters are necessary to gain the advantage of this novel separation technique.

3.2.2 ROI analysis in select gray matter region in UCSF cohort

For the sake of reproducibility correlation analysis was performed for a smaller number of scans collected at UCSF MAC (Memory and aging center). The demographic information of the UCSF AD patients is the following; age: 63.3 ± 9.6 (Average $\pm$ standard deviation), MMSE 18:20:23 (1st: 2nd: 3rd quartile), and M/F: 9/6. Multi-echo GRE with 8 echoes data was collected on a SIEMENS Prisma 3T scanner with $TE_1/\Delta TE/TE_8$ of 4/5/39 ms and a native resolution $= 0.86 \times 0.86 \times 2$ mm^3. T_1 weighted structural image was acquired using an MPRAGE sequence with TE/TR of 2.9/2300 ms and a resolution of $1 \times 1 \times 1$ mm^3. The MPRAGE image for each subject was segmented using FreeSurfer 5.3 for normalizing the tau PET images and defining the ROIs for analysis. After intravenous injection of Flortaucipir (FTP, tau PET tracer) and PIB (β-amyloid tracer), CT and tau PET scans were collected and processed using the standard procedure on a Siemens Biograph PET/CT scanner. Details of PET analysis can be found elsewhere [64].

The association between PCS and tau PET is still positive in cortical areas as shown in Table 3.3, however with a much stronger correlation coefficient. It can be noted the sample size is pretty small here so, it is difficult to draw a conclusion. On top of that, the number of echoes is 8 instead of 5 as in Mayo Clinic data, which may affect reconstruction accuracy in DECOMPOSE-QSM. With more echo reconstruction accuracy improves. Basically, more standard sequence design and data collection is needed for future reproducibility studies.

The association between age and PCS seems very small. Given the cohort includes only AD patients, the relationship between age and iron accumulation is complicated. Also, in putamen for both the Mayo Clinic and the UCSF cohorts the small positive association between PCS and age is noticeable.

3.3 Conclusion

The role of iron in AD neurodegeneration is an active field of research. New techniques and more accurate measures are needed to understand iron dyshomeostasis in AD. Through voxelwise comparison of controls and AD patients and the correlation between PET measures and PCS we have established the usefulness of PCS as a meaningful measure of tracking iron-

ROI	Pearson's r for PCS and age	Pearson's r for PCS and tau PET	Pearson's r for PCS and amyloid PET
Entorhinal cortex	0.09	0.29	0.3
Parahippocampal cortex	0.27	−0.04	−0.08
Inferior temporal cortex	0.18	0.56	0.15
Middle temporal cortex	0.14	0.52	−0.34
Superior temporal cortex	0.09	0.61	0.05
Fusiform gyrus	−0.06	0.58	0.22
Lingual cortex	0.57	−0.29	−0.37
Precuneus	−0.41	0.50	0.30
Posterior cingulate cortex	0.23	0.29	−0.23
Amygdala	0.60	−0.1	−0.41
Putamen	0.36	0.77	0.44
Caudate nucleus	−0.02	0.65	0.40
Globus pallidus	−0.45	0.26	0.17

Table 3.3: Pearson's correlation between amyloid PET, tau PET, and age vs PCS for cognitively impaired patients for the UCSF cohort.

related neurodegeneration. Multi-center and longitudinal studies and other benchmarking techniques should be applied to establish the feasibility and understanding of this novel marker.

Chapter 4

Diamagnetic Susceptibility in Neurodegenerative Brain

One of the familiar pathological changes in AD is the accumulation of two proteins in the brain gray matter (GM), namely, β-amyloid in the form of plaques [74, 75] and tau in the form of tangles [76]. Often these plaques and tangles colocalize with iron, e.g., because of undergoing neuroinflammation [77, 48]. In addition to these changes, alteration in the white matter (WM), which may include neurite damage, glial damage, cell death, and eventual atrophy, is known to happen in many neurodegenerative diseases such as AD [63, 78, 79], multiple sclerosis (MS) [80], small vessel disease (SVD) [81] and so on. Recently, many studies [4, 3] have reported β-amyloid content alterations in the cerebrospinal fluid (CSF) in the course of neurodegeneration. Specifically, a decreased level of β-amyloid-42 in CSF has been reported to potentially be a prominent AD bio-marker. Positron emission tomography (PET) imaging is the gold standard to detect β-amyloid in the brain GM clinically using Pittsburg compound (PiB), and tau-protein using Flortaucipir (FTP) [67]; however, PET imaging suffers from low spatial resolution, radiation exposure, and off-target binding [33].

The DECOMPOSE-QSM [14] postprocessing method has been developed to resolve the sub-voxel level susceptibility mixture by calculating the paramagnetic component susceptibility (PCS) and the diamagnetic component susceptibility (DCS) using a signal model with summation of exponentials. PCS is dominantly affected by iron, and DCS can inform pathological changes caused by myelin degeneration, protein aggregation, and other species with diamagnetic susceptibility. While paramagnetic iron accumulation in the brain is one of the widely studied phenomena in healthy aging and neurodegenerative process, it is important to study its counterpart, namely the diamagnetic susceptibility or DCS alteration in AD more extensively.

In the current chapter, we investigate the DCS of the whole-brain volume for cohorts of amnestic dementia (AD) patients and healthy controls (HC). By using voxel-wise group comparison, we show that whole brain differences exist between AD patients and HC participants for all GM, WM, and CSF regions. With β-amyloid and tau PET scans, we hypothesize that the higher voxel-wise |DCS| (the absolute value of DCS) values for AD participants,

relative to controls, in GM, may result from protein aggregations; the observed lower |DCS|
value in WM may be caused by demyelination and in CSF may indicate β-amyloid protein
ratio change. ROI-based correlation analysis suggests demyelination may also happen in the
GM because of tau-protein aggregation.

4.1 Voxel-wise group analysis

Demographic and data acquisition information for this analysis has been presented in Chap-
ter 2. The metric $m_{|\text{DCS}|}$ is defined as follows:

$$m_{\text{PCS}} = \frac{\text{number of voxels with } |\text{DCS}|_{\text{AD}} > |\text{DCS}|_{\text{HC}}}{\text{number of voxels with } |\text{DCS}|_{\text{AD}} < |\text{DCS}|_{\text{HC}}}, \tag{4.1}$$

which estimates the number of voxels with lower |DCS| in AD patient group compared
to the HC participant group in the probability maps after computing group comparisons.
This metric has been computed for all segments of the brain namely GM, WM, and CSF
and reported with corresponding analysis.

4.1.1 AD patients differ from healthy controls at GM in voxel-wise analysis of |DCS|

Whole brain group comparison maps in GM revealed alterations in different regions as shown
in Fig. 4.1 |DCS| maps of β-amyloid and tau-positive AD patients were statistically compared
to β-amyloid and tau-negative HC participants. A higher |DCS| value means a larger amount
of diamagnetic content and vice versa.

The voxel-wise |DCS| value in several grey matter clusters was higher for AD patients
relative to the HC participants as shown in Fig. 4.1. One explanation, for the elevated
|DCS| value, may be the accumulation of the diamagnetic species. Most proteins contain
a high level of paired electrons, hence are diamagnetic. Many efforts have been made to
confirm that disease-related aggregations of the β-amyloid plaques and tau tangles cause
tissue susceptibility changes and can be non-invasively revealed by QSM.

Previously, van Bergen et al. [47] demonstrated that β-amyloid PET SUVr was positively
associated with mean QSM in each different cortical region for every subject and Spotorno
et al. [48] showed tau PET SUVr also was positively associated with regional QSM. The
positive association between PET SUVr and QSM was explained by the colocalization of iron
with the plaques and tangles. However, the missing piece was that the susceptibility sources
were not separated, as a result, the diamagnetic component was likely overwhelmed by the
paramagnetic susceptibility of iron. Gong et al. [82] showed that β-amyloid and tau protein
are diamagnetic and visible through QSM using phantom experiments. Additionally, in the
same study, it is shown that for a human brain specimen with AD, the diamagnetic pattern in
QSM aligns with the histological staining for β-amyloid plaques and tau tangles. Zhao et al.
[83] showed that in AD-diagnosed human hippocampal slices, the aggregations of β-amyloid
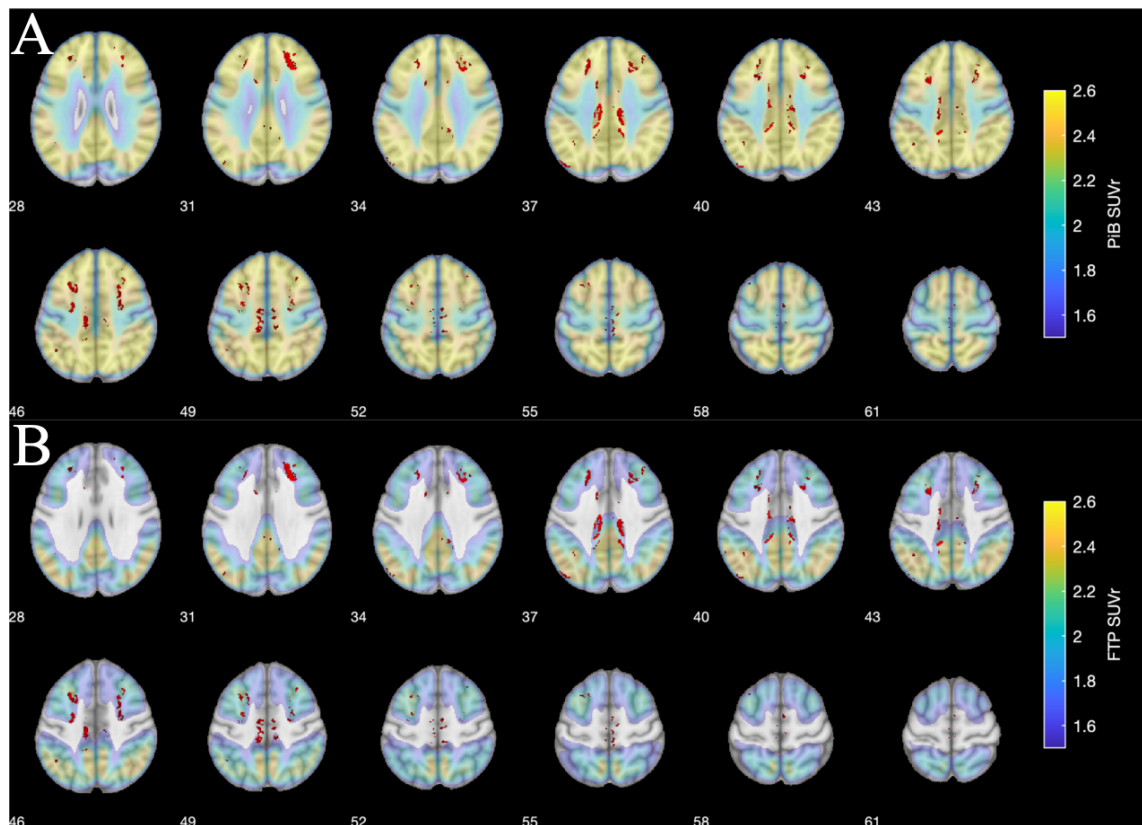
Figure 4.1: Regions of statistically significant ($p < 0.05$) higher |DCS| value (red) in the GM of AD patients vs CU HC overlaid on top of the average β-amyloid PET (A, top two rows) and average tau PET (B, bottom two rows) in MNI space. The clusters of significant differences are primarily located at superior and medial frontal gyri and paracentral gyri. Numbers in the figure denote the slice locations.

and tau cause diamagnetic changes in QSM. In the current work, |DCS| value of β-amyloid and tau-positive AD patients being higher in several regions than that of their β-amyloid and tau-negative HC counterparts may allude to the existence of voxels with accumulated plaques and tangles not just iron.

Further investigation reveals that some of the clusters with higher absolute |DCS| values in AD patients compared to HC participants were either situated in the boundaries of the GM and WM or seemed to appear to have much smaller dimensions compared to the spread of the PET signal intensity as shown in Fig. 4.1 or both. This mismatch of dimension can be attributed partly to the resolution mismatch between PET and DECOMPOSE-QSM.

Fig. 4.2 reveals regions with lower |DCS| in AD patients compared to HC participants. The value of $m_{|DCS|}$ in GM is 0.64; meaning, more voxels show lower than higher |DCS|
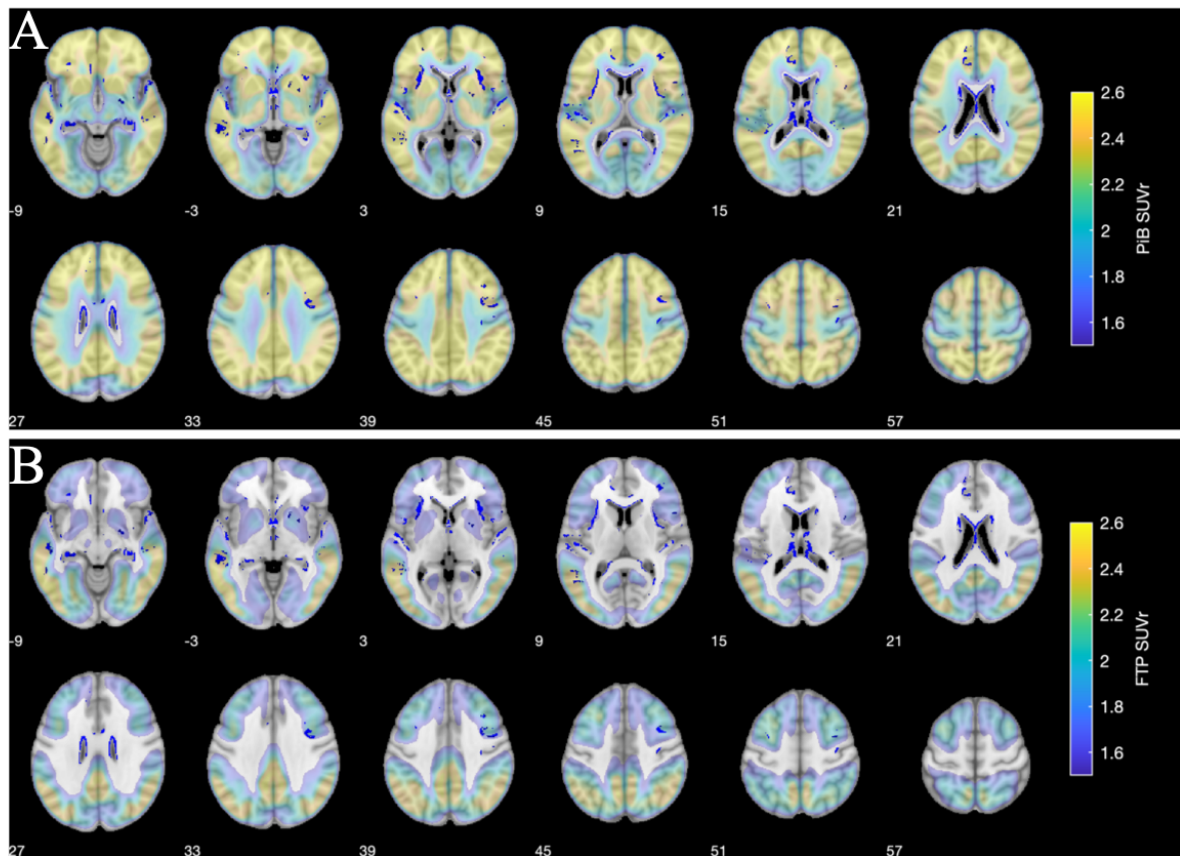
Figure 4.2: Regions of statistically significant ($p < 0.05$) lower |DCS| (blue) in the WM of the AD patients vs CU HC overlaid on top of the average β-amyloid PET (A, top two rows) and average tau PET (B, bottom two rows) in MNI space. A few of the clusters overlap with the highest intensity PET signal, which may correspond to the demyelinated region discussed in section 4.2.1. Some of the clusters reside in tissue segmentation boundaries, particularly in the subcortical and thalamic regions may not be directly associated with the PET signal. However, these differences still can be ascribed to pathological differences between AD and HC groups.

in the GM of AD patients compared to HC participants. It is worth mentioning that the susceptibility is not a direct measurement of the existent β-amyloid or tau protein aggregations, other species such as myelin also contribute to the DCS contrast. Demyelination may result in lower |DCS|. So, in a region depending on the severity and the order of the arrival of either pathological alteration, such as protein accumulation or demyelination |DCS| may show higher or lower values. Similar results and the corresponding discussion are presented in the ROI correlation section.

4.1.2 AD patients differ from healthy controls at WM in voxel-wise analysis of |DCS|

In Fig. 4.3, the area (number of voxels) of the WM with a lower |DCS| value was larger than the area of the WM with a higher |DCS| value in AD patients compared to the HC participants. A lower |DCS| value in AD patients relative to HC participants was observed primarily in the periventricular WM; a higher |DCS| value in the AD group was observed in the frontal WM, corpus callosum (CC), and internal capsule (IC). The value of $m_{|DCS|}$ in GM is 0.34; meaning, more voxels show lower than higher |DCS| in the WM of AD patients compared to HC participants.
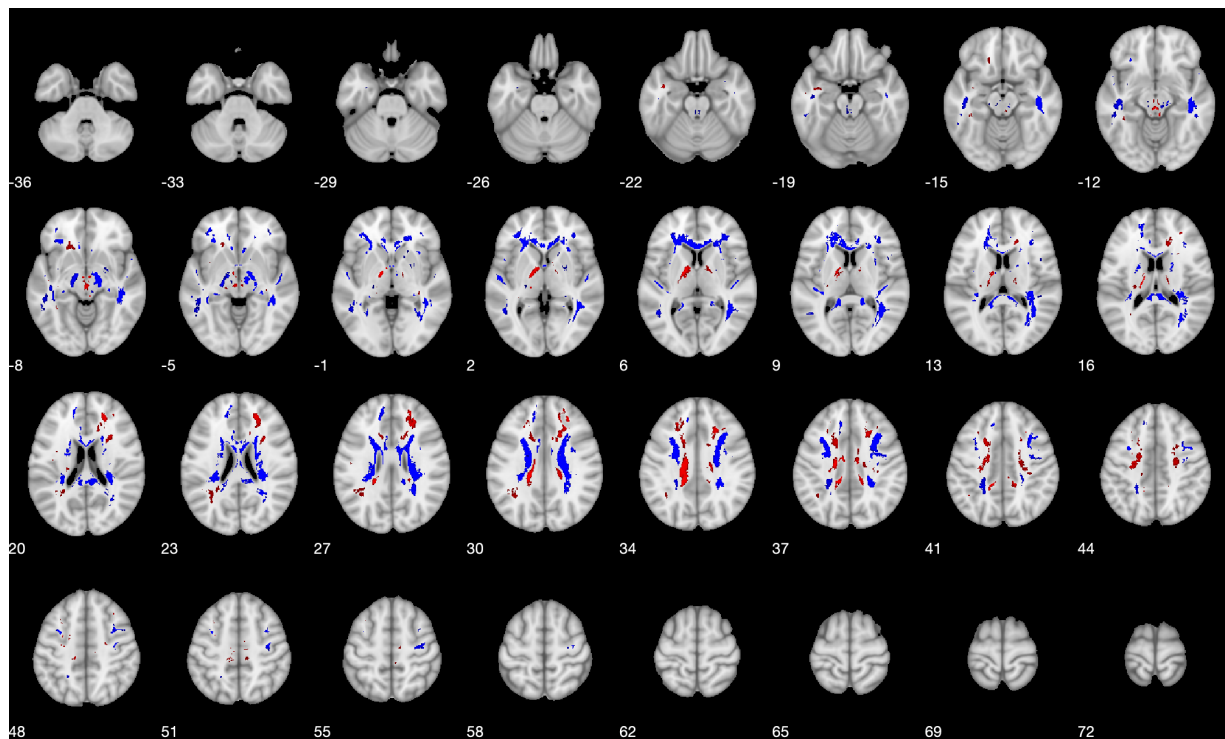
Figure 4.3: Regions of statistically significant ($p < 0.05$) higher (red) and lower (blue) |DCS| value in the WM of AD patients relative to the HC participants in MNI space. Clusters of higher |DCS| values in the AD group are primarily located in the frontal WM, posterior part of CC, and IC. Clusters of lower |DCS| values are predominantly periventricular, and also located in corona radiata and posterior part of CC. Numbers in the figure denote the slice locations.

Shown in Fig. 4.3, regions of both higher and lower |DCS| values are observed for the AD patients relative to the HC participants. A lower trend of |DCS| value indicates a decreased amount of diamagnetic species. Previously, Acosta-Cabronero et al. [51] reported that not

many clusters with lower susceptibility in AD compared to controls were found comparing corresponding QSM. It can be argued, that because non-compartmentalized QSM was used in that work and the number of subjects was very small (19 in total), it was difficult to find significant clusters with lower absolute susceptibility in AD patients. Studying a relatively small number (10) of AD patients Au et al [63] showed an increase of QSM in a very small structure known as hippocampal fimbria ascribing the increase to iron accumulation. In current work some clusters are also seen with higher |DCS| in AD patients in Fig. 4.3, however, the majority (in the number of voxels) of the clusters show lower |DCS| compared to that of HC participants. On top of that, Gong et al [84] showed that lower myelin content is associated with rapid cognitive decline.

Previously in a study by Liu et al., [85] a dramatic reduction of susceptibility in WM was observed in shiverer mice as an indication of the loss of myelination. Meanwhile, diffusion measurements showed intact fiber pathways. Similarly, a decreased diamagnetism (an increase in signed QSM value) in WM was observed by Lee et al. [86] and Wang et al [87] independently through the Cuprizone diet-induced demyelinated mouse model. While the fractional anisotropy (FA) map from diffusion tensor imaging showed the preservation of the axonal structure in the CC, the QSM measured susceptibility was significantly increased (less negative) in CC for the demyelinated mouse model. The QSM value in CC returned to negative during the remyelination process. A study by O'Callaghan et al [10] showed that the WM/GM contrast was reduced for the mouse with tau pathology compared to the wild type. Further, the histology staining revealed the white matter atrophy in CC, and the white matter structure thickness is significantly decreased for tau pathology-affected mice. All the evidence suggests that myelin is the major diamagnetic contribution in QSM contrast in the WM. Previously in various studies [88, 89, 90, 91], as an indication of abnormal myelination, white matter hyperintensities from FLAIR MRI scans were observed for AD patients in various cases [88, 89, 90, 91]. The β-amyloid aggregation in cortical GM is hypothesized to participate in a cascade process and cause WM abnormalities in AD patients [92, 79]. The multi-layered myelin sheath is crucial for the axon to perform proper functions in the nervous system. The loss of myelination would cause axonal damage and eventually affect the behavior [93]. The β-amyloid aggregation in cortical GM is believed to participate in a cascade process and cause WM abnormalities in AD patients [92, 79]. Although the aggregations of β-amyloid and tau proteins happen in the WM as well [94, 10], the PET imaging results suggest that the plaques mostly exist in the GM rather than the WM as shown in Fig. 4.1. The size of plaques is very small relative to the clinical imaging resolution. Therefore, in WM, the dominant cause of WM susceptibility change is the alteration of myelination. With all these considerations, the observed lower |DCS| value in AD patients was likely caused by the loss of myelination during AD progression.

4.1.3 AD patients differ from healthy controls at CSF in voxel-wise analysis of |DCS|

In Fig. 4.4, AD patients showed a lower |DCS| value in most of the CSF region relative to the HCs, clusters residing predominantly in the lateral ventricles and sylvian fissures, but not in the 4th ventricle or basal cisterns. The value of $m_{|DCS|}$ in CSF is 0.19; meaning, more voxels show lower than higher |DCS| in the CSF of AD patients compared to HC participants.
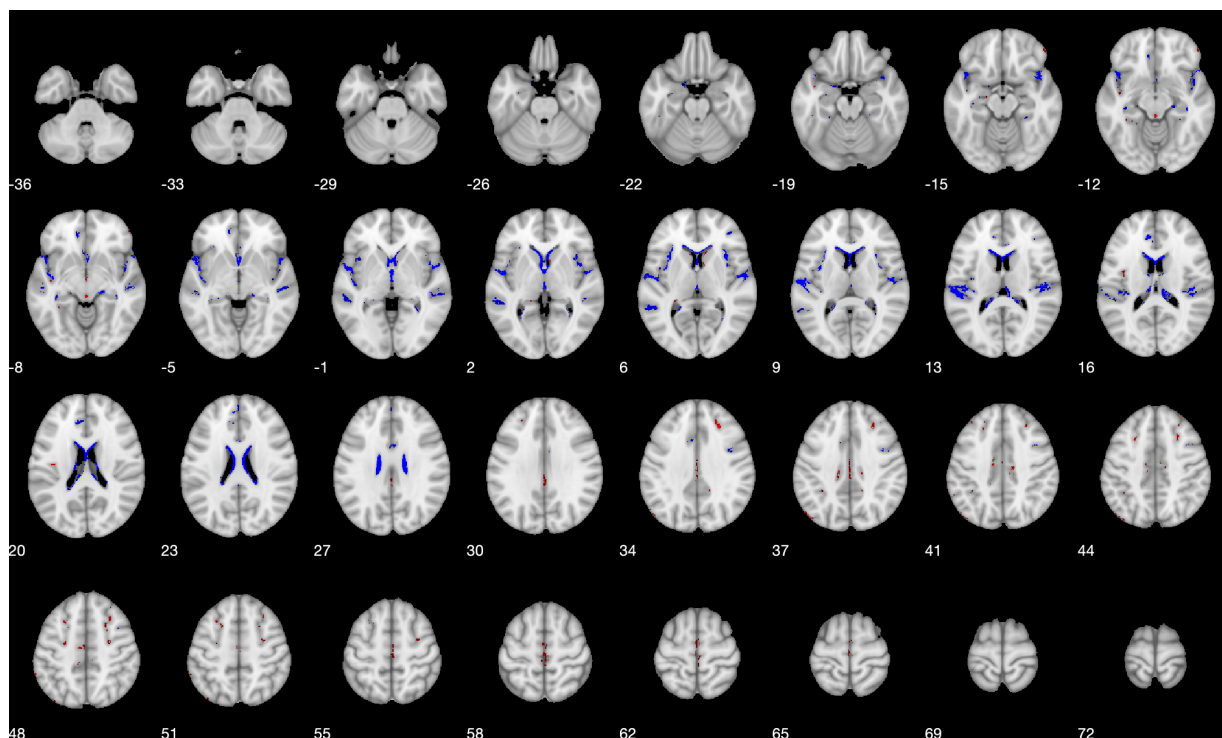
Figure 4.4: Regions of statistically significant ($p < 0.05$) higher (red) and lower (blue) |DCS| value in the CSF of AD patients compared to the HC participants in MNI space. Lower |DCS| value in the AD group relative to controls primarily was observed in lateral ventricles and sylvian fissures. A similar effect was not observed in the 4th ventricle or basal cisterns. Numbers in the figure denote the slice locations.

A lower |DCS| value in the CSF regions was observed for the AD patients relative to the HC participants. CSF serves as the support fluid of the whole brain volume. Through the blood-brain barrier, CSF carries biomolecules such as proteins and peptides that can directly indicate the active inflammation and disease pathologies of the brain. There are many studies focusing on tau and β-amyloid in the CSF as biomarkers for AD [95, 96, 97]. β-amyloid-42 is the dominant component of the plaques seen in AD [98], the decreased CSF β-amyloid-42 or the decrease of CSF β-amyloid-42/β-amyloid-40 ratio has been reported to be superior

in identifying patients with AD [3]. Thal et al showed [99] that the β-amyloid-40 stays unchanged for AD cases. Additionally, the increase of CSF phosphorylated- tau/β-amyloid-42 ratio is shown to be an accurate biomarker for detecting AD dementia [4]. Therefore, the decrease of β-amyloid-42 in CSF may be one of the important contributing factors behind the reduction of the β-amyloid-42/β-amyloid-40 ratio. Although |DCS| maps from DECOMPOSE-QSM cannot give the susceptibility species composition, a decreased trend of the |DCS| value would suggest a reduced total protein content and seems to agree with the report of the decreased level of β-amyloid-42 or the decreased ratio of β-amyloid-42/ β-amyloid-40. However, this finding needs to be verified ideally with CSF samples.

Alternatively, a previous AD study by Choi et al. [100] looked into the choroid plexus (CP), a structure that produces cerebrospinal fluid. It shows that the volume of CP is higher for the AD group compared to the cognitively impaired group while the susceptibility of CP did not show significant change. The changes in the volume of CP could contribute to the observation of |DCS| changes as well, however, the effect is unclear. It is also worth mentioning that the clusters with lower |DCS| values in AD patients compared to HC participants appear to align with the periphery of the ventricles. Impaired barriers caused by ependymal cells and vessels may also play a role in the change of DCS in the CSF region [101]. The bulk magnetic susceptibility in CSF is supposed to be close to zero and its long T_2^* makes susceptibility estimation less reliable. Moreover, partial volume effects, artifacts, and CSF widening can confound the susceptibility metrics. Particularly, enlarged ventricles may be mixed with periventricular tissue that has more diamagnetic susceptibility than CSF during registration with standard brain templates. This partial volume effect would result in CSF voxels in AD patients having higher |DCS|, which, however, was the opposite of what was observed in the CSF analysis in the current work. Therefore, CSF enlargement does not seem to explain the findings. Nonetheless, direct comparison using CSF samples would be necessary to verify and explain our findings.

4.2 ROI correlation analysis

ROI choice details and method has been discussed in section 3.2.

4.2.1 DCS correlated with tau PET measures and age in ROI analysis for the Mayo clinic cohort

In Table 4.1 and Fig. 4.5, in several limbic and cortical ROIs, mean tau PET was associated with mean |DCS| value moderately (Pearson's correlation coefficient > 0.3) or strongly (Pearson's correlation coefficient > 0.5). This relationship may seem contrary to what was observed in Fig. 4.1, where a higher |DCS| value was seen in several GM voxel clusters. However, it should be noted that Fig. 4.1 is showing the voxel-wise comparison between AD patients and controls. On the other hand, Fig. 4.5 and Table 4.1 is showing the ROI correlation for dementia patients between the ROI mean measures. It is possible that in

the ROI level after averaging, only the strongest of the several competing effects dominate mean |DCS|. The competing effects may be protein accumulations [82], cell death [102], atrophy [79], and demyelination [92]. Protein accumulation may increase |DCS| values and demyelination may reduce the |DCS| values. Cell death and atrophy may affect |DCS| values in a complicated fashion that is yet to be explored. The negative direction of association suggests that the demyelination is potentially the leading factor contributing to smaller absolute diamagnetic susceptibility with a larger tau PET signal. Previously, Irimia et al [103] reported a reduction in the T1-w/T2-w ratio (a marker of myelin content) in some frontal and central regions while Pelkmans et al [104] reported an increase of the same in some ROIs including cingulate gyrus, and precuneus. So, conflicting reports have been made on whether demyelination in GM happens measurably using MRI-derived contrast; DCS should be included among one of those contrasts for further investigation. Association between amyloid PET and |DCS|, is very small in most of the selected regions as these regions are primarily affected by tau pathology in the earlier stages of the disease and the cohort contains patients at different stages.

ROI	Pearson's r for |DCS| and tau PET	Pearson's r for |DCS| and amyloid PET
Entorhinal cortex	-0.25	-0.27
Parahippocampal cortex	-0.57^{***}	-0.06
Inferior temporal cortex	-0.11	0.12
Middle temporal cortex	-0.01	0.07
Superior temporal cortex	-0.22	0.04
Fusiform gyrus	-0.48^{**}	-0.006
Lingual cortex	-0.33	-0.14
Precuneus	-0.34	0.15
Posterior cingulate cortex	-0.08	0.03
Amygdala	-0.35	0.07
Putamen	0.08	0.03
Caudate nucleus	0.16	0.27
Globus pallidus	0.28	0.01

Table 4.1: Pearson's correlation between DCS and tau vs amyloid PET for AD patients in the Mayo clinic cohort.

Looking particularly at parahippocampal cortex (ph) and fusiform gyrus the association between |DCS| and tau PET is very strong. AD is marked by drastic changes in laminar structure and cytoarchitecture in PHC [105]. Pyramidal cells in layers III and V of ph are markedly affected by NFTs deteriorating the structural integrity of ph [106]. Intracortical myelin is abundantly present in ph confirmed by T1-w/T2-w ratio [107]. Given the susceptibility of ph in AD both demyelination and structural deterioration may be cautiously
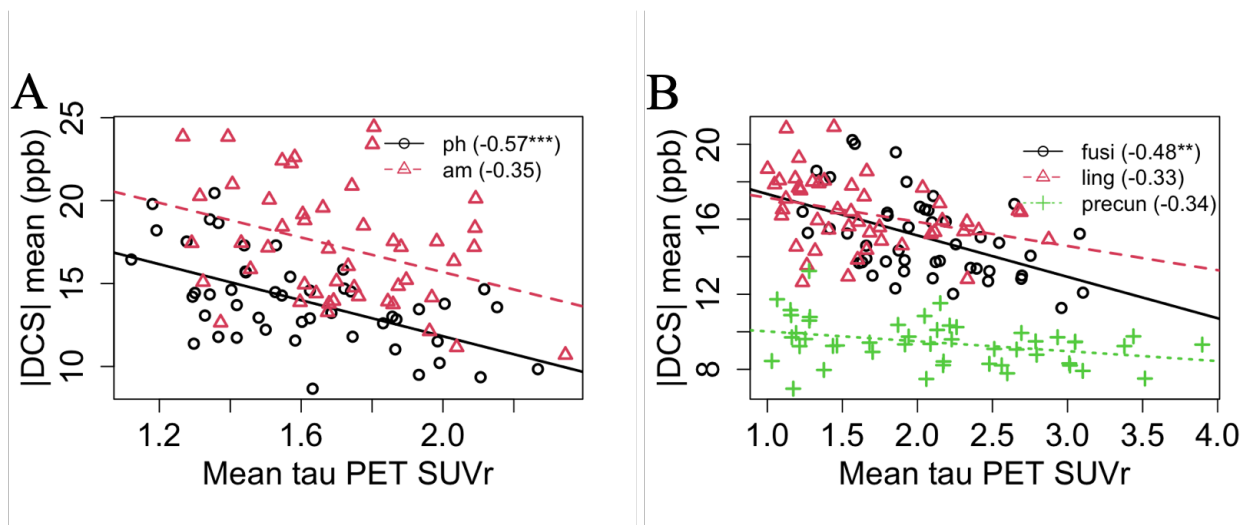
Figure 4.5: Regional association between mean |DCS| and tau PET for selected (A) limbic
and (B) neocortical ROIs. The plot has been subdivided into two subplots for the sake
of legibility. The number in the parenthesis represents Pearson's correlation coefficient.
Here, $*p < 0.05$, $**p < 0.01$, $***p < 0.001$, after correction for multiple comparisons using
permutation tests. Also, ph = parahippocampal cortex, am = amygdala, fusi = fusiform
gyrus, ling = lingual cortex, precun = precuneus regions.

attributed to a very strong correlation between tau PET and |DCS| in this region. In fusiform
gyrus also, the strong association between |DCS| and tau PET is curious as this region is also
very involved in AD progression. Functionally, this region is associated with face recognition
and AD patients show issues with recognition at advanced AD stages [108].

Association between |DCS| and age in AD group is weaker in general compared to HC
participants as evidenced by Table 4.2. If |DCS| were to capture only the effect of myelin,
the relationship presented in Table 4.2 and Fig. 4.6 would have looked more complicated,
to be precise akin to inverse U-shaped, where the myelin would increase with age, then stay
steady for a particular age group, and then decrease with age [109]. However, intracortical
myelination is more complicated compared to white matter myelination [110]. On top of
that structural integrity loss related to protein accumulation and cell death may contribute
to |DCS| too. Hence, the pseudo-linear association between |DCS| and age is intriguing and
needs further exploration for complete understanding.

The difference in the association between age and |DCS| in a few ROIs particularly, in
the posterior cingulate cortex (pcing) and caudate nucleus (cn) is worth mentioning. These
associations are significantly different between AD patients and HC participants. pcing has
been identified as one of the most vulnerable regions in AD pathological progression [111]
and showed significantly reduced gray matter volume (GMV) in longitudinal studies with
AD patients. QSM showed a significant increase in pcing in previous studies [112]. The

ROI	Pearson's r for PCS and age for AD patients	Pearson's r for PCS and age for HC participants
Entorhinal cortex	0.13	0.26
Parahippocampal cortex	0.34	0.29
Inferior temporal cortex	0.17	0.34*
Middle temporal cortex	0.08	0.31
Superior temporal cortex	0.11	0.33*
Fusiform gyrus	0.48**	0.43**
Lingual cortex	0.40	0.26
Precuneus	0.35	0.37**
Posterior cingulate cortex	0.03	0.55***
Amygdala	0.31	0.36*
Putamen	0.52**	0.45**
Caudate nucleus	0.20	0.63***
Globus pallidus	0.36	0.29

Table 4.2: Pearson's correlation between |DCS| and age for AD patients and HC participants for the Mayo clinic cohort.
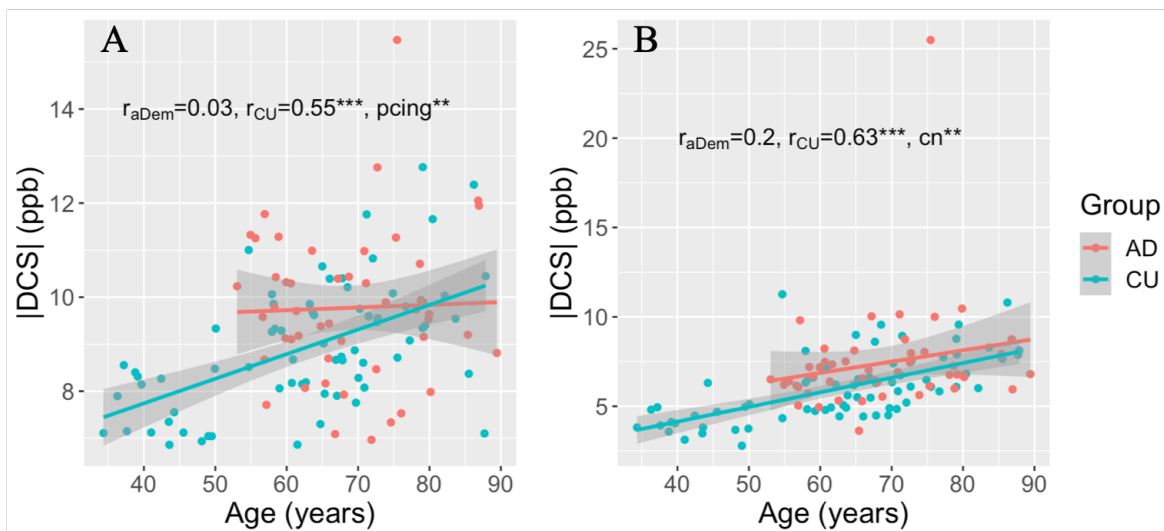
Figure 4.6: Association between |DCS| and age for (A) posterior cingulate cortex (pcing) and (B) caudate nucleus (cn) for AD (aDem) patients and CU HC participants. It should be noted that the correlations are significantly different for each subject group.

fact that |DCS| increases in pcing for HC participants but shows no consistent trend for AD patients is intriguing. If |DCS| is hypothesized as a measure of structural integrity and myelination increase of |DCS| with age can represent the health of certain structures whereas no trend may represent expected change not happening to maintain the health of the structure. A similar comment can be made about cn, as cognitively unimpaired (CU) participants showed higher |DCS| with age but AD patients do not. cn showed a marked increase in QSM previously in AD patients compared to controls [49].

4.2.2 ROI analysis in select gray matter region in the UCSF cohort

Even though the association coefficients as presented in Table 4.3 in the UCSF cohort did not match with the Mayo Clinic cohort certain similarities are noticeable, such as high correlation coefficient between age and |DCS| in fusiform gyrus and all the subcortical ROIs. Also, in precuneus, the association between |DCS| and tau PET has quite similar magnitudes. Most of the other association coefficients are dissimilar, however, the mismatch in the size of the two cohorts and the very small number of subjects in the UCSF cohort should be mentioned.

ROI	Pearson's r for |DCS| and age	Pearson's r for |DCS| and tau PET	Pearson's r for |DCS| and amyloid PET
Entorhinal cortex	0.16	0.12	−0.05
Parahippocampal cortex	0.35	−0.25	−0.35
Inferior temporal cortex	−0.05	0.25	0.02
Middle temporal cortex	0.13	0.46	−0.12
Superior temporal cortex	0.43	0.09	−0.05
Fusiform gyrus	0.63	−0.13	−0.39
Lingual cortex	−0.49	0.15	0.24
Precuneus	0.44	−0.37	−0.14
Posterior cingulate cortex	−0.03	−0.11	0.15
Amygdala	−0.26	0.44	0.21
Putamen	0.41	0.49	0.17
Caudate nucleus	0.61	0.29	−0.17
Globus pallidus	0.75*	0.63	0.09

Table 4.3: Pearson's correlation between |DCS| and age, tau, and amyloid PET for AD patients for the UCSF cohort.

4.3 Conclusion

The diamagnetic compartment DCS from DECOMPOSE-QSM is tested as a marker for the presence of pathology (β-amyloid and tau). It appears DCS is affected in an opposing manner by two important pathological changes, such as protein accumulation and demyelination. In the voxel-wise analysis of the WM, a lower DCS pointed to white matter integrity loss. Voxel-wise analysis results of the |DCS| value in the CSF region may be an indication of the decrease of the β-amyloid-42/β-amyloid-40 ratio in AD. In short, diamagnetic susceptibility may help track several pathological alterations in neurodegeneration.

Chapter 5

Assessing the Predictive Power of Source-Separated Susceptibility

In previous chapters, the importance of PCS and DCS has been established in terms of studying AD pathology. It has been evidenced that PCS and DCS show meaningful physical relations with AD disease pathology. In this chapter, the further potential of these modalities will be explored in predicting different indicators or factors related to disease status. So far, the usefulness of susceptibility in studying mainly tau pathology and iron accumulation has been discussed. Other clinical and genetic factors may have a simple or complex relationship with susceptibility metrics. Previously, it has been shown that when considering the susceptibility values of a region not only the mean value is essential but also other statistics related to the distribution of susceptibility are also important [113]. In previous chapters, voxel-wise analysis and ROI analysis in terms of mean measures have been explored. One of the limitations of voxel-wise analysis is the alteration of values while warping the images from one space to another. On the other hand, while using ROI average, pixel magnitude alteration due to warping is avoided but spatial information is lost. A considerate middle ground would be using distribution statistics for each ROI preserving some spatial information from images in ROI analysis.

5.1   Data demography

A subset of current data has already been used in previous chapters to assess the usefulness of source-separated susceptibility. However, here the full dataset will be used to assess the relationship between susceptibility markers and other relevant information. The detail of the whole dataset is given in Table 5.1. Based on the availability of certain information a subset of this data will be used in different analyses to follow. One AD and one MCI patient were excluded from analyses because of segmentation errors.

Variable	AD patients (n=56)	MCI patients (n=69)	CU HC participants (n=100)
Male/female	27/29 (48%/52%)	39/30 (57%/43%)	58/42 (58%/42%)
Age	68 (60, 77)	77 (72, 89)	68 (59, 77)
STMS	22 (18, 28)	32 (29, 33)	37 (35, 38)
Education	16 (13, 16)	15 (12, 16)	16 (14, 16)
ApoE4 status	37/15/14	20/44/5	27/73/0

Table 5.1: Demographic details of all participant data. Age, STMS, and education are displayed as median (1st quartile, 3rd quartile). ApoE4 status is displayed as positive/negative/not available. STMS: Short Test of Mental State, MCI: Mild Cognitive Impairment, CU: Cognitively Unimpaired, HC: Healthy Control.

5.2 Susceptibility metrics and diagnosis

One of the objectives of relating susceptibility to other pathological markers is to use it to potentially improve diagnosis. With that in mind, here the most known and relatively less used metrics will be associated with diagnoses.

5.2.1 Mean susceptibility measures differentiates subjects from patients

Mean ROI susceptibility values can be very useful to compare patient groups. In the following analysis three different measures of susceptibility namely QSM, PCS, and DCS of each group of AD patients, patients with MCI, and CU HC participants. Groups were compared based on average (mean) ROI susceptibility. Benjamini-Hochberg (BH) correction was applied to assess significance and data analysis was performed in R.

In Fig. 5.1 Significant ROI QSM difference was seen in gp and mte in between AD and HC subjects; fusi, ite, and precun between AD and MCI subjects; and fusi, mte, pcing, and precun between MCI and HC subjects. Previously, cn and put showed significant differences between AD and MCI groups using 30 AD patients and 30 HC participants [49]. In another study by Kim et al [112] showed a significant difference in QSM between AD and amnestic MCI (aMCI) subjects in am; between AD patients and cognitively neutral (CN) subjects in am, precun, and pcing; and between aMCI patients and CN subjects in precun and pcing using 19 AD patients, 19, aMCI patients, and 19 CN subjects. Differences between previous studies and the current one can be attributed to the number of patients, reconstruction approaches, and approaches used to compare different groups. In the current analysis the number of AD patients used was 55, that of MCI patients was 68, and of HC participants was 100. So, the current study uses much more participants compared to previous ones. However, because of the retrospective nature of the study, the groups were not matched in
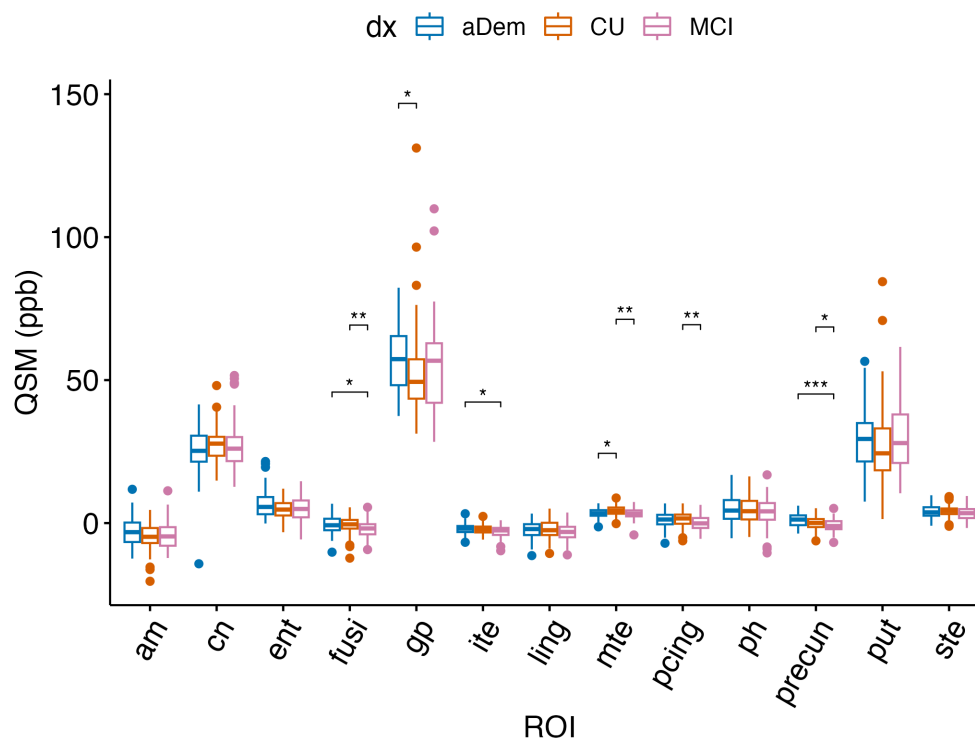
Figure 5.1: Group comparison between AD or aDem patients, MCI subjects, and CU HC participants based on QSM. Here, am = amygdala, cn = caudate nucleus, ent = entorhinal cortex, fusi = fusiform gyrus, gp = globus pallidus, ite = inferior temporal cortex, ling = lingual cortex, mte = middle tempral cortex, pcing = posterior cingulate cortex, ph = parahippocampal cortex, precun = precuneus, put = putamen, ste = superior temporal cortex. Mean ROI QSM in gp and mte are significantly different in AD patients and CU participants; in fusi, ite, and precun between AD and MCI patients; and fusi, mte, pcing, and precun between MCI patients and CU participants.

the case of subject numbers, age, and other relevant covariates. On top of that, variation interpretation of statistical significance can make explanations of findings more complicated. Last but not least, QSM was interpreted as a measure of iron in the previous studies, which may not be entirely accurate because of the contribution from diamagnetic sources. Similar to previous works, it was encouraging to see differences between the groups picked up using QSM even though QSM itself may not be the most accurate measure of iron.

When mean PCS is used, a few ROIs can separate AD, and MCI patients and HC participants as shown in Fig. 5.2. AD patients and HC participants showed significantly different PCS in am and gp; MCI and AD patients showed that in pcing, and precun; and MCI patients and HC participants showed the same in pcing. Remembering, the analysis

in chapter 3 in precun and pcing PCS showed an association with age in amyloid and tau-
negative HC participants but none in amyloid and tau-positive AD patients. Considering
these complicated associations between age and diagnoses we have introduced more holistic
models in the next subsection.
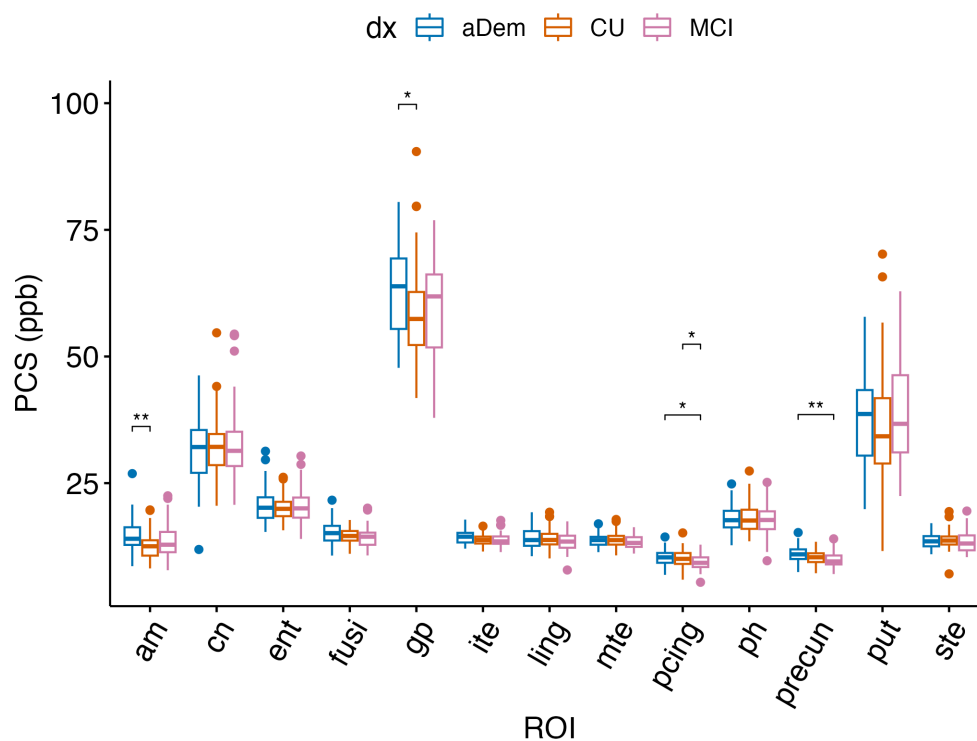
Figure 5.2: Group comparison between AD or aDem patients, MCI subjects, and CU HC
participants based on PCS.

In Fig. 5.3 |DCS| is compared between different groups, significant differences were seen
between AD patients and HC participants in cn and mte. Also, HC and MCI participants
showed significant differences in cn, fusi, gp, ite, mte, pcing, put. Finally, MCI and AD
patients showed significant differences in ent, gp, precun, put. Again, age dependence of
|DCS| should be considered before reading into these differences.

In this simple analysis based on ROI mean susceptibility measures difference between
patients and controls was established. This exercise also prompted the asking of the question
of whether these differences can be exploited further and used in accordance with other
covariates to differentiate patients from controls. In the next subsection more, complicated
models are proposed and discussed to utilize these differences based on ROI susceptibility
metrics.
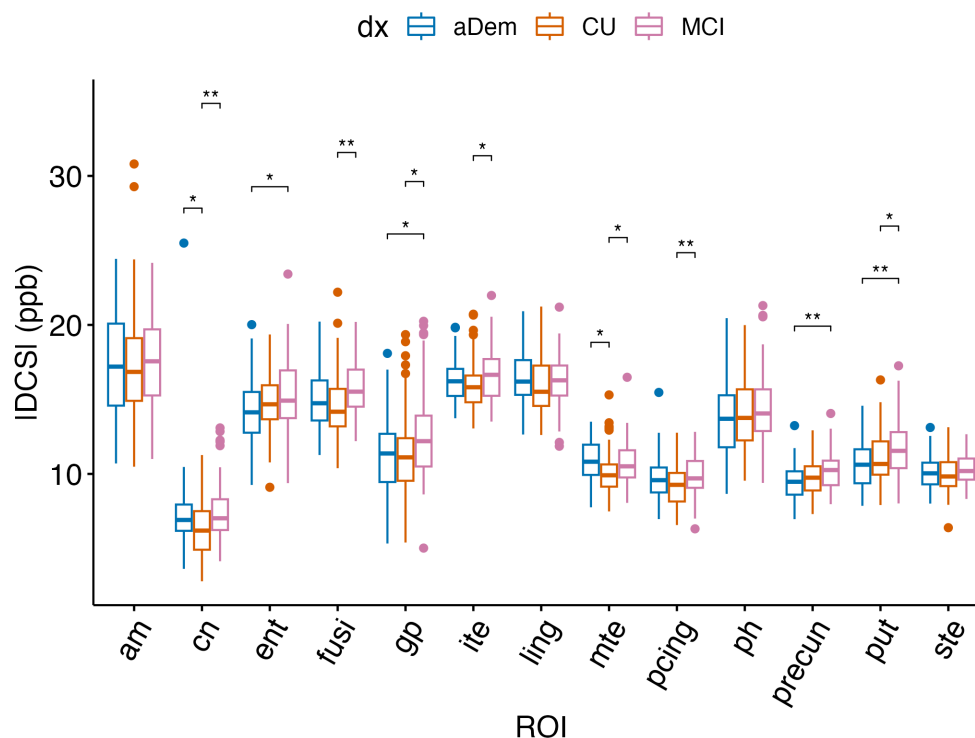
Figure 5.3: Group comparison between AD or aDem patients, MCI subjects, and CU HC
participants based on DCS.

5.2.2 Data-driven model using susceptibility metrics for moderately successful diagnosis

The results in the previous section though inspiring, brings into question the usefulness
of these comparisons because not all the available and necessary covariates were included.
More intricate models are needed to compare the groups to include different variables of
interest. Besides only mean values of corresponding susceptibility metrics were used in that
analysis. It may be hypothesized that the inclusion of other distribution parameters will
either increase accuracy or decrease inherent bias resulting from using one covariate. With
this in mind, a few approaches have been used to assess the separability of patient groups
based on different susceptibility metrics. A few things have been tested in the subsequent
analysis.

- Linear discriminant analysis (LDA) was used for classification because of its stability
  and superior performance for multiclass classification compared to logistic regression
  in the case of a small dataset such as the current one. The objective was not to find

the best classifier, it was to choose a good enough classifier so that effect of introducing
new parameters can be understood [114]

- In the first model, the separability of subject groups based on mean ROI QSM and
  age were computed

- In the second model, the separability of subject groups based on QSM distribution
  parameters (mean, variance, skewness, kurtosis, 75th percentile, and 90th percentile)

- In the third model, combined QSM and DECOMPOSE-QSM measures were used to
  assess the improvement of classification between subject groups.

- All the analyses were performed in the chosen ROIs discussed in previous sections to
  decide which ROIs demonstrate better classification accuracy

As described in previous ROI analysis, mean, variance, skewness, kurtosis, 75th percentile, and 90th percentile of QSM, PCS, and DCS values were extracted using in-house MATLAB code. The extracted ROI features were saved in comma-separated value (csv) files and the later part of the processing was performed in Jupyter Notebook using Python 3 [115]. In Python data was divided into training and test sets using the default ratio set by the program and standardized using MinMaxScaler() method. The program was run with a fixed random seed for reproducibility.

| ROI | Area under the curve of the receiver operating characteristics (AUC) | | | | | | | | |
| | Age & QSM | | | QSM dist. param. | | | All dist. param. | | |
	HC	MCI	AD	HC	MCI	AD	HC	MCI	AD
Ent	0.6	0.70	0.52	0.60	0.65	0.55	0.68	0.67	0.68
Ph	0.65	0.70	0.50	0.57	0.66	0.38	0.48	0.58	0.49
Ite	0.62	0.66	0.63	0.64	0.67	0.54	0.71	0.69	0.63
Mte	0.71	0.71	0.65	0.70	0.66	0.60	0.69	0.63	0.77
Ste	0.65	0.69	0.53	0.70	0.63	0.60	0.74	0.59	0.69
Fusi	0.66	0.69	0.55	0.70	0.68	0.46	0.70	0.68	0.48
Ling	0.65	0.70	0.59	0.61	0.70	0.55	0.63	0.66	0.53
Precun	0.68	0.70	0.67	0.78	0.65	0.71	0.81	0.66	0.73
Pcing	0.66	0.71	0.56	0.62	0.71	0.48	0.64	0.71	0.52
Am	0.69	0.69	0.58	0.76	0.73	0.84	0.79	0.76	0.85
Put	0.65	0.72	0.70	0.71	0.67	0.68	0.73	0.59	0.77
Cn	0.65	0.71	0.61	0.74	0.73	0.72	0.67	0.67	0.60
Gp	0.67	0.67	0.68	0.68	0.71	0.69	0.70	0.68	0.72

Table 5.2: Classification performance between AD, MCI, and HC participants using Linear Discriminant Analysis (LDA).

In Fig. 5.4, and Table 5.2 ROC analysis of the chosen ROIs is presented. One disclaimer
is, none of the classifiers showed exceedingly high (> 0.9) AUC value. However, there are
definitely some standouts in terms of ROI and chosen model. In each subpanel, the leftmost
classifiers used only mean ROI QSM and age as features; the middle one used all the QSM
statistics mentioned previously at the beginning of this section, and age; and the rightmost
uses all QSM, DCS, and PCS statistics and age.
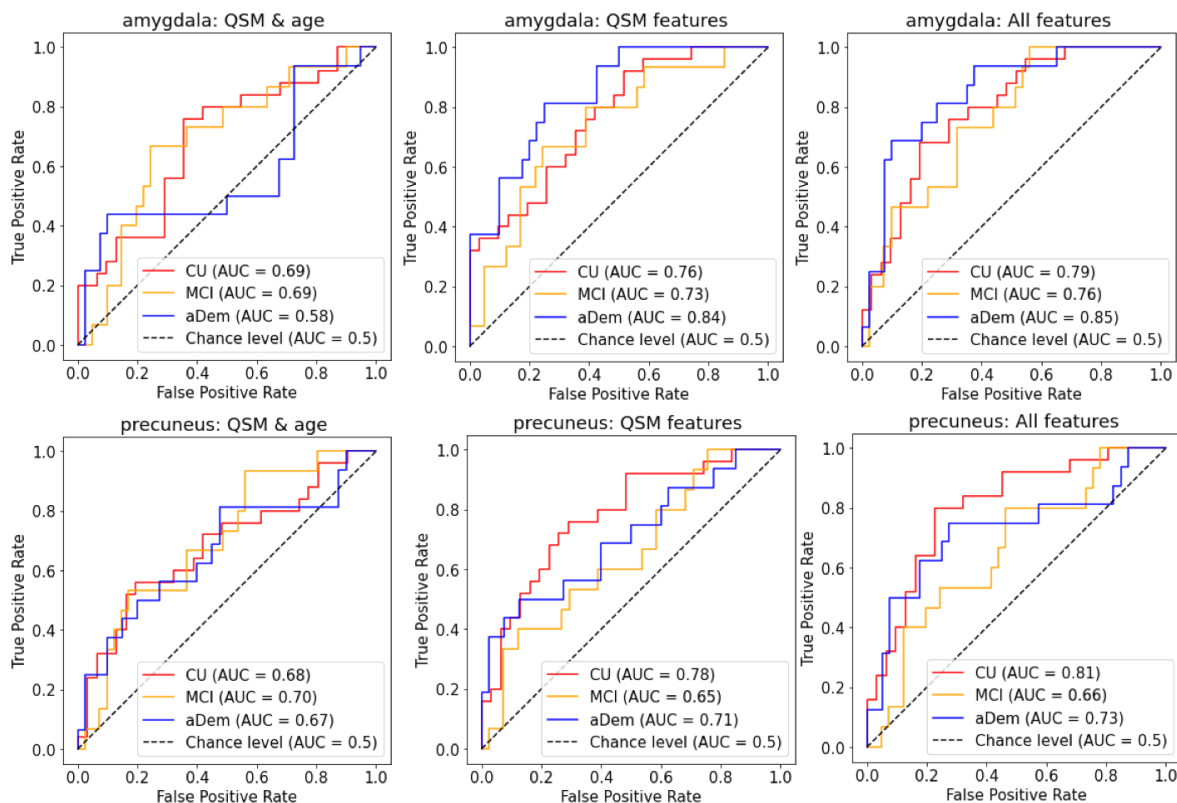
Figure 5.4: ROC curve in amygdala and precuneus using LDA for classifying AD, MCI
patients, and HC participants.

In chapters 3 and 4 precuneus showed a moderately strong (> 0.3) association between
both PCS and tau PET and |DCS| and tau PET for AD patients. Precuneus PCS also showed
a very strong association with age for HC participants. On top of that other distribution
parameters have been added to the current model which may have an association with
disease. Hence, acceptable separability is observed between HC and AD groups in precuneus
as shown in Fig. 5.4. Previously, precuneus has been shown to demonstrate a difference in
QSM values between AD patients and HC participants as mentioned already [112] and this
region was chosen for analysis because it is affected by tau pathology. This region is part
of the default mode network and has been shown to be affected by amyloid pathology early

in the disease [116]. So, affected by amyloid, tau, and iron pathology and related to default brain function this region deserves further study using susceptibility and other measures. A longitudinal study of alteration in this region may reveal further information about disease progression.

Another important observation is that the subcortical ROIs showed quite improved AUC when only QSM distribution parameters is incorporated in the model, whereas cortical ROIs shows improved AUC when all the parameters are included. Because subcortical ROIs are known to accumulate iron, QSM itself in these regions is a more representative measure of iron, and QSM and PCS values are less different from each other. The effect of DCS in diagnostic for the subcortical ROIs was much less prominent compared to the cortical regions.

Am showed group differences in PCS contrast, and it held the difference after introducing improved models and other variables. Previous works [51, 112, 117] reported pronounced QSM increase in subcortical ROIs such as am, put, and cn in AD. Particularly [118] am in AD has shown widespread gliosis, neuronal death, structural change, and atrophy. So, it is not surprising that by introducing all the susceptibility parameters the performance of amygdala in separating subject groups improves substantially. As mentioned earlier other deep gray matter regions such as put and cn performed well with QSM parameters only because these regions are saturated with iron, particularly in the aged patient group, so QSM acts as a proxy measure of iron in these regions.

In summary, the classifiers presented in this section is not present very high AUC values, yet they revealed moderate sensitivity towards better classification which can be used in the future in combination with other modalities for improved diagnosis.

5.3 Susceptibility metrics fails to associate with ApoE4 status

ApoE4-carrying individuals show a higher propensity to develop AD [119, 5]. Hence, the susceptibility metrics could be assessed in terms of their efficacy to be related to ApoE status. In this subsection, this was investigated using different models.

5.3.1 Simple difference based on mean

Using just mean ROI measures neither QSM, PCS, and DCS could show any difference between ApoE4 positive vs negative subjects as shown in Fig. 5.5, Fig. 5.6, and Fig. 5.7.
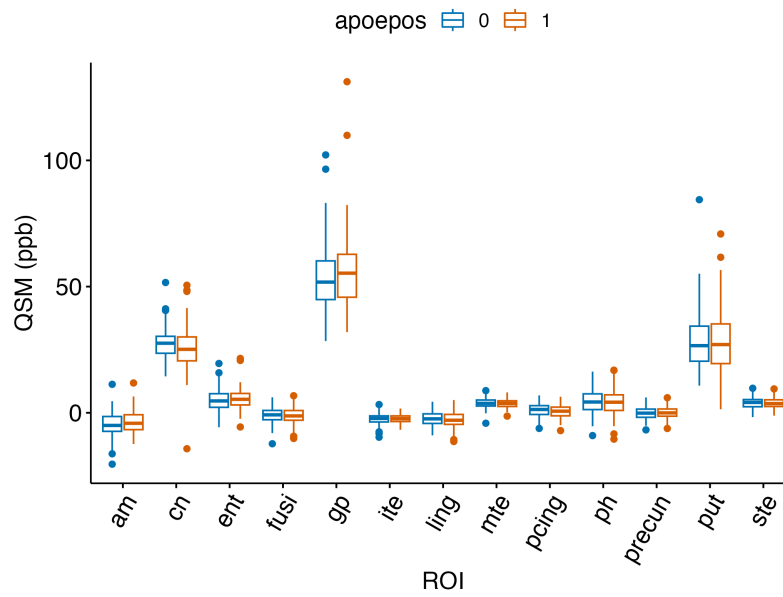
Figure 5.5: Comparison of ApoE4 status based on QSM.
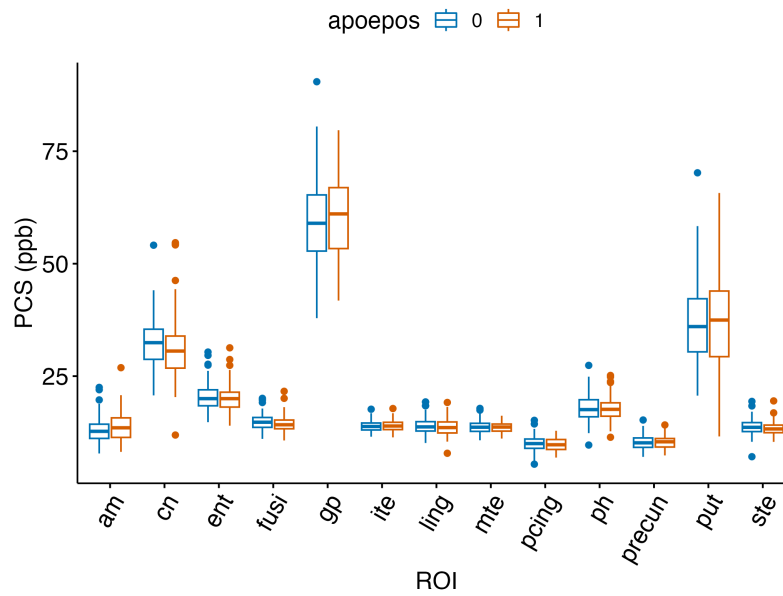
Figure 5.6: Comparison of ApoE4 status based on PCS.
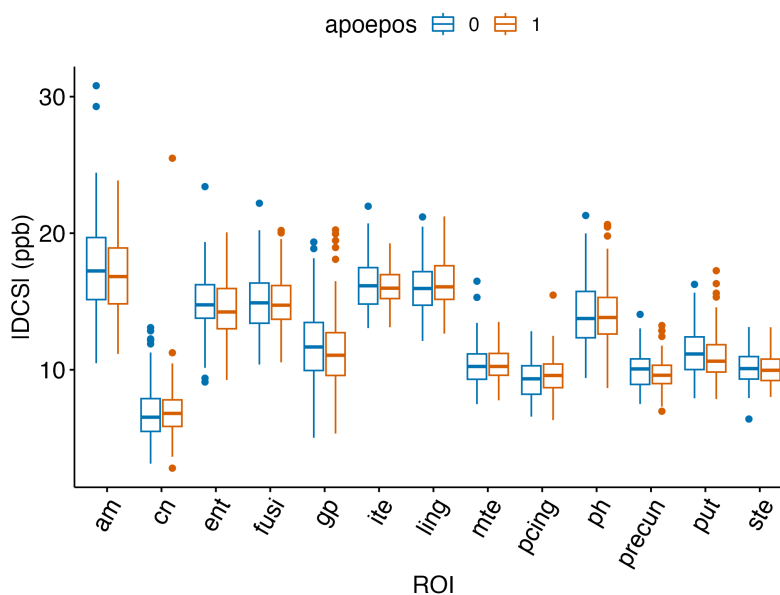
Figure 5.7: Comparison of ApoE4 status based on DCS.

5.3.2 Other models fail to associate susceptibility statistics with ApoE4 status

For the sake of completeness susceptibility statistics were input into three different classifiers as shown in Table 5.3. Logistic regression was chosen because of its ubiquitous use and flexibility. Gaussian Naïve Bayes (GNB) was chosen because it can work with smaller datasets. LDA was used because of its capacity to reduce dimensionality without heavily depending on data collinearity. None of the classifiers or ROIs showed too much of a selectivity to ApoE4 positivity. GNB performed a little better in terms of AUC but it's the assumption that all the features are independent may not be true in the current situation [120]. The entorhinal cortex demonstrated the highest AUC obtained using GNB classifier with very subpar AUC values.

Previously, ApoE4 carriers 65 years and older showed higher hippocampal and amygdalar QSM compared to ApoE2 carriers and for less than 65 years old subjects the difference was only in hippocampus in the UK Biobank study [121]. The current study contains a much smaller number of participants and subgrouping subjects based on age would reduce the power of analysis even further. It will be interesting to increase the number of subjects in future studies and test the reproducibility of said differences reported by Talia et al [121] . The conclusion from the current study is in the selected ROIs no difference is observed in terms of ApoE4 status whether using only mean susceptibility or a comprehensive set of susceptibility statistics.

| ROI | AUC | | | | | |
| | LDA | | Logistic regression | | GNB | |
	QSM stat.	QSM, PCS, and DCS stat.	QSM stat.	QSM, PCS, and DCS stat.	QSM stat.	QSM, PCS, and DCS stat.
Ent	0.53	0.57	0.6	0.63	0.62	0.71
Ph	0.60	0.55	0.58	0.59	0.59	0.58
Ite	0.47	0.44	0.42	0.37	0.51	0.46
Mte	0.38	0.52	0.39	0.43	0.43	0.49
Ste	0.61	0.58	0.51	0.60	0.64	0.68
Fusi	0.47	0.47	0.43	0.47	0.64	0.66
Ling	0.45	0.39	0.44	0.45	0.55	0.50
Precun	0.39	0.56	0.46	0.43	0.52	0.51
Pcing	0.48	0.43	0.53	0.58	0.62	0.69
Am	0.55	0.58	0.50	0.48	0.55	0.48
Put	0.50	0.56	0.43	0.58	0.50	0.58
Cn	0.46	0.57	0.56	0.64	0.65	0.61
Gp	0.40	0.51	0.42	0.42	0.57	0.49

Table 5.3: Classification of ApoE4 status based on QSM, and other parameters.

5.3.3 ApoE4 based voxel-wise group comparisons differentiates healthy controls in small front white matter cluster

All subjects with known ApoE4 status were compared based on their ApoE4 positivity. Also, separate comparisons based on diagnosis were also made, for example, ApoE4 positive HC subjects were compared to ApoE4 negative HC, ApoE4 positive MCI patients were compared to ApoE4 negative MCI patients, and ApoE4 positive AD patients were compared to ApoE4 negative AD patient. Details of voxel-wise group comparison can be found in chapter 4. Only ApoE4 positive HC participants showed clusters of significant difference with ApoE4 negative subjects, other comparisons resulted in no significant clusters. Difference clusters between ApoE4 positive vs negative HC subjects resided mostly on the frontal white matter as presented in Fig. 5.8. Microstructural deterioration associated with ApoE4 positivity has been reported before [122]. However, why the difference was not found in other patient groups and why the only difference was found in small WM clusters needs further investigation.
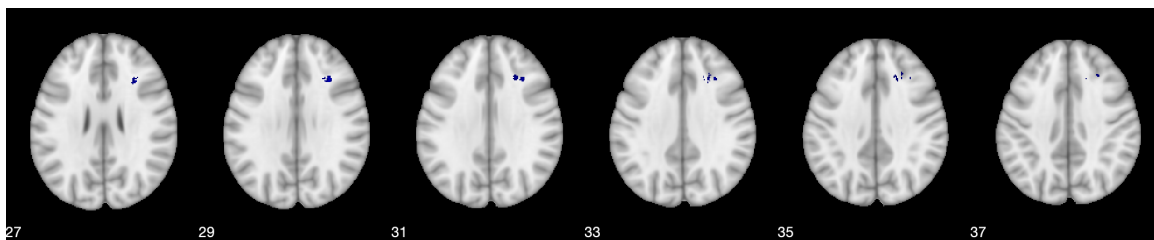
Figure 5.8: Significantly different clusters with lower PCS in ApoE4 positive healthy subjects compared to ApoE4 negative healthy subjects in the frontal white matter.

5.4 Susceptibility metrics explains tau positivity moderately well

As mentioned earlier tau PET is correlated with cognitive status. The prediction of tau PET status with susceptibility metrics is important and hence included in this section.

5.4.1 Linear models for tau PET

In Fig. 5.9 the models for all HC participants are compared. Models with all features have the highest adjusted R-squared (adjR). In terms of the Akaike information criterion (AIC) the models have variable performance. To explain, adjusted R-squared is a measure of how well the models perform to fit current data [123]. AIC takes noise in the data into consideration and gives an estimate of how the model will perform with new data [124]. The higher the adjR and the lower the AIC the better the model. It is not surprising that with more features adjR increases for almost all the models, but AIC is not always the lowest for models with the largest number of variables or features.

One important point is the value of adjR is pretty small for all the models meaning none of the models are doing extremely well in terms of explaining the variances in tau PET SUVr. The majority of the participants (139 of 223) included in Fig. 5.9 do not have any specific tau accumulation in the cortical regions. Hence the small adjR, explains the absence of tau PET signal and the corresponding non-existent pathology across all the subject groups.

A subset of all subjects was chosen based on tau positivity containing 84 subjects. Tau-positive subjects were selected based on a tau-PET meta ROI median SUVr threshold of 1.29 [125]. When only the tau-positive subjects are used in multiple regression analysis adjR values increase substantially as shown in Fig. 5.10. In terms of adjR model using all susceptibility features shows superior performance in general as expected. In terms of AIC the base model performs the best for almost all the ROIs even though all the models have AIC values quite close to each other.

Interestingly, superior temporal cortex (ste) showed the lowest AIC and highest adjR in the model with all the parameters. Alteration in the connectivity in ste has been associated

Figure 5.9: Comparison of multiple regression models for tau PET using different subsets of susceptibility features for all participants. Here, the adjusted R-squared (adjR) and Akaike information criterion (AIC) of each model for all the ROIs are presented. Also, 'base': model with age and ROI QSM as independent variables, 'QSM': model with age and QSM features as independent variables, and 'All': model with age and all QSM, PCS, and DCS features as independent variables.

Figure 5.10: Comparison of multiple regression models for tau PET using different subsets of susceptibility features for 'tau positive' participants.
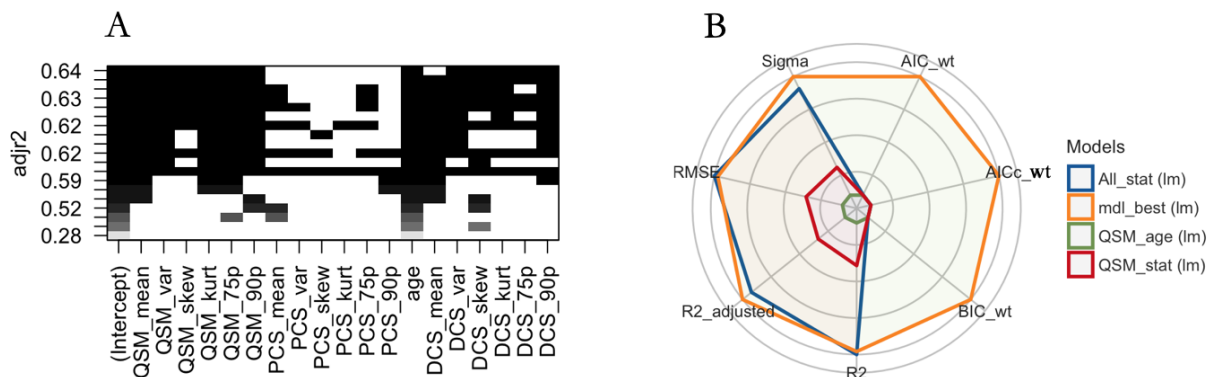
Figure 5.11: Choosing the best model in superior temporal cortex. (A) adjR value of an exhaustive set of models containing combinations of all independent variables (age, QSM, PCS, and DCS features) and (B) performance comparison of all the models including the best model (mdl_best) found using the model resulting in the highest adjR value in (A).

with the change of predictive coding in tau-positive subjects in a recent study [126]. Even though all the selected regions are affected markedly by tau pathology in AD for some reason in the current cohort susceptibility metrics explain tau accumulation quite well with adjR value of (0.61) on a model using all relevant susceptibility metrics mentioned in this chapter as shown in Fig. 5.10 (model denoted by 'All'). In comparison, the model containing only age and mean ROI QSM ('base') had an adjR value of (0.31) and the one containing age and QSM statistics ("QSM") had an adjR of (0.4).

Further analysis on ste multiple regression was warranted to find a more robust set of parameters to explain tau PET SUVr in this region. For this 'leaps' package in Rstudio was used [127]. In Fig. 5.11(A) the blackened fields in the top column presented the relevant parameters needed to achieve highest adjR. These parameters are age, mean QSM, variance, skewness, kurtosis, 75th and 90th percentile of QSM, and |DCS|. The performance evaluation approach [128] shown in Fig. 5.11(B) demonstrated that the best model ("mdl_best") achieved the highest performance in terms of all relevant performance statistics. In this figure, all the statistics are weighted in a way so that the model that has spiderweb corners furthest from the center has the best statistics and hence it is the best model. The best model had an adjR value of 0.63 highest among all of the models presented.

Overall, the susceptibility metrics showed very good performance in terms of adjR in explaining tau PET SUVr. Even though the adjR values were not too high (> 0.8) it was encouraging to see different susceptibility statistics not just the mean QSM has a meaningful

association with tau accumulation.

5.5 Susceptibility metrics weekly explains amyloid positivity in chosen ROIs

Using similar linear models amyloid accumulation was not explained too well with susceptibility metrics as presented in the following subsection.

5.5.1 Linear models for amyloid PET

The regions chosen are more affected by tau accumulation compared to amyloid. Hence all of the regions resulted in small adjR for the whole cohort or the amyloid-positive subjects as shown in Fig. 5.12 and Fig 5.13.
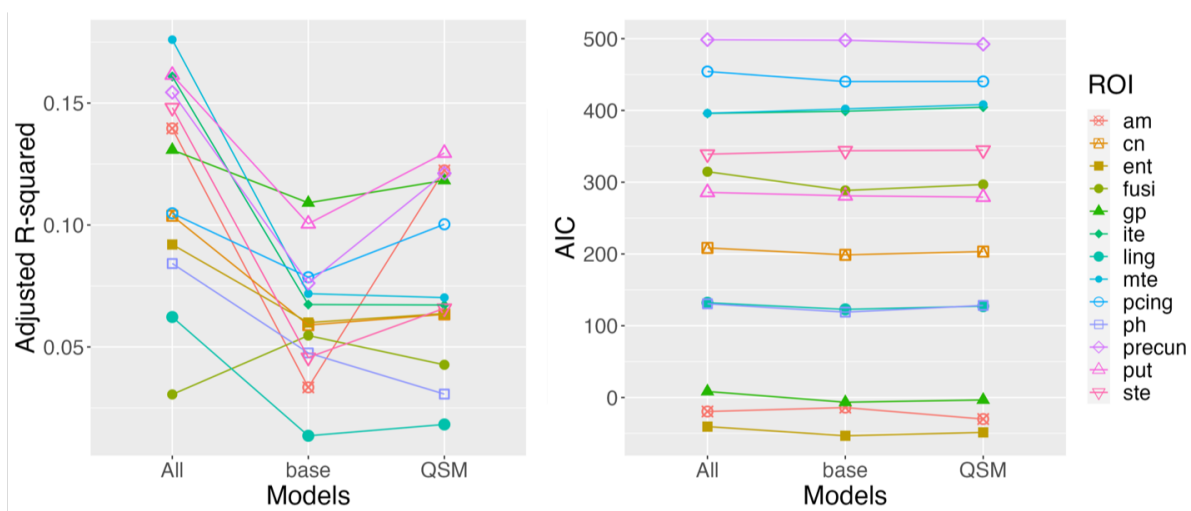
Figure 5.12: Comparison of multiple regression models for amyloid PET using different subsets of susceptibility features for all the participants.
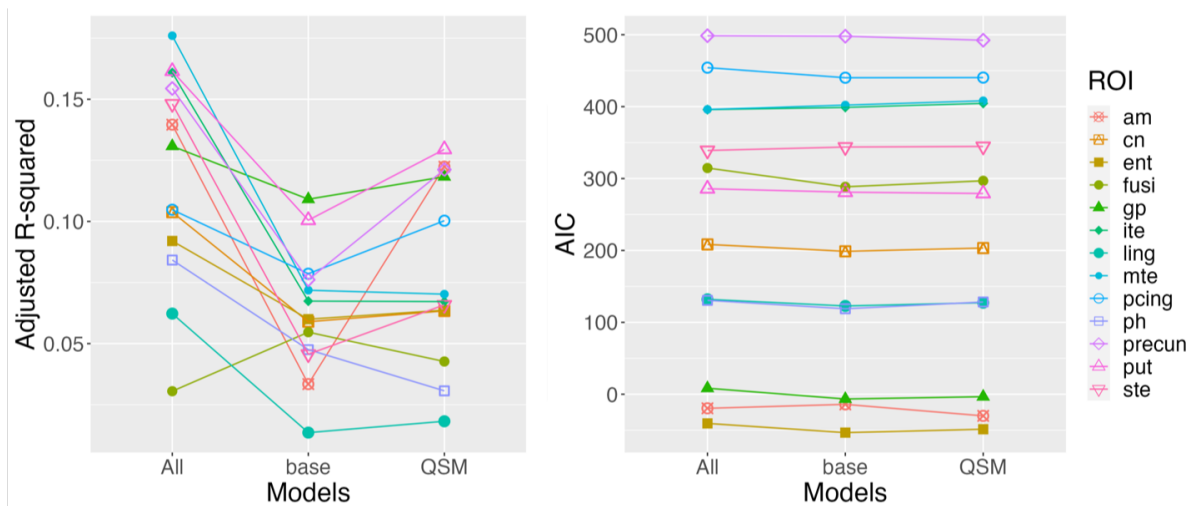
Figure 5.13: Comparison of multiple regression models for amyloid PET using different subsets of susceptibility features for 'amyloid-positive' participants.

5.6 Susceptibility metrics and STMS

STMS score was converted to z-score and models similar to amyloid and tau PET were analyzed.

5.6.1 Linear models for STMS

STMS is a clinical measure and susceptibility is an MRI-based imaging marker. So, modeling one with the other may not result in too high of an adjR value. This is confirmed for all the subjects as shown in Fig. 5.14 and in all of the subject groups as shown in Fig. 5.15, Fig. 5.16, and Fig. 5.17. The range of STMS varies much less for the healthy control group as shown in Table 5.1, with an Interquartile Range (IQR) of 3 (38-35). The highest adjRs were observed in the models containing all susceptibility metrics in Fig. 5.15. Since most of the participants are HC, the analysis containing all the subjects in Fig. 5.17 may be biased by the observation of HC participants.

Focusing on the more important MCI group in Fig. 5.16 reveals AICs were the lowest for the base models containing only age and ROI QSM for all the ROIs. The highest adjR was observed in putamen between all the ROIs. The importance of this subcortical region has been repeatedly mentioned in previous work and the current one in terms of iron accumulation and susceptibility alteration with age in between different subject groups already. Here that is reinforced by the relatively larger adjR of putamen model compared to other cortical ROIs. Also, the IQR of STMS values for the MCI group was also quite small (33-29 = 4) as shown in Table 5.1.
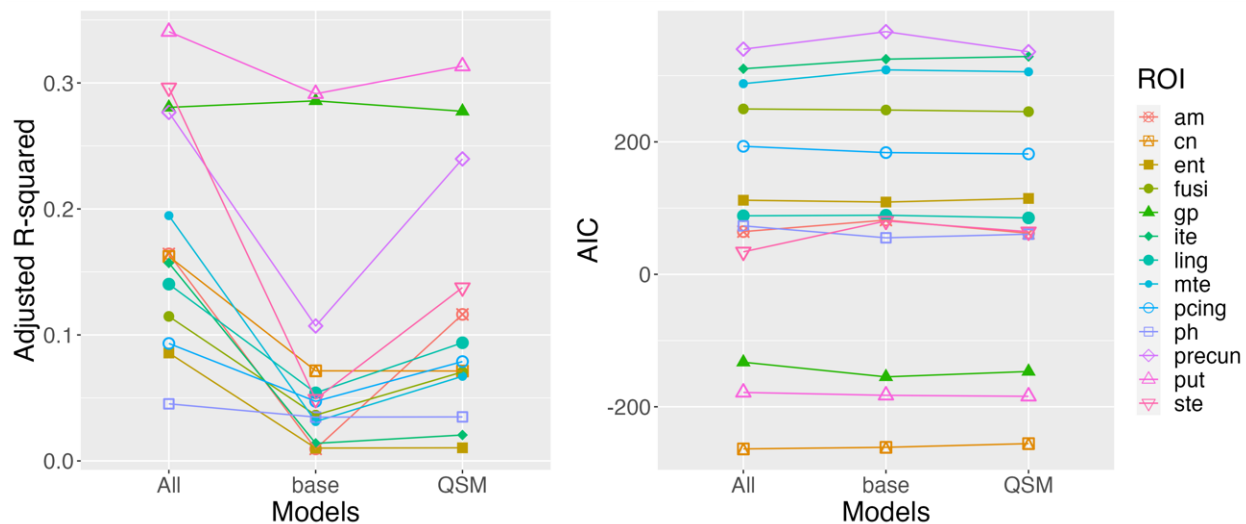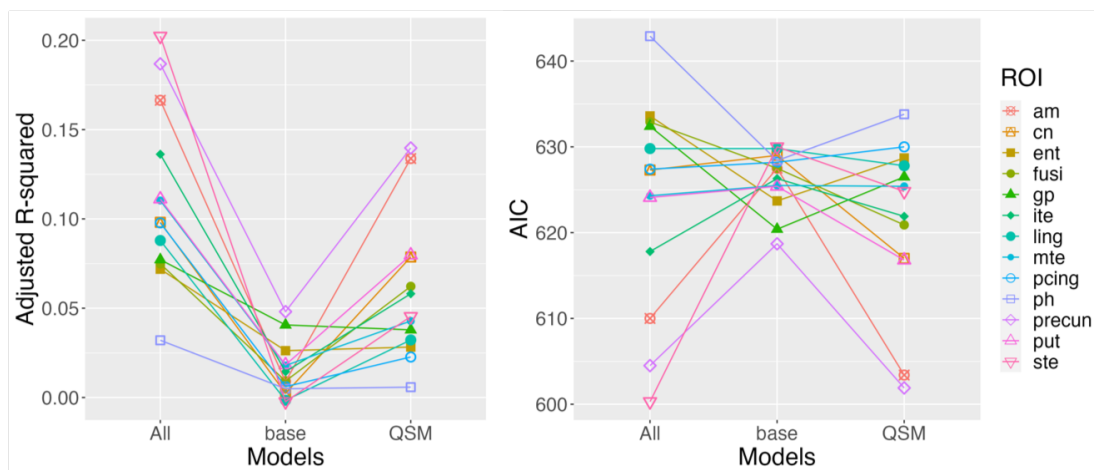
Figure 5.14: Comparison of multiple regression models for STMS z-score using different subsets of susceptibility features for all participants.
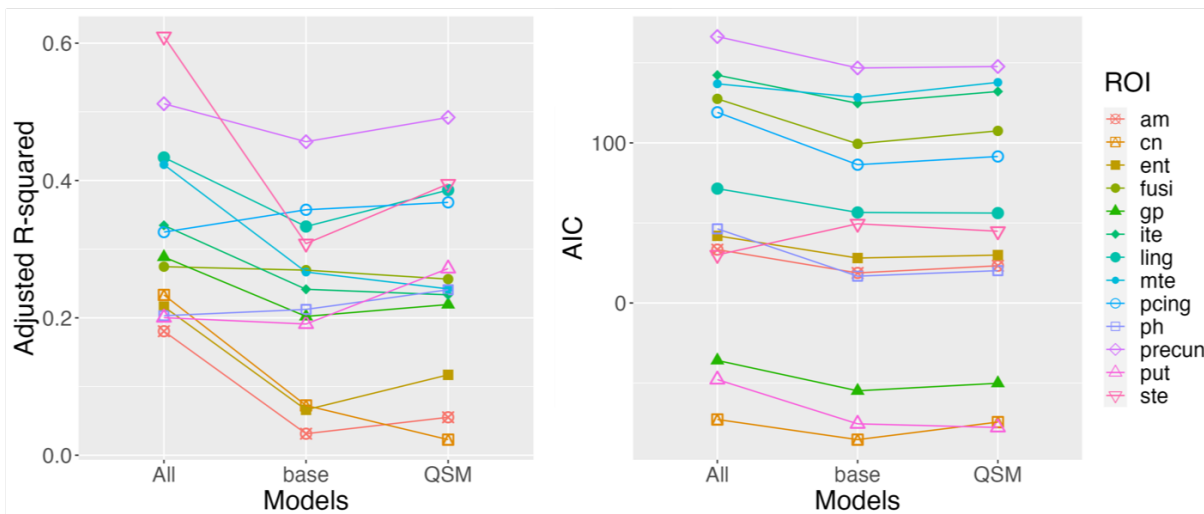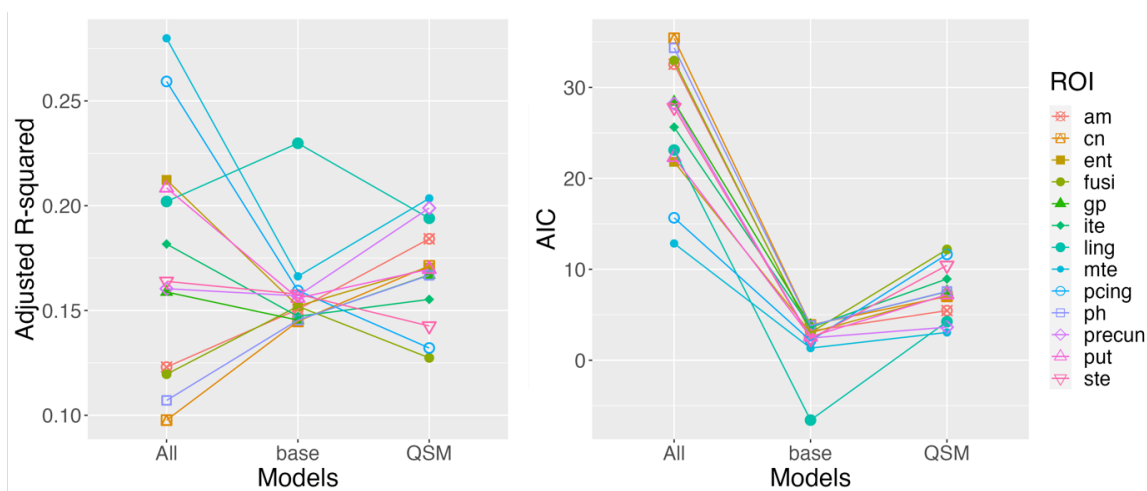

Figure 5.15: Comparison of multiple regression models for STMS z-score using different subsets of susceptibility features for the HC participants.

In AD patients' lingual cortex showed the highest adjR followed by gp and cn as shown in Fig. 5.17. It was interesting to see a cortical region showing higher adjR in the all-feature model compared to subcortical regions. In terms of AIC, all the ROIs showed superior performance in the base model containing only age and ROI QSM. IQR of STMS (28-18=10) was quite high in the AD patient group compared to HC and MCI groups as shown in Table 5.1.
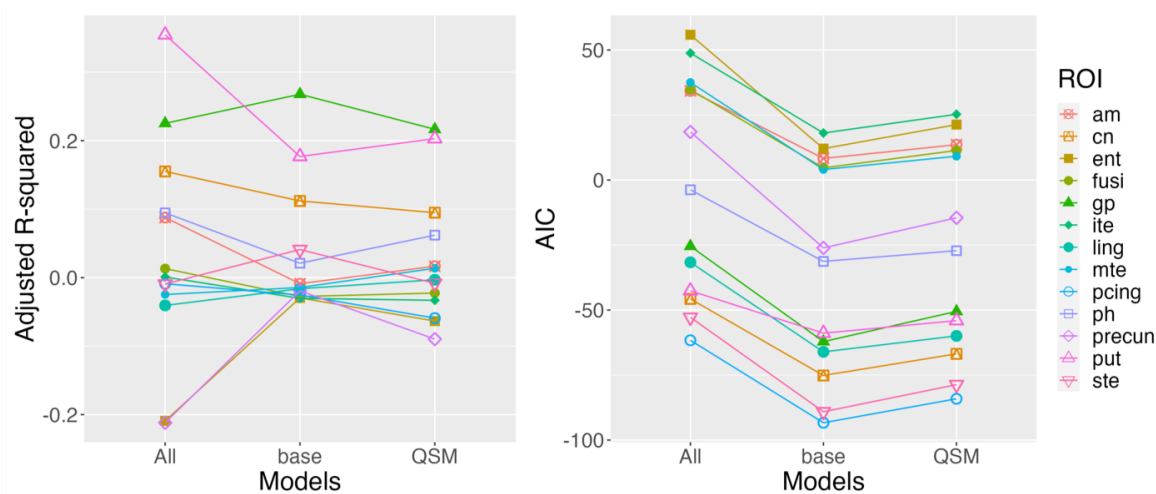
Figure 5.16: Comparison of multiple regression models for STMS z-score using different subsets of susceptibility features for the MCI patients.
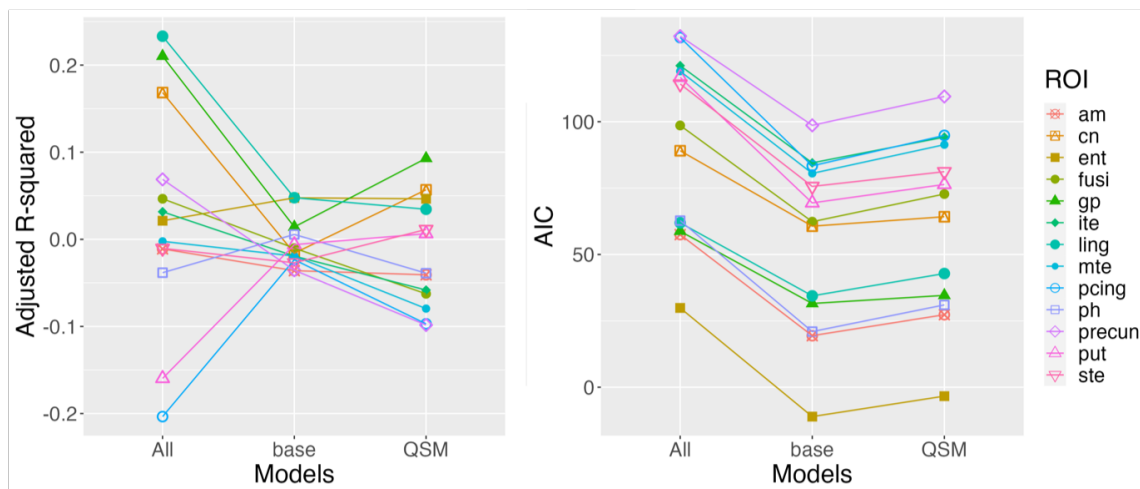
Figure 5.17: Comparison of multiple regression models for STMS z-score using different subsets of susceptibility features for AD patients.

5.7 Conclusion

Among different markers presented in this chapter tau PET SUVR showed a moderately strong association with susceptibility distribution parameters, particularly in superior temporal cortex. On the other hand, amyloid PET did not show too strong of an association with susceptibility metrics in the chosen ROIs. Tau PET uptake represents cognitive decline

better than amyloid PET and hence susceptibility metrics associating more with tau PET
is significant. Perhaps, because of a similar reason susceptibility metrics showed moderate
AUC in separating AD patients from other subjects in amygdala and precuneus. Last but not
least susceptibility metrics associated with STMS score in lingual cortex and other subcorti-
cal ROIs in AD patients is also a very important outcome of the current study. Through the
analysis presented in this chapter, it has been established that using only mean ROI QSM in
associating with other clinical, and pathological markers may underemphasize the usefulness
of MRI-based susceptibility mapping. It is hoped that the current study will inspire future
multi-center multi-scanner studies with optimized sequences to understand the full potential
QSM and compartmentalized susceptibility mapping.

Chapter 6

Conclusion and Future Work

The paramagnetic (PCS) and diamagnetic (DCS) compartments from DECOMPOSE-QSM are tested as a marker for the presence of pathology (iron, β-amyloid and tau). Observed increased PCS in cortical, subcortical, and WM regions confirm increased iron accumulation in the AD brain. Also, the strong association between tau PET and PCS reinforces the iron colocalization hypothesis with tau tangles in several ROIs. On the other hand, DCS is affected in an opposing manner by two important pathological changes, such as protein accumulation and demyelination. In the voxel-wise analysis of the WM, a lower |DCS| pointed to white matter integrity loss. Voxel-wise analysis results of the |DCS| value in the CSF region may be an indication of the decrease of the β-amyloid-42/ β-amyloid-40 ratio in AD. Introducing susceptibility distribution parameters to assess disease status and pathology progression resulted in somewhat inspiring observations with moderate effect sizes such as AUC and adjusted R squared.

The distinctive way of measuring compartmentalized magnetic susceptibility will allow the investigation of pathological changes happening in all tissue types such as GM, WM, and CSF of the brain. There are numerous studies on using QSM as a potential biomarker for neurodegenerative diseases. The purpose of this work was to investigate whether the two derived contrasts, namely PCS and DCS, from DECOMPOSE-QSM, can provide additional information. To gain a comprehensive view of how much DECOMPOSE could be beneficial to understand AD progression, many other contrasts and clinical diagnosis data need to be applied in parallel. Histological verification was out of scope in the current study, which would be needed in the future to verify the usefulness of DCS. This verification can ensure whether the gray matter susceptibility changes detected in the current work represent demyelination. Due to the nature of the retrospective analysis, the MEGRE data of the participants used in the current work only contain five echoes which is the minimum number of echoes for DECOMPOSE to perform in theory, and more echoes could benefit better susceptibility compartmentalization. The DECOMPOSE-QSM model does not address the composition of species within the diamagnetic or paramagnetic regime. We are unable to differentiate which protein or peptide specifically contributes to the DCS contrast. Longitudinal study rather than cross-sectional analysis may provide more meaningful insight into

the relationship between pathology progression and susceptibility measures as well.

Statistical tests have been used to assess the relationship between pathological markers and susceptibility. These tests are limited by the number of participants and the noise level of data. A conservative family-wise correction was applied for all p-value-based statistics to increase their reliability. In addition to the p-values, the magnitude of the correlation coefficient was taken as a convincing measure of association.

the initial promise observed with susceptibility separation future studies need to be designed with comparable age groups and size of the patient group. Also, optimization of the relevant pulse sequences to acquire MEGRE data in the most reproducible way would be beneficial. Multi-center and multi-scanner reproducibility are also important in order to establish the usefulness of the sequence. Test-retest reproducibility is needed to be assessed. More sequences and modalities need to be studied by combining DECOMPOSE-QSM to increase the performance of the model introduced in chapter 5. Utilization of separated susceptibility in the study of other neurodegenerative diseases such as PD, MS, Huntington's disease, and so on is worth exploring.

Separating susceptibility compartments to even further precision to compute contribution from different sources containing similar polarity of susceptibilities such as myelin, plaques, tangles or even calcification are interesting problems. More intricate signal models considering structural composition and variability of susceptibility sources can potentially be explored to attempt this.

Explicit comparison and association between susceptibility-based modalities and other modalities such as diffusion or MTI-based modalities need to be compared and potentially combined to extract more information in less amount of acquisition time. Utilization of these combined modalities to explore intricate pathways of disease progression would be exciting. Imaging in higher resolution and DECOMPOSING may even result in fine-grained information not revealed at the current resolution. In short, we have to look at studying neurodegeneration with MRI as an information extraction maximization problem where the highest amount of details can be obtained with the amount of time and effort ensuring the comfort of the patients.

Bibliography

[1]   Marion Delenclos, Daryl R. Jones, Pamela J. McLean, and Ryan J. Uitti. "Biomarkers in Parkinson's disease: Advances and strategies". In: *Parkinsonism I& Related Disorders* 22 (Jan. 2016), S106–S110. ISSN: 1353-8020. DOI: 10.1016/J.PARKRELDIS.2015.09.048.

[2]   Jeffrey Cummings. "The Role of Biomarkers in Alzheimer's Disease Drug Development". In: ed. by Paul C Guest. Springer International Publishing, 2019, pp. 29–61. ISBN: 978-3-030-05542-4. DOI: 10.1007/978-3-030-05542-4_2. URL: https://doi.org/10.1007/978-3-030-05542-4_2.

[3]   Oskar Hansson, Sylvain Lehmann, Markus Otto, Henrik Zetterberg, and Piotr Lewczuk. "Advantages and disadvantages of the use of the CSF Amyloid B (AB) 42/40 ratio in the diagnosis of Alzheimer's Disease". In: *Alzheimer's Research and Therapy* 11 (1 2019), pp. 1–15. ISSN: 17589193. DOI: 10.1186/s13195-019-0485-0.

[4]   Femke H. Bouwman, Giovanni B. Frisoni, Sterling C. Johnson, Xiaochun Chen, Sebastiaan Engelborghs, Takeshi Ikeuchi, Claire Paquet, Craig Ritchie, Sasha Bozeat, Frances-Catherine Quevenco, and Charlotte Teunissen. "Clinical application of CSF biomarkers for Alzheimer's disease: From rationale to ratios". In: *Alzheimer's & Dementia: Diagnosis, Assessment & Disease Monitoring* 14 (1 2022), pp. 1–12. ISSN: 2352-8729. DOI: 10.1002/dad2.12314.

[5]   Chia Chan Liu, Takahisa Kanekiyo, Huaxi Xu, and Guojun Bu. "Apolipoprotein e and Alzheimer disease: Risk, mechanisms and therapy". In: *Nature Reviews Neurology* 9 (2 Feb. 2013), pp. 106–118. ISSN: 17594758. DOI: 10.1038/nrneurol.2012.263.

[6]   Chenyou Sun, Xiaoming Ou, Jerry M Farley, Craig Stockmeier, Steven Bigler, Roberta Diaz Brinton, and Jun Ming Wang. "Imaging of Alzheimer's Disease". In: 9 (4 2012). Good paper, pp. 473–480. DOI: 10.1177/1051228403254657.

[7]   Theresa M. Harrison, Renaud La Joie, Anne Maass, Suzanne L. Baker, Kaitlin Swinnerton, Laura Fenton, Taylor J. Mellinger, Lauren Edwards, Julie Pham, Bruce L. Miller, Gil D. Rabinovici, and William J. Jagust. "Longitudinal tau accumulation and atrophy in aging and alzheimer disease". In: *Annals of Neurology* 85 (2 2019), pp. 229–240. ISSN: 15318249. DOI: 10.1002/ana.25406.

[8] Jiayin Kang, Yaozong Gao, Feng Shi, David S. Lalush, Weili Lin, and Dinggang Shen. "Prediction of standard-dose brain PET image by using MRI and low-dose brain [18F]FDG PET images". In: *Medical Physics* 42 (9 2015), pp. 5301–5309. ISSN: 00942405. DOI: 10.1118/1.4928400.

[9] Jiaying Zhang. "Applications of NODDI for imaging in vivo white matter pathology in neurodegenerative diseases". In: *Doctoral thesis, UCL (University College London).* (2019).

[10] J. O'Callaghan et al. "Tissue magnetic susceptibility mapping as a marker of tau pathology in Alzheimer's disease". In: *NeuroImage* 159 (July 2017), pp. 334–345. ISSN: 10959572. DOI: 10.1016/j.neuroimage.2017.08.003.

[11] Silvia Mangia, Federico De Martino, Timo Liimatainen, Michael Garwood, and Shalom Michaeli. "Magnetization transfer using inversion recovery during off-resonance irradiation". In: *Magnetic Resonance Imaging* 29 (10 Dec. 2011), pp. 1346–1350. ISSN: 0730-725X. DOI: 10.1016/J.MRI.2011.04.002.

[12] Hedi An, Xiaoyan Zeng, Tengfei Niu, Gaiying Li, Jie Yang, Lanlan Zheng, Wei Zhou, Hong Liu, Miaomiao Zhang, Dongya Huang, and Jianqi Li. "Quantifying iron deposition within the substantia nigra of Parkinson's disease by quantitative susceptibility mapping". In: *Journal of the Neurological Sciences* 386 (December 2017 2018), pp. 46–52. ISSN: 18785883. DOI: 10.1016/j.jns.2018.01.008. URL: https://doi.org/10.1016/j.jns.2018.01.008.

[13] Ulrike W. Kaunzner, Yeona Kang, Shun Zhang, Eric Morris, Yihao Yao, Sneha Pandya, Sandra M. Hurtado Rua, Calvin Park, Kelly M. Gillen, Thanh D. Nguyen, Yi Wang, David Pitt, and Susan A. Gauthier. "Quantitative susceptibility mapping identifies inflammation in a subset of chronic multiple sclerosis lesions". In: *Brain* 142 (1 2019), pp. 133–145. ISSN: 14602156. DOI: 10.1093/brain/awy296.

[14] Jingjia Chen, Nan-jie Gong, Khallil Taverna Chaim, Maria Concepci´on Garc´ıa Otaduy, and Chunlei Liu. "Decompose quantitative susceptibility mapping (QSM) to sub- voxel diamagnetic and paramagnetic components based on gradient-echo MRI data". In: *NeuroImage* (2021), p. 118477. ISSN: 1053-8119. DOI: 10.1016/j.neuroimage.2021.118477. URL: https://doi.org/10.1016/j.neuroimage.2021.118477.

[15] Alexey V. Dimov, Thanh D. Nguyen, Kelly M. Gillen, Melanie Marcille, Pascal Spincemaille, David Pitt, Susan A. Gauthier, and Yi Wang. "Susceptibility source separation from gradient echo data using magnitude decay modeling". In: *Journal of Neuroimaging* (March 2022), pp. 1–8. ISSN: 1051-2284. DOI: 10.1111/jon.13014.

[16] Hyeong Geol Shin, Jingu Lee, Young Hyun Yun, Seong Ho Yoo, Jinhee Jang, Se Hong Oh, Yoonho Nam, Sehoon Jung, Sunhye Kim, Masaki Fukunaga, Woojun Kim, Hyung Jin Choi, and Jongho Lee. "chi-separation: Magnetic susceptibility source separation toward iron and myelin mapping in the brain". In: *NeuroImage* 240 (July

2021), p. 118371. ISSN: 10959572. DOI: `10.1016/j.neuroimage.2021.118371`. URL: `https://doi.org/10.1016/j.neuroimage.2021.118371`.

[17] Jeff Duyn. "MR susceptibility imaging". In: *Journal of Magnetic Resonance* 229 (2013), pp. 198–207. ISSN: 10907807. DOI: `10.1016/j.jmr.2012.11.013`. URL: `http://dx.doi.org/10.1016/j.jmr.2012.11.013`.

[18] Hongjiang Wei, Russell Dibb, Yan Zhou, Yawen Sun, Jianrong Xu, Nian Wang, and Chunlei Liu. "Streaking artifact reduction for quantitative susceptibility mapping of sources with large dynamic range". In: *NMR in Biomedicine* 28 (10 2015), pp. 1294–1303. ISSN: 10991492. DOI: `10.1002/nbm.3383`.

[19] Yoonho Nam, Jongho Lee, Dosik Hwang, and Dong Hyun Kim. "Improved estimation of myelin water fraction using complex model fitting". In: *NeuroImage* 116 (2015), pp. 214–221. ISSN: 10959572. DOI: `10.1016/j.neuroimage.2015.03.081`. URL: `http://dx.doi.org/10.1016/j.neuroimage.2015.03.081`.

[20] Surabhi Sood, Javier Urriola, David Reutens, Kieran O'Brien, Steffen Bollmann, Markus Barth, and Viktor Vegh. "Echo time-dependent quantitative susceptibility mapping contains information on tissue properties". In: *Magnetic Resonance in Medicine* 77 (5 2017), pp. 1946–1958. ISSN: 15222594. DOI: `10.1002/mrm.26281`.

[21] Andreas Deistung, Ferdinand Schweser, and Jürgen R. Reichenbach. "Overview of quantitative susceptibility mapping". In: *NMR in Biomedicine* 30 (4 2017). Review later, when studying QSM. ISSN: 10991492. DOI: `10.1002/nbm.3569`.

[22] Chunlei Liu, Hongjiang Wei, Nan-Jie Gong, Matthew Cronin, Russel Dibb, and Kyle Decker. "Quantitative Susceptibility Mapping: Contrast Mechanisms and Clinical Applications". In: *Tomography* 1 (1 2015), pp. 3–17. ISSN: 2379-1381. DOI: `10.18383/j.tom.2015.00136`.

[23] Woojin Jung, Steffen Bollmann, and Jongho Lee. "Overview of quantitative susceptibility mapping using deep learning: Current status, challenges and opportunities". In: *NMR in Biomedicine* (February 2020), pp. 1–14. ISSN: 10991492. DOI: `10.1002/nbm.4292`.

[24] Wei Li, Alexandru V. Avram, Bing Wu, Xue Xiao, and Chunlei Liu. "Integrated Laplacian-based phase unwrapping and background phase removal for quantitative susceptibility mapping". In: *NMR in Biomedicine* 27 (2 2014), pp. 219–227. ISSN: 09523480. DOI: `10.1002/nbm.3056`.

[25] Wei Li, Bing Wu, and Chunlei Liu. "Quantitative susceptibility mapping of human brain reflects spatial variation in tissue composition". In: *NeuroImage* 55 (4 2011). QSM base paper from our group. Trying to understand this first., pp. 1645–1656. ISSN: 10538119. DOI: `10.1016/j.neuroimage.2010.11.088`.

[26] Pinar Senay Özbay, Andreas Deistung, Xiang Feng, Daniel Nanz, Jürgen Rainer Reichenbach, and Ferdinand Schweser. "A comprehensive numerical analysis of background phase correction with V-SHARP". In: *NMR in Biomedicine* 30 (4 Apr. 2017). ISSN: 10991492. DOI: `10.1002/nbm.3550`.

[27] Tian Liu, Pascal Spincemaille, Ludovic de Rochefort, Bryan Kressler, and Yi Wang. "Calculation of susceptibility through multiple orientation sampling (COSMOS): A method for conditioning the inverse problem from measured magnetic field map to susceptibility source image in MRI". In: *Magnetic Resonance in Medicine* 61 (1 Jan. 2009). https://doi.org/10.1002/mrm.21828, pp. 196–204. ISSN: 0740-3194. DOI: `https://doi.org/10.1002/mrm.21828`. URL: `https://doi.org/10.1002/mrm.21828`.

[28] Chunlei Liu. *STISuite*. URL: `https://people.eecs.berkeley.edu/~chunlei.liu/software.html`.

[29] Clifford R. Jack et al. "NIA-AA Research Framework: Toward a biological definition of Alzheimer's disease". In: *Alzheimer's and Dementia* 14 (4 Apr. 2018), pp. 535–562. ISSN: 15525279. DOI: `10.1016/j.jalz.2018.02.018`.

[30] M Brant-Zawadzki, G D Gillan, and W R Nitz. "MP RAGE: a three-dimensional, T1 weighted, gradient-echo sequence–initial experience in the brain". In: *Radiology* 182 (3 1992). DOI: `10.1148/radiology.182.3.1535892`.

[31] Bruce Fischl. "FreeSurfer". In: *NeuroImage* 62 (2 2012), pp. 774–781. ISSN: 10538119. DOI: `10.1016/j.neuroimage.2012.01.021`.

[32] B. Fischl. *Freesurfer*. URL: `https://surfer.nmr.mgh.harvard.edu/`.

[33] Petrice M. Cogswell et al. "Associations of quantitative susceptibility mapping with Alzheimer's disease clinical and imaging markers". In: *NeuroImage* 224 (October 2020 2021), p. 117433. ISSN: 10959572. DOI: `10.1016/j.neuroimage.2020.117433`. URL: `https://doi.org/10.1016/j.neuroimage.2020.117433`.

[34] *SPM*. URL: `https://www.fil.ion.ucl.ac.uk/spm/doc/`.

[35] Clifford R. Jack et al. "Defining imaging biomarker cut points for brain aging and Alzheimer's disease". In: *Alzheimer's and Dementia* 13 (3 2017), pp. 205–216. ISSN: 15525279. DOI: `10.1016/j.jalz.2016.08.005`.

[36] *MNI ICBM152 non-linear*. URL: `https://nist.mni.mcgill.ca/mni-icbm152-non-linear-6th-generation-symmetric-average-brain-stereotaxic-registration-model/`.

[37] B. Avants, N. Tustinson, and H. Johnson. *ANTs*. URL: `http://stnava.github.io/ANTs/`.

[38] Analysis Group, FMRIB, and Oxford. *fsl*. URL: `https://fsl.fmrib.ox.ac.uk/fsl/fslwiki`.

[39] *fsl randomise*. URL: https://fsl.fmrib.ox.ac.uk/fsl/fslwiki/Randomise/UserGuide.

[40] Marti J. Anderson and John Robinson. "Permutation tests for linear models". In: *Australian and New Zealand Journal of Statistics* 43 (1 2001), pp. 75–88. ISSN: 13691473. DOI: 10.1111/1467-842X.00156.

[41] *randomise theory*. URL: https://fsl.fmrib.ox.ac.uk/fsl/fslwiki/Randomise/Theory.

[42] Stephen M. Smith and Thomas E. Nichols. "Threshold-free cluster enhancement: Addressing problems of smoothing, threshold dependence and localisation in cluster inference". In: *NeuroImage* 44 (1 2009), pp. 83–98. ISSN: 10538119. DOI: 10.1016/j.neuroimage.2008.03.061. URL: http://dx.doi.org/10.1016/j.neuroimage.2008.03.061.

[43] Yongyue Zhang, Michael Brady, and Stephen Smith. "Segmentation of brain MR images through a hidden Markov random field model and the expectation-maximization algorithm". In: *IEEE Transactions on Medical Imaging* 20 (1 2001), pp. 45–57. ISSN: 02780062. DOI: 10.1109/42.906424.

[44] Daniele Mascali. *BrainSlicer*. 2022.

[45] Dominic Hare, Scott Ayton, Ashley Bush, and Peng Lei. "A delicate balance: Iron metabolism and diseases of the brain". In: *Frontiers in Aging Neuroscience* 5 (2013). ISSN: 1663-4365. URL: https://www.frontiersin.org/articles/10.3389/fnagi.2013.00034.

[46] Roberta J. Ward, Fabio A. Zucca, Jeff H. Duyn, Robert R. Crichton, and Luigi Zecca. "The role of iron in brain ageing and neurodegenerative disorders". In: *The Lancet Neurology* 13 (10 Oct. 2014), pp. 1045–1060. ISSN: 14744465. DOI: 10.1016/S1474-4422(14)70117-6.

[47] J. M.G. van Bergen, X. Li, F. C. Quevenco, A. F. Gietl, V. Treyer, R. Meyer, A. Buck, P. A. Kaufmann, R. M. Nitsch, P. C.M. van Zijl, C. Hock, and P. G. Unschuld. "Simultaneous quantitative susceptibility mapping and Flutemetamol-PET suggests local correlation of iron and B-amyloid as an indicator of cognitive performance at high age". In: *NeuroImage* 174 (March 2018), pp. 308–316. ISSN: 10959572. DOI: 10.1016/j.neuroimage.2018.03.021.

[48] Nicola Spotorno, Julio Acosta-Cabronero, Erik Stomrud, Björn Lampinen, Olof T. Strandberg, Danielle van Westen, and Oskar Hansson. "Relationship between cortical iron and tau aggregation in Alzheimer's disease". In: *Brain : a journal of neurology* 143 (5 2020). Reviewed ¡br/¿Needed to connect A-beta plaque and tau to PET and QSM for modeling, pp. 1341–1349. ISSN: 14602156. DOI: 10.1093/brain/awaa089.

[49] Lei Du et al. "Increased Iron Deposition on Brain Quantitative Susceptibility Mapping Correlates with Decreased Cognitive Function in Alzheimer's Disease". In: *ACS Chemical Neuroscience* 9 (7 July 2018), pp. 1849–1857. ISSN: 19487193. DOI: `10.1021/acschemneuro.8b00194`.

[50] Holly Spence, Chris J. McNeil, and Gordon D. Waiter. "The impact of brain iron accumulation on cognition: A systematic review". In: *PLoS ONE* 15 (10 October Oct. 2020). ISSN: 19326203. DOI: `10.1371/journal.pone.0240697`.

[51] Julio Acosta-Cabronero, Guy B. Williams, Arturo Cardenas-Blanco, Robert J. Arnold, Victoria Lupson, and Peter J. Nestor. "In vivo quantitative susceptibility mapping (QSM) in Alzheimer's disease". In: *PLoS ONE* 8 (11 2013). ISSN: 19326203. DOI: `10.1371/journal.pone.0081093`.

[52] Petr Dusek, Tim Hofer, Jan Alexander, Per M. Roos, and Jan O. Aaseth. "Cerebral Iron Deposition in Neurodegeneration". In: *Biomolecules* 12 (5 May 2022). ISSN: 2218273X. DOI: `10.3390/biom12050714`.

[53] Scott Ayton et al. "Cerebral quantitative susceptibility mapping predicts amyloid-B-related cognitive decline". In: *Brain* 140 (8 2017), pp. 2112–2119. ISSN: 14602156. DOI: `10.1093/brain/awx137`.

[54] Andrew Gleason and Ashley I Bush. "Iron and Ferroptosis as Therapeutic Targets in Alzheimer's Disease". In: (). DOI: `10.1007/s13311-020`. URL: `https://doi.org/10.1007/s13311-020-00954-y`.

[55] Erika P Raven, Po H Lu, Todd A Tishler, Panthea Heydari, and George Bartzokis. "Increased Iron Levels and Decreased Tissue Integrity in Hippocampus of Alzheimer's Disease Detected in vivo with Magnetic Resonance Imaging". In: *Journal of Alzheimer's Disease* 37 (2013), pp. 127–136. ISSN: 1875-8908. DOI: `10.3233/JAD-130209`.

[56] Feixue Wang, Jiandong Wang, Ying Shen, Hao Li, Wolf-Dieter Rausch, and Xiaobo Huang. "Iron Dyshomeostasis and Ferroptosis: A New Alzheimer's Disease Hypothesis?" In: *Frontiers in Aging Neuroscience* 14 (2022). ISSN: 1663-4365. URL: `https://www.frontiersin.org/articles/10.3389/fnagi.2022.830569`.

[57] Noah Lubben, Elizabeth Ensink, Gerhard A. Coetzee, and Viviane Labrie. "The enigma and implications of brain hemispheric asymmetry in neurodegenerative diseases". In: *Brain Communications* 3 (3 2021). ISSN: 26321297. DOI: `10.1093/braincomms/fcab211`.

[58] Boyd Kenkhuis, Antonios Somarakis, Lorraine de Haan, Oleh Dzyubachyk, Marieke E. IJsselsteijn, Noel F.C.C. de Miranda, Boudewijn P.F. Lelieveldt, Jouke Dijkstra, Willeke M.C. van Roon-Mom, Thomas Höllt, and Louise van der Weerd. "Iron loading is a prominent feature of activated microglia in Alzheimer's disease patients". In: *Acta Neuropathologica Communications* 9 (1 Dec. 2021). ISSN: 20515960. DOI: `10.1186/s40478-021-01126-5`.

[59] Steven J. Madsen, Phillip S. DiGiacomo, Yitian Zeng, Maged Goubran, Yuanxin Chen, Brian K. Rutt, Donald Born, Hannes Vogel, Robert Sinclair, and Michael M. Zeineh. "Correlative Microscopy to Localize and Characterize Iron Deposition in Alzheimer's Disease". In: *Journal of Alzheimer's Disease Reports* 4 (1 Dec. 2020), pp. 525–536. DOI: `10.3233/adr-200234`.

[60] Dean Tran, Phillip DiGiacomo, Donald E. Born, Marios Georgiadis, and Michael Zeineh. "Iron and Alzheimer's Disease: From Pathology to Imaging". In: *Frontiers in Human Neuroscience* 16 (July 2022). ISSN: 16625161. DOI: `10.3389/fnhum.2022.838692`.

[61] Michael M Zeineh, Yuanxin Chen, Hagen H Kitzler, Robert Hammond, Hannes Vogel, Brian K Rutt, and Dresden Dresden. "Activated iron-containing microglia in the human hippocampus identified by magnetic resonance imaging in Alzheimer disease HHS Public Access". In: *Neurobiol Aging* 36 (9 2015), pp. 2483–2500. DOI: `10.1016/j.neurobiolaging`. URL: `http://dx.doi.org/10.1016/j.neurobiolaging.`.

[62] Sara van Duijn, Marjolein Bulk, Sjoerd G van Duinen, Rob J A Nabuurs, Mark A van Buchem, Louise van der Weerd, and Remco Natté. "Cortical Iron Reflects Severity of Alzheimer's Disease". In: *Journal of Alzheimer's Disease* 60 (2017), pp. 1533–1545. ISSN: 1875-8908. DOI: `10.3233/JAD-161143`.

[63] Chun Ki Franklin Au, Jill Abrigo, Chunlei Liu, Wanting Liu, Jack Lee, Lisa Wing Chi Au, Queenie Chan, Sirong Chen, Eric Yim Lung Leung, Chi Lai Ho, Ho Ko, Vincent Chung Tong Mok, and Weitian Chen. "Quantitative Susceptibility Mapping of the Hippocampal Fimbria in Alzheimer's Disease". In: *Journal of Magnetic Resonance Imaging* 53 (6 2021), pp. 1823–1832. ISSN: 15222586. DOI: `10.1002/jmri.27464`.

[64] Jenna N. Adams, Anne Maass, Theresa M. Harrison, Suzanne L. Baker, and William J. Jagust. "Cortical tau deposition follows patterns of entorhinal functional connectivity in aging". In: *eLife* 8 (2019), pp. 1–22. ISSN: 2050084X. DOI: `10.7554/eLife.49132`.

[65] Michael J. Pontecorvo et al. "Comparison of regional flortaucipir PET with quantitative tau immunohistochemistry in three subjects with Alzheimer's disease pathology: a clinicopathological study". In: *EJNMMI Research* 10 (1 2020). ISSN: 2191219X. DOI: `10.1186/s13550-020-00653-x`.

[66] Hanna Cho, Jae Yong Choi, Mi Song Hwang, You Jin Kim, Hye Mi Lee, Hye Sun Lee, Jae Hoon Lee, Young Hoon Ryu, Myung Sik Lee, and Chul Hyoung Lyoo. "In vivo cortical spreading pattern of tau and amyloid in the Alzheimer disease spectrum". In: *Annals of Neurology* 80 (2 2016), pp. 247–258. ISSN: 15318249. DOI: `10.1002/ana.24711`.

[67] Philip S Insel, Elizabeth C Mormino, Paul S Aisen, Wesley K Thompson, and Michael C Donohue. "Neuroanatomical spread of amyloid B and tau in Alzheimer's disease: implications for primary prevention". In: *Brain Communications* 2 (1 2020), pp. 1–11. ISSN: 2632-1297. DOI: `10.1093/braincomms/fcaa007`.

[68] Clifford R. Jack et al. "Longitudinal tau PET in ageing and Alzheimer's disease". In: *Brain* 141 (5 2018), pp. 1517–1528. ISSN: 14602156. DOI: `10.1093/brain/awy059`.

[69] Justin S Sanchez et al. "The cortical origin and initial spread of medial temporal tauopathy in Alzheimer's disease assessed with positron emission tomography". In: 0655 (January 2021).

[70] Solveig Tiepolt, Michael Rullmann, Thies H. Jochimsen, Hermann Josef Gertz, Matthias L. Schroeter, Marianne Patt, Osama Sabri, and Henryk Barthel. "Quantitative susceptibility mapping in B-Amyloid PET-stratified patients with dementia and healthy controls – A hybrid PET/MRI study". In: *European Journal of Radiology* 131 (July 2020), p. 109243. ISSN: 18727727. DOI: `10.1016/j.ejrad.2020.109243`. URL: `https://doi.org/10.1016/j.ejrad.2020.109243`.

[71] RStudio Team (2020). *RStudio: Integrated Development for R. RStudio, PBC, Boston, MA.* URL: `http://www.rstudio.com/`.

[72] Chun Chen, Marnix Witte, Wilma Heemsbergen, and Marcel V. Herk. "Multiple comparisons permutation test for image based data mining in radiotherapy". In: *Radiation Oncology* 8 (1 2013), pp. 1–10. ISSN: 1748717X. DOI: `10.1186/1748-717X-8-293`.

[73] J. Mumford. *Day 32: Permutation tests that control for multiple comparisons.* URL: `https://www.youtube.com/watch?v=zg0tmnGGwBI&t=801s`.

[74] P. Lei, S. Ayton, and A. I. Bush. "The Essential Elements of Alzheimer's Disease Peng". In: *JBC papers* (2020). Later. Not relevant right now., pp. 1–61. DOI: `10.1074/jbc.REV120.008207`.

[75] Sangram S. Sisodia and Donald L. Price. "Role of the B-amyloid protein in Alzheimer's disease". In: *The FASEB Journal* 9 (5 1995), pp. 366–370. ISSN: 0892-6638. DOI: `10.1096/fasebj.9.5.7896005`.

[76] Michael J. Pontecorvo, Michael D. Devous, Michael Navitsky, Ming Lu, Stephen Salloway, Frederick W. Schaerf, Danna Jennings, Anupa K. Arora, Anne McGeehan, Nathaniel C. Lim, Hui Xiong, Abhinay D. Joshi, Andrew Siderowf, and Mark A. Mintun. "Relationships between flortaucipir PET tau binding and amyloid burden, clinical diagnosis, age and cognition". In: *Brain* 140 (3 2017), pp. 748–763. ISSN: 14602156. DOI: `10.1093/brain/aww334`.

[77] Julio Acosta-Cabronero, Judith Machts, Stefanie Schreiber, Susanne Abdulla, Katja Kollewe, Susanne Petri, Nicola Spotorno, Joern Kaufmann, Hans Jochen Heinze, Reinhard Dengler, Stefan Vielhaber, and Peter J. Nestor. "Quantitative susceptibility MRI to detect brain iron in amyotrophic lateral sclerosis". In: *Radiology* 289 (1 2018). Reviewed Jan 11, 2021, pp. 195–203. ISSN: 15271315. DOI: `10.1148/radiol.2018180112`.

[78] Klaus H. Maier-Hein, Carl Fredrik Westin, Martha E. Shenton, Michael W. Weiner, Ashish Raj, Philipp Thomann, Ron Kikinis, Bram Stieltjes, and Ofer Pasternak. "Widespread white matter degeneration preceding the onset of dementia". In: *Alzheimer's and Dementia* 11 (5 2015), 485–493.e2. ISSN: 15525279. DOI: `10.1016/j.jalz.2014.04.518`. URL: `http://dx.doi.org/10.1016/j.jalz.2014.04.518`.

[79] Sara E. Nasrabady, Batool Rizvi, James E. Goldman, and Adam M. Brickman. "White matter changes in Alzheimer's disease: a focus on myelin and oligodendrocytes". In: *Acta neuropathologica communications* 6 (1 2018), p. 22. ISSN: 20515960. DOI: `10.1186/s40478-018-0515-3`.

[80] Cynthia Wisnieff, Sriram Ramanan, John Olesik, Susan Gauthier, Yi Wang, and David Pitt. "Quantitative susceptibility mapping (QSM) of white matter multiple sclerosis lesions: Interpreting positive susceptibility and the presence of iron". In: *Magnetic Resonance in Medicine* 74 (2 2015), pp. 564–570. ISSN: 15222594. DOI: `10.1002/mrm.25420`.

[81] Marco Pasi, Inge W.M. Van Uden, Anil M. Tuladhar, Frank Erik De Leeuw, and Leonardo Pantoni. "White Matter Microstructural Damage on Diffusion Tensor Imaging in Cerebral Small Vessel Disease: Clinical Consequences". In: *Stroke* 47 (6 2016), pp. 1679–1684. ISSN: 15244628. DOI: `10.1161/STROKEAHA.115.012065`.

[82] Nan Jie Gong, Russell Dibb, Marjolein Bulk, Louise van der Weerd, and Chunlei Liu. "Imaging beta amyloid aggregation and iron accumulation in Alzheimer's disease using quantitative susceptibility mapping MRI". In: *NeuroImage* 191 (100 2019). Reviewed Jan 11, 2021¡br/¿¡br/¿Useful paper from our group to relate QSM with beta-amyloid plaque concentration and tau NFT concentration, pp. 176–185. ISSN: 10959572. DOI: `10.1016/j.neuroimage.2019.02.019`. URL: `https://doi.org/10.1016/j.neuroimage.2019.02.019`.

[83] Zhiyong Zhao, Lei Zhang, Qingqing Wen, Wanrong Luo, Weihao Zheng, Tingting Liu, Yi Zhang, Keqing Zhu, and Dan Wu. "The effect of beta-amyloid and tau protein aggregations on magnetic susceptibility of anterior hippocampal laminae in Alzheimer's diseases". In: *NeuroImage* 244 (Dec. 2021), p. 118584. ISSN: 1053-8119. DOI: `10.1016/J.NEUROIMAGE.2021.118584`.

[84] Zhaoyuan Gong, Murat Bilgel, Matthew Kiely, Curtis Triebswetter, Luigi Ferrucci, Susan M. Resnick, Richard G. Spencer, and Mustapha Bouhrara. "Lower myelin content is associated with more rapid cognitive decline among cognitively unimpaired

individuals". In: *Alzheimer's and Dementia* (2023). ISSN: 15525279. DOI: `10.1002/alz.12968`.

[85] Chunlei Liu, Wei Li, G. Allan Johnson, and Bing Wu. "High-field (9.4 T) MRI of brain dysmyelination by quantitative mapping of magnetic susceptibility". In: *NeuroImage* 56 (3 June 2011), pp. 930–938. ISSN: 1053-8119. DOI: `10.1016/J.NEUROIMAGE.2011.02.024`.

[86] Jongho Lee, Karin Shmueli, Byeong Teck Kang, Bing Yao, Masaki Fukunaga, Peter Van Gelderen, Sara Palumbo, Francesca Bosetti, Afonso C. Silva, and Jeff H. Duyn. "The contribution of myelin to magnetic susceptibility-weighted contrasts in high-field MRI of the brain". In: *NeuroImage* 59 (4 Feb. 2012), pp. 3967–3975. ISSN: 1053-8119. DOI: `10.1016/J.NEUROIMAGE.2011.10.076`.

[87] Nian Wang, Jie Zhuang, Hongjiang Wei, Russell Dibb, Yi Qi, and Chunlei Liu. "Probing demyelination and remyelination of the cuprizone mouse model using multimodality MRI". In: *Journal of Magnetic Resonance Imaging* 50 (6 2019), pp. 1852–1865. ISSN: 15222586. DOI: `10.1002/jmri.26758`.

[88] Adam M. Brickman. "Contemplating Alzheimer's disease and the contribution of white matter hyperintensities". In: *Current Neurology and Neuroscience Reports* 13 (12 2013). ISSN: 15284042. DOI: `10.1007/s11910-013-0415-7`.

[89] Adam M. Brickman, Nicole Schupf, Jennifer J. Manly, Yaakov Stern, José A. Luchsinger, Frank A. Provenzano, Atul Narkhede, Qolamreza Razlighi, Lyndsey Collins-Praino, Sylvaine Artero, Tasnime N. Akbaraly, Karen Ritchie, Richard Mayeux, and Florence Portet. "APOE e4 and risk for Alzheimer's disease: Do regionally distributed white matter hyperintensities play a role?" In: *Alzheimer's and Dementia* 10 (6 2014), pp. 619–629. ISSN: 15525279. DOI: `10.1016/j.jalz.2014.07.155`.

[90] A. A. Capizzano, L. Ación, T. Bekinschtein, M. Furman, H. Gomila, A. Martínes, R. Mizrahi, and S. E. Starkstein. "White matter hyperintensities are significantly associated with cortical atrophy in Alzheimer's disease". In: *Journal of Neurology, Neurosurgery and Psychiatry* 75 (6 2004), pp. 822–827. ISSN: 00223050. DOI: `10.1136/jnnp.2003.019273`.

[91] N. Hirono, H. Kitagaki, H. Kazui, M. Hashimoto, and E. Mori. "Impact of white matter changes on clinical manifestation of Alzheimer's disease: A quantitative study". In: *Stroke* 31 (9 2000), pp. 2182–2188. ISSN: 00392499. DOI: `10.1161/01.STR.31.9.2182`.

[92] Mustapha Bouhrara, David A. Reiter, Christopher M. Bergeron, Linda M. Zukley, Luigi Ferrucci, Susan M. Resnick, and Richard G. Spencer. "Evidence of demyelination in mild cognitive impairment and dementia using a direct and specific magnetic resonance imaging measure of myelin content". In: *Alzheimer's and Dementia* 14 (8 2018), pp. 998–1004. ISSN: 15525279. DOI: `10.1016/j.jalz.2018.03.007`.

[93] Ian A. McKenzie, David Ohayon, Huiliang Li, Joana Paes De Faria, Ben Emery, Koujiro Tohyama, and William D. Richardson. "Motor skill learning requires active central myelination". In: *Science* 346 (6207 2014), pp. 318–322. ISSN: 10959203. DOI: 10.1126/science.1254960.

[94] Holly E. Holmes et al. "Imaging the accumulation and suppression of tau pathology using multiparametric MRI". In: *Neurobiology of Aging* 39 (Mar. 2016), pp. 184–194. ISSN: 0197-4580. DOI: 10.1016/J.NEUROBIOLAGING.2015.12.001.

[95] Kaj Blennow and Harald Hampel. "CSF markers for incipient Alzheimer's disease". In: *The Lancet Neurology* 2 (10 Oct. 2003), pp. 605–613. ISSN: 1474-4422. DOI: 10.1016/S1474-4422(03)00530-1.

[96] Kaj Blennow, Harald Hampel, Michael Weiner, and Henrik Zetterberg. "Cerebrospinal fluid and plasma biomarkers in Alzheimer disease". In: *Nature Reviews Neurology* 6 (3 2010), pp. 131–144. ISSN: 17594758. DOI: 10.1038/nrneurol.2010.4.

[97] Richard J. Perrin, Anne M. Fagan, and David M. Holtzman. "Multimodal techniques for diagnosis and prognosis of Alzheimer's disease". In: *Nature* 461 (7266 2009), pp. 916–922. ISSN: 00280836. DOI: 10.1038/nature08538.

[98] Alex E. Roher, Jonathan D. Lowenson, Steven Clarke, Amina S. Woods, Robert J. Cotter, Eric Gowing, and Melvyn J. Ball. "B-amyloid-(1-42) is a major component of cerebrovascular amyloid deposits: Implications for the pathology of Alzheimer disease". In: *Proceedings of the National Academy of Sciences of the United States of America* 90 (22 1993), pp. 10836–10840. ISSN: 00278424. DOI: 10.1073/pnas.90.22.10836.

[99] Leon J. Thal, Kejal Kantarci, Eric M. Reiman, William E. Klunk, Michael W. Weiner, Henrik Zetterberg, Douglas Galasko, Domenico Praticò, Sue Griffin, Dale Schenk, and Eric Siemers. "The role of biomarkers in clinical trials for Alzheimer disease". In: *Alzheimer Disease and Associated Disorders* 20 (1 2006), pp. 6–15. ISSN: 08930341. DOI: 10.1097/01.wad.0000191420.61260.a8.

[100] Jong Duck Choi, Yeonsil Moon, Hee Jin Kim, Younghee Yim, Subin Lee, and Won Jin Moon. "Choroid Plexus Volume and Permeability at Brain MRI within the Alzheimer Disease Clinical Spectrum". In: *Radiology* 304 (3 Sept. 2022), pp. 635–645. ISSN: 15271315. DOI: 10.1148/radiol.212400.

[101] Diana G Nelles and Lili-Naz Hazrati. "Ependymal cells and neurodegenerative disease: outcomes of compromised ependymal barrier function". In: *Brain Communications* 4 (6 2022), pp. 1–12. ISSN: 26321297. DOI: 10.1093/braincomms/fcac288. URL: https://doi.org/10.1093/braincomms/fcac288.

[102] Saif Shahriar Rahman Nirzhor, Rubayat Islam Khan, and Sharmind Neelotpol. "The biology of glial cells and their complex roles in Alzheimer's disease: New opportunities in therapy". In: *Biomolecules* 8 (3 2018), pp. 1–21. ISSN: 2218273X. DOI: 10.3390/biom8030093.

[103] Andrei Irimia, Sean Mahoney, and Nahian F. Chowdhury. "Quantifying the longitudinal effects of Alzheimer's disease upon myelin content in gray matter". In: *Alzheimer's & dementia : the journal of the Alzheimer's Association* 17 (Dec. 2021), e054836. ISSN: 15525279. DOI: 10.1002/alz.054836.

[104] Wiesje Pelkmans, Ellen Dicks, Frederik Barkhof, Hugo Vrenken, Philip Scheltens, Wiesje M. van der Flier, and Betty M. Tijms. "Gray matter T1-w/T2-w ratios are higher in Alzheimer's disease". In: *Human Brain Mapping* 40 (13 2019), pp. 3900–3909. ISSN: 10970193. DOI: 10.1002/hbm.24638.

[105] Gary W. Van Hoesen, Jean C. Augustinack, Jason Dierking, Sarah J. Redman, and Ramasamy Thangavel. "The parahippocampal gyrus in Alzheimer's disease. Clinical and preclinical neuroanatomical correlates". In: vol. 911. New York Academy of Sciences, 2000, pp. 254–274. DOI: 10.1111/j.1749-6632.2000.tb06731.x.

[106] Ramasamy Thangavel, Gary W Van Hoesen, and Asgar Zaheer. *Posterior parahippocampal gyrus pathology in Alzheimer's disease.* 2008, pp. 667–676.

[107] Matthew F. Glasser and David C. van Essen. "Mapping human cortical areas in vivo based on myelin content as revealed by T1- and T2-weighted MRI". In: *Journal of Neuroscience* 31 (32 Aug. 2011), pp. 11597–11616. ISSN: 02706474. DOI: 10.1523/JNEUROSCI.2180-11.2011.

[108] Dingailu Ma, Irfete S Fetahu, Mei Wang, Rui Fang, Jiahui Li, Hang Liu, Tobin Gramyk, Isabella Iwanicki, Sophie Gu, Winnie Xu, Li Tan, Feizhen Wu, and Yujiang G Shi. "The fusiform gyrus exhibits an epigenetic signature for Alzheimer's disease". In: *Clinical Epigenetics* 12 (1 2020), p. 129. ISSN: 1868-7083. DOI: 10.1186/s13148-020-00916-3. URL: https://doi.org/10.1186/s13148-020-00916-3.

[109] Jonathan E Sherin and George Bartzokis. "Chapter 15 - Human Brain Myelination Trajectories Across the Life Span: Implications for CNS Function and Dysfunction". In: ed. by Edward J Masoro and Steven N Austad. Academic Press, 2011, pp. 333–346. ISBN: 978-0-12-378638-8. DOI: https://doi.org/10.1016/B978-0-12-378638-8.00015-4. URL: https://www.sciencedirect.com/science/article/pii/B9780123786388000154.

[110] Yu Veronica Sui, Arjun V. Masurkar, Henry Rusinek, Barry Reisberg, and Mariana Lazar. "Cortical myelin profile variations in healthy aging brain: A T1w/T2w ratio study". In: *NeuroImage* 264 (Dec. 2022). ISSN: 10959572. DOI: 10.1016/j.neuroimage.2022.119743.

[111] Pei Lin Lee, Kun Hsien Chou, Chih Ping Chung, Tzu Hsien Lai, Juan Helen Zhou, Pei Ning Wang, and Ching Po Lin. "Posterior Cingulate Cortex Network Predicts Alzheimer's Disease Progression". In: *Frontiers in Aging Neuroscience* 12 (Dec. 2020). ISSN: 16634365. DOI: 10.3389/fnagi.2020.608667.

[112] Hyug Gi Kim, Soonchan Park, Hak Young Rhee, Kyung Mi Lee, Chang Woo Ryu, Sun Jung Rhee, Soo Yeol Lee, Yi Wang, and Geon Ho Jahng. "Quantitative susceptibility mapping to evaluate the early stage of Alzheimer's disease". In: *NeuroImage: Clinical* 16 (March 2017), pp. 429–438. ISSN: 22131582. DOI: 10.1016/j.nicl.2017.08.019. URL: http://dx.doi.org/10.1016/j.nicl.2017.08.019.

[113] Marta Lancione, Matteo Cencini, Mauro Costagli, Graziella Donatelli, Michela Tosetti, Giulia Giannini, Roberta Zangaglia, Giovanna Calandra-Buonaura, Claudio Pacchetti, Pietro Cortelli, and Mirco Cosottini. "Diagnostic accuracy of quantitative susceptibility mapping in multiple system atrophy: The impact of echo time and the potential of histogram analysis". In: *NeuroImage: Clinical* 34 (December 2021 2022), p. 102989. ISSN: 2213-1582. DOI: 10.1016/J.NICL.2022.102989. URL: https://linkinghub.elsevier.com/retrieve/pii/S2213158222000547.

[114] *LDA in geeksforgeeks*. URL: https://www.geeksforgeeks.org/ml-linear-discriminant-analysis/.

[115] Guido Van Rossum and Fred L. Drake. *Python 3 Reference Manual*. Scotts Valley, CA: CreateSpace, 2009. ISBN: 1441412697.

[116] Sebastian Palmqvist, Michael Schöll, Olof Strandberg, Niklas Mattsson, Erik Stomrud, Henrik Zetterberg, Kaj Blennow, Susan Landau, William Jagust, and Oskar Hansson. "Earliest accumulation of B-amyloid occurs within the default-mode network and concurrently affects brain connectivity". In: *Nature Communications* 8 (1 2017). ISSN: 20411723. DOI: 10.1038/s41467-017-01150-x.

[117] Parsa Ravanfar, Samantha M. Loi, Warda T. Syeda, Tamsyn E. Van Rheenen, Ashley I. Bush, Patricia Desmond, Vanessa L. Cropley, Darius J.R. Lane, Carlos M. Opazo, Bradford A. Moffat, Dennis Velakoulis, and Christos Pantelis. "Systematic Review: Quantitative Susceptibility Mapping (QSM) of Brain Iron Profile in Neurodegenerative Diseases". In: *Frontiers in Neuroscience* 15 (Feb. 2021). ISSN: 1662453X. DOI: 10.3389/fnins.2021.618435.

[118] Shira Knafo. "Amygdala in Alzheimer's Disease". In: ed. by Barbara Ferry. IntechOpen, 2012, Ch. 15. DOI: 10.5772/52804. URL: https://doi.org/10.5772/52804.

[119] Mohammed Amir Husain, Benoit Laurent, and Mélanie Plourde. "APOE and Alzheimer's Disease: From Lipid Transport to Physiopathology and Therapeutics". In: *Frontiers in Neuroscience* 15 (2021). ISSN: 1662-453X. URL: https://www.frontiersin.org/articles/10.3389/fnins.2021.630502.

[120] *Naive Bayes Classifier: Pros & Cons, Applications & Types Explained*. URL: upgrad.com/blog/naive-bayes-classifier/.

[121] Talia M Nir, Alyssa H Zhu, Iyad Ba Gari, Daniel Dixon, Tasfiya Islam, Julio E Villalon-Reina, Sarah E Medland, Paul M Thompson, and Neda Jahanshad. *Effects of ApoE4 and ApoE2 genotypes on subcortical magnetic susceptibility and microstructure in 27,535 participants from the UK Biobank † ‡*. 2021. URL: `www.worldscientific.com`.

[122] Grégory Operto et al. "White matter microstructure is altered in cognitively normal middle-aged APOE-e4 homozygotes". In: *Alzheimer's Research & Therapy* 10 (1 2018), p. 48. ISSN: 1758-9193. DOI: `10.1186/s13195-018-0375-x`. URL: `https://doi.org/10.1186/s13195-018-0375-x`.

[123] KSV Muralidhar. *Demystifying R-Squared and Adjusted R-Squared*. URL: `https://builtin.com/data-science/adjusted-r-squared`.

[124] Yash Choksi. *Model selection: Cp, AIC, BIC and adjusted R^2*. URL: `https://medium.com/analytics-vidhya/model-selection-cp-aic-bic-and-adjusted-r2-6a0af25945b6`.

[125] Val J. Lowe et al. "Tau-positron emission tomography correlates with neuropathology findings". In: *Alzheimer's and Dementia* 16 (3 Mar. 2020), pp. 561–571. ISSN: 15525279. DOI: `10.1016/j.jalz.2019.09.079`.

[126] Klevest Gjini, Cameron Casey, Sean Tanabe, Amber Bo, Margaret Parker, Marissa White, David Kunkel, Richard Lennertz, Robert A Pearce, Tobey Betthauser, Bradley T Christian, Sterling C Johnson, Barbara B Bendlin, and Robert D Sanders. "Greater tau pathology is associated with altered predictive coding". In: *Brain Communications* 4 (5 Oct. 2022), fcac209. ISSN: 2632-1297. DOI: `10.1093/braincomms/fcac209`. URL: `https://doi.org/10.1093/braincomms/fcac209`.

[127] Thomas Lumley and Alan Miller. *leaps: Regression Subset Selection*. Jan. 2020.

[128] Daniel Lüdecke, Mattan Ben-Shachar, Indrajeet Patil, Philip Waggoner, and Dominique Makowski. "performance: An R Package for Assessment, Comparison and Testing of Statistical Models". In: *Journal of Open Source Software* 6 (60 Apr. 2021), p. 3139. DOI: `10.21105/joss.03139`.